

Master's Thesis

MSc Physics and Nanotechnology

Site controlled epitaxy of quantum dots for nano- and quantum photonic applications in telecom wavelength range

Bjørn Funch Schrøder Nielsen

Supervisors:

Senior Researcher Elizaveta Semenova
Dr. Karolina Ewa Polczynska
PhD. student Christian Ruiz

March 1st 2025

Technical University of Denmark
Department of Electrical and Photonics Engineering
Ørsteds Plads
Building 343
2800 Kongens Lyngby, Denmark

I Summary

This work investigates the fabrication of strain-induced, site-controlled quantum dot structures using pre-patterning via high-resolution electron beam lithography, followed by the controlled self-assembly of quantum dots within the Stranski-Krastanov growth regime using Metalorganic Vapour-Phase Epitaxy (MOVPE). The objective was to achieve deterministic quantum dot placement with optimised uniformity and reproducibility, crucial for scalable quantum- and optoelectronic applications.

The first part of this thesis establishes the theoretical framework necessary to understand quantum dot behavior and formation. It begins with an introduction to quantum confinement principles and the effects of strain in epitaxial systems. We present the fundemental quantum effects that make quantum dots viable for photonics, mechanisms guiding self-assembly, particularly within the Stranski-Krastanov growth mode, and provide insight into how strain relaxation drives quantum dot nucleation. The thesis then explores deterministic site-controlled growth approaches, highlighting the challenges of transitioning from stochastic self-assembly to precise spatial control.

The second part of this work focuses on the experimental realisation of site-controlled quantum dots through nanofabrication and epitaxial growth. The process flow is detailed, including resist-coating, electron beam lithography exposure, etching and epitaxial growth using MOVPE. A series of growth experiments were conducted to refine the fabrication strategy, with specific attention given to precursor dynamics during the MOVPE growth. Finally, the fabricated structures were characterised using optical microscopy, scanning electron microscopy, and atomic force microscopy to evaluate quantum dot morphology and spatial distribution for various pattern geometries.

The findings of this work contribute to the development of scalable site-controlled quantum dots, essential for applications in quantum photonics.
While site-control was achieved to some extent, further optimisation of planarisation and etching processes is required to enhance reproducibility. The insights gained from this research provide a foundation for refining growth techniques and improving fabrication methodologies for future quantum dot technologies.

II Preface

The present thesis has been written in fulfillment of the graduation requirements for the Master's programme in Physics and Nanotechnology Engineering at the Technical University of Denmark (DTU). This research represents the outcome of two years of study and specialization in Nanosystems Engineering, combining theoretical physics with micro- and nanoscale fabrication.

During my master's studies, I had the opportunity to explore various aspects of physics and nanotechnology, including quantum information technology, fundamental quantum mechanics, solid-state physics, and materials science. While my focus was primarily on fabrication techniques and materials engineering, these topics provided a strong theoretical foundation for understanding and developing nanoscale systems.
Prior to my master's studies, I obtained a Bachelor's degree in Materials Engineering from DTU, where I built a strong background in materials science, semiconductor physics, and microfabrication techniques.
This experience laid the groundwork for my transition into nanotechnology and quantum device fabrication.

This thesis is written for readers with a background in physics and nanofabrication. While key topics are discussed in detail, references to relevant literature are provided for a more comprehensive understanding of specific concepts. I hope this work contributes to the ongoing advancements in nanoscale engineering and serves as a valuable resource for future research in the field.

Technical University of Denmark, Kongens Lyngby.
1st of March 2025.

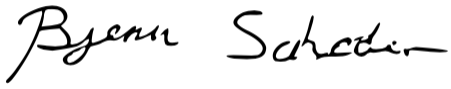

Bjørn Funch Schrøder Nielsen

III Acknowledgements

I extend my sincere thanks to Elizaveta Semenova, my project supervisor, for her guidance and valuable suggestions throughout the project. Her insights were crucial in overcoming the challenges of the project and keeping the work on track.

I also want to express my deepest gratitude to PhD student Christian Ruiz and Postdoctoral researcher Karolina Ewa Polczynska for their advice and supervision. Their expertise in nanoscale fabrication, both theoretical and practical, along with their guidance and support throughout the project, were invaluable to the success of this thesis. Thank you.

My appreciation also goes to the Nanolab staff, especially Conny Hjort and Jesper Yue Pan, for their training and assistance with the Nanolab tools and equipment.

Finally, I am deeply grateful to my family and loved ones for their unwavering support, encouragement, and patience throughout this journey. I know I have often been preoccupied with this work at your expense, and I am truly grateful for the patience and understanding.

Contents

I Summary **1**

II Preface **2**

III Acknowledgements **3**

1 Introduction **6**

2 Theoretical Framework **8**
2.1 Density of States in Quantum Confined Nanostructures 8
2.1.1 Density of States in Bulk Semiconductors 8
2.1.2 Energy Bands and Bandgaps in Bulk Semiconductors 9
2.1.3 Direct- and Indirect Bandgaps in Semiconductors 10
2.1.4 Quantum Confinement 12
2.1.5 Density of States in Quantum Confined Systems 13
2.1.6 Zero Dimensional Quantum Dots 15
2.1.7 Effects of Discrete Density of States in Quantum Dots 16
2.2 Quantum Dot Growth Dynamics and Self-Assembly 18
2.2.1 Principles of Epitaxial Growth 18
2.2.2 Equilibrium Epitaxial Growth and Growth Modes 20
2.2.3 Considerations of III-V Material Systems 22
2.2.4 Strain Effects and Bandgap Engineering in III-V Heterostructures 25
2.3 Deterministic Site-Control Growth of Quantum Dots 27
2.3.1 Strain and the Energy Landscape 27
2.3.2 Spacing and Patterning Effects 29

3 Litterature Review **30**
3.1 Self-Assembly and Quantum Dot Heterostructures 30
3.1.1 Alternative Growth Techniques for Quantum Dot Fabrication 31
3.1.2 Strain effects in deterministic site-controlled quantum dot growth 32
3.1.3 Tuning Electronic and Optical Properties of Quantum Dots 33

4 Experimental Techniques **34**
4.1 An overview of Applied Techniques and Equipment 34
4.1.1 Epitaxial Thin Film Growth 34
4.1.2 E-beam Lithography 34
4.1.3 Wet-Etching of Epitaxial Layers 35
4.1.4 Characterisation 35
4.2 Process Steps 36

4.2.1 Initial growth of Epitaxial Layers . . . 36
4.2.2 Electron Beam Lithography . . . 39
4.2.3 Wet Etching of sample . . . 44
4.2.4 Resist Stripping . . . 46
4.2.5 Quantum Dot Growth . . . 48

5 Fabrication and Characterisation 50
5.1 Fabrication for InGaAs Epitaxy on InP Substrate . . . 50
5.1.1 Epitaxial Growth of InGaAs . . . 50
5.1.2 Pre-treatment and Spin Coating . . . 50
5.1.3 Exposure and Development . . . 51
5.1.4 Etching of InGaAs Epitaxial Layer . . . 53
5.2 Fabrication of Optimised InP/InGaAs/InP Sample . . . 58
5.2.1 Epitaxial Growth of InGaAs and InP . . . 58
5.2.2 Resist Application, Exposure and Development . . . 59
5.2.3 Etching of the InGaAs/InP epitaxial Layers . . . 60
5.3 Fabrication Using Pre-coated InGaAs/InP Sample . . . 63
5.3.1 Etching of InGaAs Epitaxial Layer and Resist Removal . . . 64
5.3.2 Epitaxial Growth of InP Top-layer and InAs Quantum Dots . . . 67
5.3.3 AsH_3-Enhanced Epitaxial Growth for Improved Planarisation . . . 70

6 Conclusion 75

7 Appendix 76
7.1 Exposure Mask Topology Optimisation . . . 76
7.1.1 Problem Definition . . . 76
7.1.2 The Symmetric Solution . . . 77
7.1.3 Optimisation Using Greedy and Simulated Annealing Algorithms . . . 78
7.2 Exposure Mask Generation . . . 80
7.2.1 Compiler . . . 80
7.2.2 Alignment Markers . . . 82
7.2.3 Field Generation . . . 83
7.2.4 Label Generation . . . 84
7.2.5 Scalebar Generation . . . 85
7.2.6 Spacing Visualisation . . . 86
7.3 Process Flow . . . 87
7.4 Critical Thickness Script . . . 90

8 Bibliography 91

1 Introduction

The progressive refinement of microelectronic devices has allowed for the proliferation of computing power, transforming industries and daily life. Continuous improvements in device performance, scalability, and energy efficiency have driven the miniaturization of electronic components to the point where the fundamental limits of classical physics are being challenged. As feature sizes shrink towards the atomic scale, quantum mechanical effects take precedence, placing constraints on conventional semiconductor architectures and driving the development of new innovations that harness these effects.
Among these emerging technologies, quantum light sources play a crucial role in the advancement of quantum information science. In particular, single-photon emitters are essential for applications such as quantum key distribution, quantum computing, and quantum metrology [1]. Among the various quantum emitters explored, self-assembled quantum dots (QDs) have emerged as a promising platform due to their ability to provide high-purity, indistinguishable, and entangled photon pairs [2].

A particularly important spectral region for quantum communications is the telecom C-band (1530-1565 nm), which aligns with the minimum attenuation window of silica optical fibers: These fibers exhibit exceptionally low loss at infrared wavelengths, around 0.2 dB/km [3], making them the backbone of long-distance optical communication networks. Over 95% of the world's data traffic is transmitted through undersea fiber-optic cables operating in this spectral region [4]. Moreover, the telecom C-band enables Dense Wavelength Division Multiplexing (DWDM), where multiple data channels are transmitted simultaneously, significantly increasing optical carrier capacity [5]. While extending transmission into the telecom-L band (1565-1625 nm) can allow for even more data channels, the increased chromatic dispersion at higher wavelengths can introduce pulse broadening effects [6]. Thus, the C-band remains the optimal choice for high-capacity optical communication systems.

Despite the efficiency of silicon-based photonic platforms for guiding light, they suffer from a critical limitation: the inability to generate coherent photons. This issue arises from the centrosymmetric crystal structure of silicon, which forbids second-order nonlinear optical processes such as spontaneous parametric down-conversion (SPDC) [7]. Consequently, alternative material platforms are required for quantum light generation. Among these, InAs/InP quantum dots have demonstrated significant potential as robust single-photon sources, capable of operating in the telecom wavelength range with high efficiency and coherence [8] [9] [10].

A fundamental property of QDs is their ability to confine charge carriers in all three spatial dimensions, leading to discrete electronic states. This quantum confinement effect significantly modifies the density of states, shifting from a continuous spectrum in bulk materials to discrete, atomic-like levels in QDs [11]. Self-assembled QDs are typically formed via the Stranski-

Krastanov growth mode [9], where a few monolayers of material initially grow pseudomorphically as a strained wetting layer before spontaneously forming three-dimensional islands [12] [13]. This self-organization process results in defect-free QDs embedded within a semiconductor matrix, crucial for high-performance optoelectronics [14].
While self-assembly enables spontaneous QD formation, precise control over QD positioning and emission wavelength remains a challenge.

Despite the significant potential of quantum dots as single-photon emitters, achieving high spatial precision in their positioning remains an ongoing challenge in the field. The self-assembly process results in randomly distributed QDs, leading to difficulties in integrating them into scalable photonic architectures. For practical quantum technologies, the deterministic placement of QDs with predefined emission properties is essential.
Strain engineering presents a promising solution to this challenge by providing an effective means of site-controlled QD nucleation. This method could allow for precise control over both the spatial positioning and the optical properties of the QDs, offering a scalable approach to deterministic QD fabrication [15]. Compared to other site-control techniques, such as selective area growth [16], strain engineering minimises material defects and preserves the high optical quality of QDs required for quantum applications.

This project is dedicated to the advancement of epitaxially grown, self-assembled InAs/InP quantum dots, using strain engineering for precise site control. By controlling the intrinsic strain fields that arise during epitaxial growth, the spatial positioning and of these QDs can be finely tuned, offering a scalable approach to deterministic quantum dot fabrication. This methodology is critical for integrating high-quality single-photon emitters into quantum photonic circuits, paving the way for enhanced performance in quantum communication and computation applications.

2 Theoretical Framework

A thorough understanding of the physics governing quantum dots is essential, both conceptually to understand why these nanostructures are viable in the optoelectronics landscape, but also to understand the fabrication process behind them. This section provides the necessary theoretical foundation, outlining the principles of quantum confinement, and strain effects in epitaxial systems.

2.1 Density of States in Quantum Confined Nanostructures

The limitations of traditional silicon-based photonic platforms, as outlined in the previous section, highlight the necessity of exploring alternative materials and fabrication approaches for advanced photonic and quantum communication systems. Since the 1990s [11], QDs have shown promise as the next-generation photonic technologies, owing to their unique quantum confinement effects. These effects enable discrete energy levels and tunable optical properties, making QDs highly versatile for various applications.
Quantum dots are semiconductor nanostructures capable of confining charge carriers in all three spatial dimensions, resulting in atom-like discrete energy states -a concept we will explore momentarily.

2.1.1 Density of States in Bulk Semiconductors

Bulk materials can be understood as material systems that adhere to the classical laws of physics, by having length scales of macroscopic order. For such material systems both electronic and vibrational states in solids form a continuous set of allowed energy levels.
The density of states (DOS) $g(E)$ quantifies the number of available quantum states per unit energy interval.
In the 3-dimensional bulk, the DOS can be expressed as

$$g(E) = \frac{dN}{dE}, \tag{1}$$

which quantifies the number of available states, N, per unit energy, E. However, counting, or rather, estimating individual states directly in energy space is cumbersome [17], and thus we can instead use a more dimensionally-indiscriminate approach, which is to use the fact that quantum states are defined in momentum space, or, k-space.
To derive the DOS in terms of k-space, we count the number of quantum states within a sphere of radius k in reciprocal space, which is proportional to the volume of the sphere:

$$N(k) = \frac{V}{(2\pi)^3} \cdot \frac{4}{3}\pi k^3, \tag{2}$$

where V is the system volume. Differentiating gives the density of states in k-space:

$$g(k) = \frac{dN}{dk} = \frac{V}{2\pi^2}k^2. \tag{3}$$

To express $g(E)$, we use the free-electron dispersion relation:

$$E = \frac{\hbar^2 k^2}{2m^*}, \tag{4}$$

where m^* is the effective electron mass. Differentiating,

$$\frac{dE}{dk} = \hbar^2 \frac{k}{m^*}, \tag{5}$$

allows us to obtain the DOS in terms of energy:

$$g(E)_{3D} = g(k)\frac{dk}{dE} = \frac{V}{2\pi^2}\left(\frac{2m^*}{\hbar^2}\right)^{3/2} E^{1/2}. \tag{6}$$

This expression shows that the density of states in a bulk 3D material scales as $E^{1/2}$.

2.1.2 Energy Bands and Bandgaps in Bulk Semiconductors

The continuous nature of the DOS leads to the formation of well-defined energy bands. These bands are separated by forbidden energy regions, bandgaps, where no electronic states exist.

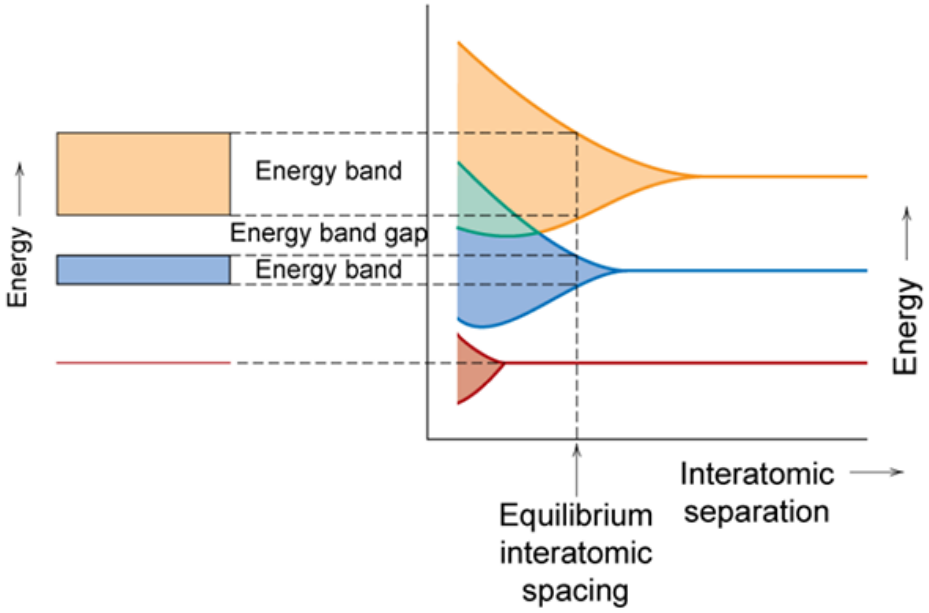

Figure 1: The conventional representation of the electron energy band structure for a solid material at the equilibrium interatomic separation [18] Figure 12.3.

The bandgap energy E_g represents the minimum energy required to excite an electron from the valence band to the conduction band. The formation of the bandgap can be understood through the periodic potential of the crystal lattice, which governs the behavior of electrons in a crystalline solid. As electrons propagate through the periodic potential, their wavefunctions experience constructive and destructive interference due to the periodic arrangement of atoms. This interference causes the splitting of energy levels into continuous energy bands and the opening of bandgaps at certain points in k-space. This is formally described by Bloch's theorem [19]:

In a crystal with a periodic potential $V(\bar{r})$ that satisfies $V(\bar{r} + \bar{R}) = V(\bar{r})$ for any lattice vector $\bar{R}$, the electron wavefunctions can be expressed as:

$$\psi_{n\bar{k}}(\bar{r}) = e^{i\bar{k}\cdot\bar{r}} u_{n\bar{k}}(\bar{r}), \tag{7}$$

where $u_{n\bar{k}}(\bar{r})$ is a periodic function with the same periodicity as the crystal lattice, $\psi_{n\bar{k}}(\bar{r})$ is the electron wavefunction, $\bar{k}$ is the crystal momentum, and n denotes the band index.

According to this theorem, electron wavefunctions in a crystal can be described as plane waves modulated by a periodic function. At specific points in k-space, known as Brillouin zone boundaries, these wavefunctions undergo Bragg reflection, leading to gaps in the energy spectrum—the bandgaps. The width of a bandgap depends on the strength of the periodic potential and the overlap of atomic orbitals in the crystal, making it an intrinsic material property in bulk systems.

Within these allowed energy bands, the DOS describes how the available electronic states are distributed. The continuous nature of the DOS ensures that electrons can always occupy states within the bands, enabling broad absorption and emission spectra. Unlike discrete atomic energy levels, electronic transitions in solids can occur over a wide range of energies, spanning the bandgap and extending throughout the bands.

2.1.3 Direct- and Indirect Bandgaps in Semiconductors

The bandgap of a semiconductor can be classified as either direct or indirect, depending on the relative positions of the conduction band minimum and the valence band maximum in k-space. This distinction determines the efficiency of interband transitions, where an electron is excited from the valence band to the conduction band through the absorption of a photon, provided that the final state in the conduction band is unoccupied, in accordance with Pauli's exclusion principle [20][21].
In a direct bandgap material, the conduction band minimum and the valence band maximum occur at the same value of crystal momentum, generally at the center of the Brillouin zone, $k = 0$. An interband transition in such a material occurs when an electron absorbs a photon with energy $\hbar\omega$ that matches or exceeds the bandgap energy E_g, causing the electron to be excited from the valence band to the conduction band:

$$\hbar\omega \geq E_g. \tag{8}$$

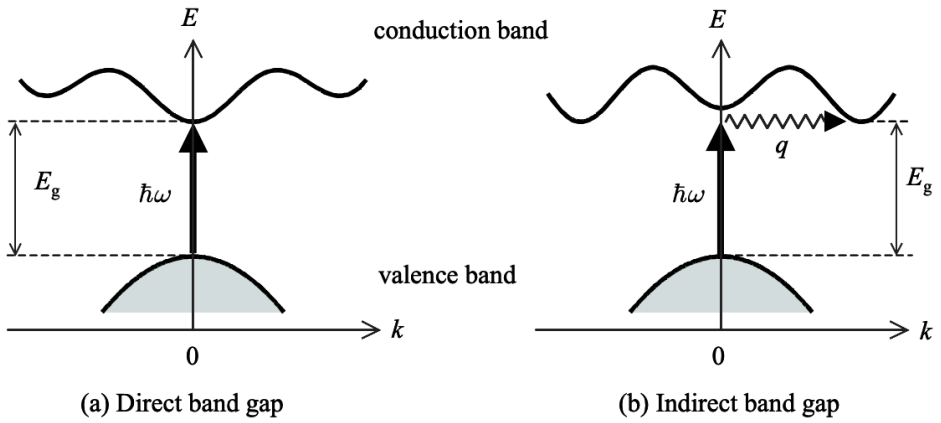

Figure 2: Illustration of direct and indirect bandgaps in semiconductors. (a) In a direct bandgap material, the conduction band minimum and valence band maximum occur at the same crystal momentum $k = 0$, allowing efficient photon emission. (b) In an indirect bandgap material, the conduction band minimum and valence band maximum occur at different k-points, requiring phonon-assistance with momentum q to conserve momentum, making photon emission less efficient. Figure from [20].

Since this transition requires no change in crystal momentum, interband transitions can occur efficiently through the absorption or emission of a photon.
The bandgap energy for a direct bandgap material can be expressed as:

$$E_g = E_c(k = 0) - E_v(k = 0), \tag{9}$$

where $E_c(k)$ and $E_v(k)$ represent the energy levels of the conduction and valence bands, respectively.

In an indirect bandgap material, such as silicon, the conduction band minimum and the valence band maximum occur at different points in k-space. For example, the conduction band minimum may occur near the X-point in the Brillouin zone, while the valence band maximum remains at $k = 0$. As a result, a direct interband transition is not possible without a change in momentum. In this case, the transition requires the involvement of a phonon to provide the necessary momentum transfer:

$$E_g = \hbar\omega_{\text{photon}} + \hbar\omega_{\text{phonon}} = E_c(\mathbf{k_c}) - E_v(\mathbf{k_v}), \tag{10}$$

where $\hbar\omega_{\text{photon}}$ is the photon energy, and $\hbar\omega_{\text{phonon}}$ is the phonon energy.
The need for a phonon-assisted transition makes radiative recombination in indirect bandgap materials much less efficient compared to direct bandgap materials, as the simultaneous involvement of both a photon and a phonon significantly reduces the probability of the transition occurring at all.

2.1.4 Quantum Confinement

TThe derivation we arrived at in Equation 6 describes the density of states in a system where charge carriers can move freely in all three spatial dimensions. This unrestricted motion results in a continuous energy spectrum and well-defined energy bands. However, when the dimensions of a material are reduced to the nanoscale, charge carrier motion becomes restricted, and the system can no longer be adequately described using classical free-particle assumptions. Instead, a quantum mechanical treatment is required.

A natural way to determine when quantum effects become significant is through Heisenberg's uncertainty principle [22], which states that the position and momentum of a particle cannot be simultaneously determined with arbitrary precision:

$$\Delta x \Delta p \geq \frac{\hbar}{2}. \tag{11}$$

Rearranging for the momentum uncertainty in the x-direction gives:

$$\Delta p_x \sim \frac{\hbar}{\Delta x}. \tag{12}$$

This uncertainty in momentum corresponds to an additional kinetic energy contribution due to spatial confinement [20]:

$$E_{\text{confinement}} \sim \frac{\hbar^2}{2m^*(\Delta x)^2}. \tag{13}$$

For quantum confinement to occur, this energy must exceed the thermal energy of the system:

$$E_{\text{confinement}} \gtrsim \frac{1}{2} k_B T. \tag{14}$$

From this, we obtain a characteristic confinement length scale:

$$\Delta x \lesssim \sqrt{\frac{\hbar^2}{m^* k_B T}}. \tag{15}$$

This physical significance of this threshold becomes clear from a wave-mechanical perspective. A charge carrier's momentum is related to its de Broglie wavelength [23]:

$$\lambda_{\text{deBroglie}} \sim \frac{h}{p_x}. \tag{16}$$

Under thermal equilibrium, the typical carrier momentum can be estimated using the equipartition theorem:

$$p_x \sim \sqrt{2m^* k_B T}. \tag{17}$$

Substituting this into Equation 16 gives an approximate expression for the thermal de Broglie wavelength:

$$\lambda_{\text{deBroglie}} \approx \sqrt{\frac{\hbar^2}{m^* k_B T}}. \tag{18}$$

Comparing Equations 15 and 18, we see that the critical confinement length is of the same order as the thermal de Broglie wavelength. This shows that when a materials dimensions approach this scale, the charge carriers can no longer be treated as classical particles, and their wave-like nature dominates—leading to discrete energy levels and quantum confinement. At room temperature, this length scale is typically a few nanometers for electrons in semiconductors, marking the transition from bulk to nanoscale quantum behavior.

2.1.5 Density of States in Quantum Confined Systems

The quantum confinement of charge carriers in nanostructures causes their energy levels to become quantized. This happens because the boundary conditions imposed by the confinement allow only specific wavelengths of the particles' wavefunctions to exist. This quantization of energy levels results in a discrete density of states, in contrast to the continuous DOS of bulk materials.
To illustrate the quantization of the DOS, we will transition from a three-dimensional bulk semiconductor to a two-dimensional quantum well. In this case, the motion of charge carriers is confined to two dimensions, y and z, while the motion in the x-dimension is restricted.

The boundary condition in the confinement direction, x, can be written as:

$$\psi(x) = 0 \quad \text{at} \quad x = 0 \text{ and } x = L, \tag{19}$$

where L represents the width of the quantum well.
Physically, this corresponds to an infinite potential barrier at the boundaries, where the wavefunction of the carrier must vanish.

We can describe the wavefunction of a charge carrier in the quantum well using Schrödinger's equation [24]:

$$-\frac{\hbar^2}{2m^*}\frac{d^2\psi}{dx^2} = E\psi \tag{20}$$

The general solution for the wavefunction is given by:

$$\psi_n(x) = A\sin\left(k_n x\right), \tag{21}$$

where A is the normalization constant, and k_n is the quantized wave vector.

The boundary conditions at $x = 0$ and $x = L$ impose that only specific values of k_n are allowed:

$$k_n = \frac{n\pi}{L}, \quad n = 1, 2, 3, \ldots \tag{22}$$

The quantized wave vectors k_n correspond to discrete momentum, which in turn leads to the quantization of energy levels.

Substituting k_n into the expression for energy of a free particle, from Equation 4, yields the discrete energy levels for a particle confined in a quantum well:

$$E_n = \frac{\hbar^2}{2m^*} \left(\frac{n\pi}{L}\right)^2. \tag{23}$$

We have thereby shown that the energy levels of a particle, experiencing quantum confinement, become quantized.

In a two-dimensional quantum well, motion is confined in the x-direction, while charge carriers remain free to move within the y-z plane. This free movement results in a continuous energy dispersion relation for in-plane motion, as in equation 4, with $k = \sqrt{k_y^2 + k_z^2}$.

To determine the density of states in energy space, we apply the same methodology as we did for the bulk case, by first finding the DOS in k-space, and then relate it to energy space afterwards. In two dimensions, this distribution is uniform and given by:

$$g(k)\, dk = \frac{k}{2\pi}\, dk. \tag{24}$$

We can then use the energy dispersion relation to convert this distribution into Expression 4

$$k = \sqrt{\frac{2m^* E}{\hbar^2}}. \tag{25}$$

Differentiating this relation gives:

$$dk = \frac{m^*}{\hbar^2 k}\, dE. \tag{26}$$

Substituting k and dk into the expression for $g(k)\, dk$, we obtain the density of states in energy space:

$$g(E)\, dE = \frac{k}{2\pi} \cdot \frac{m^*}{\hbar^2 k}\, dE = \frac{m^*}{2\pi\hbar^2}\, dE. \tag{27}$$

However, we still need to account for the spin degeneracy of the charge carriers. Since electrons are fermions with spin $-\frac{1}{2}$, the DOS must be multiplied by a factor of 2 to account for the two possible spin states:

$$g(E)_{2D} = \frac{m^*}{\pi\hbar^2} \tag{28}$$

This derivation demonstrates how quantum confinement affects the density of states in nanostructures. In the simplest case of a 2D quantum well, where motion is confined in one direction but remains free in the plane, the DOS deviates significantly from the continuous bulk behavior. Unlike in 3D materials, the two-dimensional DOS is constant within each allowed subband. However, it is not entirely energy-independent: at each quantized energy level E_n, a new conduction channel opens, causing a discrete jump in the DOS. This leads to step-like behavior seen in quantum wells, where the DOS remains constant within a subband but increases abruptly when a new subband becomes available, as can be seen in the second diagram in Figure 3.

2.1.6 Zero Dimensional Quantum Dots

Extending this concept further, when quantum confinement occurs in all three spatial dimensions, leaving no degrees of freedom for continuous motion, the confinement effects become so pronounced that the of states is reduced to a series of discrete Dirac δ-functions. This confinement regime is known a zero-dimensional system, or quantum dot.

The method to derive the DOS in a quantum dot is similar to the previous derivation for a quantum well, but we instead consider a three-dimensional potential well. The boundary conditions for a quantum dot are nearly the same as seen in condition 19, but extended to each of the confined dimensions:

$$\psi(x, y, z) = 0 \quad \text{at} \quad x = 0 \text{ and } x = L_x, \tag{29}$$
$$\psi(x, y, z) = 0 \quad \text{at} \quad y = 0 \text{ and } y = L_y, \tag{30}$$
$$\psi(x, y, z) = 0 \quad \text{at} \quad z = 0 \text{ and } z = L_z \tag{31}$$

Extending the time-independent Schrödinger equation from Equation 20 to three dimensions,

$$-\frac{\hbar^2}{2m^*}\left(\frac{\partial^2\psi}{\partial x^2} + \frac{\partial^2\psi}{\partial y^2} + \frac{\partial^2\psi}{\partial z^2}\right) = E\psi \tag{32}$$

With the general solution for the wavefunction that satisfies these boundary conditions being a product of standing waves in each direction, (x, y, z):

$$\psi_{n_x,n_y,n_z}(x, y, z) = A \sin\left(\frac{n_x\pi x}{L_x}\right) \sin\left(\frac{n_y\pi y}{L_y}\right) \sin\left(\frac{n_z\pi z}{L_z}\right) \tag{33}$$

In this equation n_x, n_y, and n_z are the positive integer quantum numbers for each dimension that express the quantised modes of motion of an eletron in the quantum dot. Since the wavefunction must vanish at the boundaries (as per the boundary conditions 29-31), we again have a standing wave in each direction, where the quantum numbers convey the number of half-wavelengths.

We can then obtain the energy levels of the quantum dot by substituting the wavevectors into the expression for the particle energy, where all dimensions are considered:

$$E_{nx,ny,nz} = \frac{\hbar^2}{2m^*}\left(\frac{n_x^2\pi^2}{L_x^2} + \frac{n_y^2\pi^2}{L_y^2} + \frac{n_z^2\pi^2}{L_z^2}\right) \tag{34}$$

Just as in the case of the confined direction in a quantum well, the energy levels of a quantum dot are quantized due to the wavefunction vanishing at the boundaries. However, in a quantum well, confinement occurs only in one direction, while the charge carriers remain free to move in the other two directions. As a result, in these free directions, the energy levels remain continuous, similar to the bulk material, whereas quantization occurs only along the confined direction. Since a quantum dot is confined in all directions, the energy levels are exclusively discrete and depend on the quantum numbers n_x, n_y, and n_z, which represent the standing wave modes in

each spatial dimension.
The spacing between these energy levels is governed by the dimensions of the quantum dot, L_x, L_y, and L_z, with smaller dot sizes resulting in larger energy separations due to stronger confinement effects.

Since all energy levels in a quantum system are discrete and correspond to specific quantum states, there are no possible states in-between these levels. This makes the DOS binary in nature: each energy either coincides with a state or falls in a gap where no states are available. This is precisely why we can represent the DOS as a series of Dirac δ-functions, a class of generalised functions that is zero everywhere except at a single point, where it's value is infinite:

$$\delta(x) = \begin{cases} \infty, & x = 0 \\ 0, & x \neq 0 \end{cases} \text{ such } \int_{-\infty}^{\infty} \delta(x)\, dx = 1 \tag{35}$$

The density of states for a quantum dot is consequently expressed as a sum of Dirac δ-functions, each corresponding to a discrete, permitted energy level, given by

$$g(E)_{0D} = \sum_{n_x, n_y, n_z} \delta(E - E_{n_x, n_y, n_z}) \tag{36}$$

where each $\delta(E - E_{n_x, n_y, n_z})$ epresents a quantum state available at the specific energy level, and E is a continuous variable representing the energy at which the density of states is evaluated.
We can write this expression explicitly, by substituting in the energy levels of the quantum dot, that we derived in equation 34:

$$g(E)_{0D} = \sum_{n_x, n_y, n_z} \delta\left(E - \frac{\hbar^2}{2m^*}\left(\frac{n_x^2\pi^2}{L_x^2} + \frac{n_y^2\pi^2}{L_y^2} + \frac{n_z^2\pi^2}{L_z^2}\right)\right) \tag{37}$$

2.1.7 Effects of Discrete Density of States in Quantum Dots

We have now derived the density of states (DOS) for both bulk semiconductors and quantum-confined nanostructures, demonstrating the fundamental differences between these systems. As illustrated in Figure 3, this dimensional dependence of the DOS follows a clear progression: in bulk materials, the DOS is continuous, whereas in lower-dimensional systems, increasing confinement leads to greater quantization. Ultimately, in zero-dimensional quantum dots, the DOS becomes entirely discrete, consisting of a series of Dirac delta functions, with no continuous states.
This transition from a continuous to a discrete DOS fundamentally alters the material's optical properties. In bulk materials, the continuous DOS enables electronic transitions between any occupied state in the valence band and any unoccupied state in the conduction band. As a result, absorption occurs over a broad range of energies, leading to wide and featureless absorption spectra. In contrast, the discrete DOS of quantum dots restricts electronic transitions to well-defined energy levels, producing narrow, sharply defined spectral features.

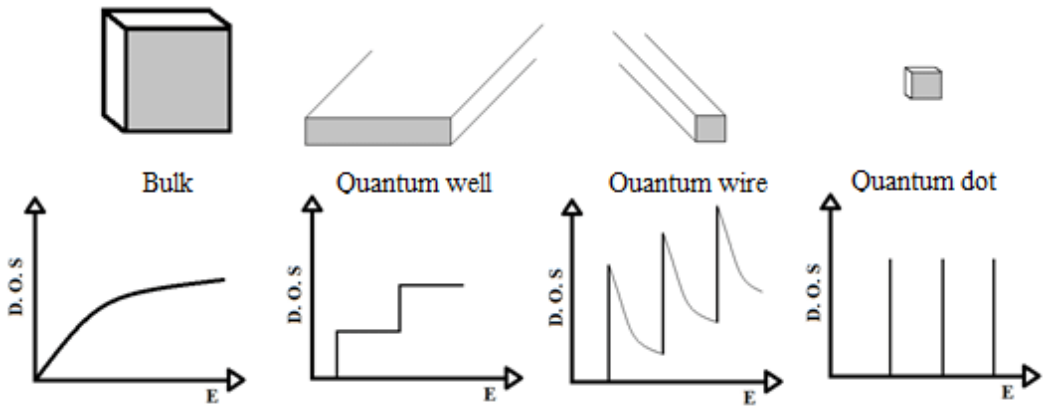

Figure 3: Dimensional dependence of the density of states, showing the transition from a continuous DOS in bulk materials to discrete energy levels in quantum dots. Figure from [25].

This distinction is equally important for electron-hole recombination processes, which determine the material's optical emission properties. There are two main types of recombination: radiative and non-radiative. Radiative recombination, the process in which an electron in the conduction band recombines with a hole in the valence band, results in the emission of a photon. The efficiency of radiative recombination is quantified by the quantum efficiency, η, which is defined as the ratio of emitted photons to total electron-hole recombination events [26]:

$$\eta = \frac{n_{\text{photons}}}{n_{\text{recombination}}}. \tag{38}$$

Following up on the point from Section 2.1.3, the efficiency of this process is strongly influenced by whether the material has a direct or indirect bandgap. In direct bandgap materials, the valence band maximum and conduction band minimum occur at the same wavevector (k-point), ensuring efficient optical transitions.

Quantum dots, with their discrete DOS, further enhance radiative recombination efficiency. The restriction of charge carriers to quantized energy levels increases the probability of radiative recombination while suppressing competing non-radiative processes. The energy of the emitted photon is directly determined by the energy separation between quantized conduction and valence band levels, given by:

$$E_{\text{photon}} = E_c(n_x, n_y, n_z) - E_v(n'_x, n'_y, n'_z), \tag{39}$$

where E_c and E_v are the quantized conduction and valence band energy levels, respectively. A key advantage of quantum dots is that these energy levels—and consequently the emitted photon energy—are highly tunable. By adjusting the physical dimensions of the quantum dot (L_x, L_y, L_z), the bandgap can be precisely engineered, allowing for emission at specific wavelengths with high spectral purity.

2.2 Quantum Dot Growth Dynamics and Self-Assembly

Fabricating quantum dots with controlled size and distribution is crucial for performance and properties. A widely used approach is to exploit certain reactions and surface physics that promote spontaneous aggregation of materials into well-defined structures.
This process is known as quantum dot self-assembly, and is specifically a process, where elastic strain relaxation leads to spontaneous generation of three-dimensional islands on the nanometer scale [27]. Self-assembly occurs during epitaxial growth, wherein the deposited material forms a thin film on a substrate, with the lattice parameters of the thin film closely matching those of the underlying substrate.

2.2.1 Principles of Epitaxial Growth

Epitaxial growth is a process in which a crystalline material is deposited onto a crystalline substrate in such a way that the deposited layer adopts a well-defined crystallographic orientation that is determined by the underlying substrate [28]. The introduced atoms diffuse across the substrate surface and integrate into the underlying crystal lattice, and thus the process requires that the lattice parameters of the deposited material to closely resemble the substrate's and for the crystal orientations to be aligned. When these conditions are met, the result is a high-quality, monocrystalline thin film with precisely controlled dimensions, down to individual atomic layers, depending on the deposition technique used.

The introduced, unbound, atoms, called adatoms, undergo a three-step process during epitaxial growth [27][28][29], which can be seen in Figure 4: The process begins with the deposition of adatoms onto the substrate surface. At this stage, the adatoms are not yet chemically or physically incorporated into the substrate and it's crystalline lattice. Instead, they adhere weakly to the surface through van der Waals forces or ionic interactions, a process known as adsorption. These interactions allow the adatoms to remain mobile in the plane, enabling mobility across the surface, while still sticking to the surface.

After adsorption, the adatoms undergo surface diffusion, migrating across the substrate in search sites that minimises the free energy (see Figure 4). These sites are typically associated with topology changes such as steps, defects, or seeds, which offer more bonding opportunities. By settling at these locations, the adatoms reduce their free energy by minimizing the number of unsaturated bonds. As adatoms accumulate at these favorable sites, small clusters form, which act as nucleation centers. These nuclei then become seeds that promote further growth by attracting more adatoms to join them.

In the final stage, the clusters formed during nucleation grow larger as additional adatoms attach to them. Over time, the clusters expand and begin to merge with one another, leading to the

formation of larger, connected structures. This process continues until the clusters coalesce to form a continuous and uniform thin film across the substrate surface.

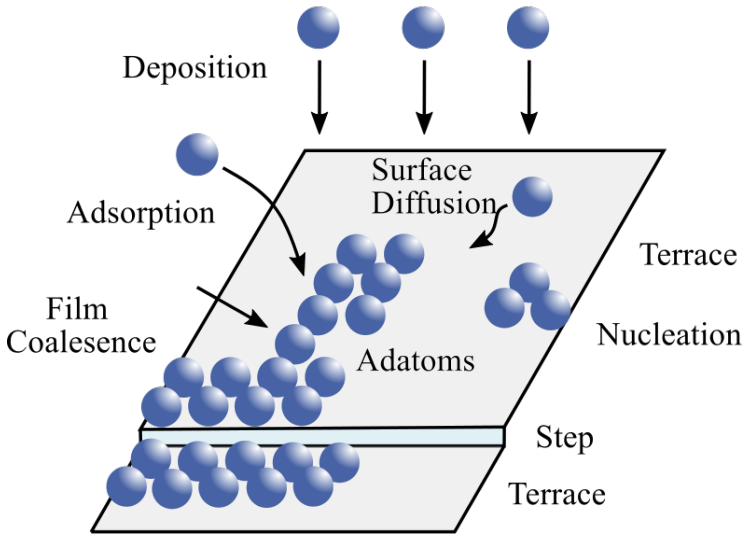

Figure 4: Schematic illustration of epitaxial growth, showing the sequential processes of deposition, adsorption, surface diffusion, nucleation, and film coalescence. Adatoms initially adsorb onto the substrate surface, migrate to energetically favorable sites, and eventually form a continuous crystalline film. From [28], Figure 2.1.

One of the components of calculating the free energy, is the free energy associated with strain. This strain energy arises from the mismatch in lattice parameters between the film and the substrate, where thelattice mismatch can quantified as

$$f = \frac{a_{\text{film}} - a_{\text{substrate}}}{a_{\text{substrate}}} \tag{40}$$

where f represents the relative lattice mismatch. A positive value of f indicates that the film is under compressive strain, meaning the lattice of the film is forced into a more compact configuration than in its unstrained state to accommodate the substrate. Naturally, a negative value of f then corresponds to tensile strain, where the film is stretched relative to its natural lattice parameter.

This lattice mismatch influences the growth dynamics of the film, as it alters the surface energy landscape, affects the film's critical thickness, and plays a crucial role in defect formation and the overall growth mode.

2.2.2 Equilibrium Epitaxial Growth and Growth Modes

When each of the outlined stages operates in a manner that minimizes the free energy, the growth is said to be in equilibrium. Under these conditions, adatoms can diffuse across the surface and settle into a nearly global free energy minimum. It should be mentioned that although metal-organic vapour-phase epitaxy does not occur under strict thermal equilibrium conditions, due to kinetic limitations, precursor decomposition, and more, this model still provides a useful framework for understanding surface diffusion and adatom incorporation. A more detailed discussion of these non-equilibrium aspects in MOVPE is provided in 4.2.1. In a state ideal of thermal equilibrium, the growth process can be described by the thermodynamic energy balance model [27][28], which relates the surface energies of the substrate-gas (B_g), overlayer-gas (A_g), and substrate-overlayer (AB) interfaces:

$$\gamma_{\text{Bg}} = \gamma_{\text{Ag}} \cos(\theta) - \gamma_{\text{AB}} + Ck_BT \cdot \ln(\rho) \tag{41}$$

This equation describes the free energy of the film-substrate system, where each term represents a contribution from different interfacial interactions.
On the left-hand side, γ_{Bg} represents the surface energy of the bare substrate in contact with the surrounding gas before deposition occurs.
On the right-hand side, the first term, $\gamma_{\text{Ag}} \cos(\theta)$, corresponds to the surface energy of the deposited film in contact with the gas. The factor $\cos(\theta)$ accounts for the spreading behavior of the material, as the film adapts its shape based on its interaction with the substrate.
The second term, $-\gamma_{\text{AB}}$, represents the interface energy between the deposited film and the substrate, which influences adhesion and wetting properties.
The final term, $Ck_BT \cdot \ln(\rho)$, accounts for the elastic strain energy, where C is the elastic modulus of the film, quantifying its resistance to deformation, and ρ describes the driving force for deposition.

By evaluating the equilibrium Equation in 41, we can understand the growth mode of the film [27][30]; Should $\theta > 0$ in equation 41, the left handside is less than the right handside, and the energy costs of adatoms dispersing across the surface becomes too high. Instead, the adatams will cluster together to minimize the free energy, favouring adatom-adatom interactions more than adatom-substrate interactions. This reduced homogeneous spreading, and increased clustering of adatoms, leads to formation of three-dimensional islands, and is typically observed when the two materials have a large lattice mismatch. We can essentially see this as the "compatibility" between the film and the substrate. If the lattice of the film has to deform a great deal to match the substrate, incoming adatoms can relax the lattice requirements by sticking to other adatoms, that favour the same lattice parameters. This relaxation of the lattice strain is a lower energy configuration, compared to the strained lattice that arises from a large lattice mismatch, and therefore clustering becomes a more favourable growth mode. This is known as Volmer-Weber growth

Another growth mode is the Frank-van der Merwe growth mode . If instead the lattice mismatch is relatively small, the compatibility of the lattices is high, making spreading more energetically favourable than clustering, and $\theta = 0$. In this case, the left handside of equation 41 becomes

greater than the right handside. In this case, the adatoms will spread across the surface, and the result will be a lightly strained continuous thin film. This process will repeat, building each thin film layer on top of the previous one, until relaxation of the lattice strain becomes more favourable. We can quantify how many layers that can be deposited before relaxation takes effect by the Matthews-Blakeslee theory[31], calculating the critical thickness of the film[32]:

$$h_c = \frac{b}{4\pi f(1+\nu)}\left[\ln\left(\frac{h_c}{b}\right)+1\right] \tag{42}$$

where f is the lattice mismatch as calculated in equation 40, b is the burgers vector, and ν is the Poisson ratio of the underlying substrate.
Up until this critical thickness is reached the film itself will be largely defect-free, but beyond this point relaxation introduces misfit dislocations [27].

The Stranski-Krastanov growth mode is a hybrid of the two growth modes, and is observed when the lattice mismatch is between the upper limit of $\sim 2\%$ required for Frank-van der Merwe growth and the lower limit of $\sim 7\%$ indicative of the Volmer-Weber mode [27]. Here, the adatoms spread across the surface, just as in the Frank-van der Merwe growth, forming an initial two-dimensional thin film layer, after which any further growth spontaneously transition into the clustering process of the Volmer-Weber growth mode, forming small three-dimensional clusters on top. This is the self-assembly process, and it can divided into 4 steps [33]:

The first step is the layer-by-layer growth in the beginning, where the crystal lattice of the film is strained to match that of the substrate. Generally, the first mono-layers are formed one by one, as seen in Figure 5a.
The next step occurs at a certain threshold thickness of the initial layers, where clustering begins to dominate. This starts the formation of stand-alone islands, as seen in Figure 5b, where certain areas of begin to vary in topology, adsorbing nearby adatoms, even consuming nearby adatoms from the monolayers below it, as the energy associated with remaining bonded in an unsaturated manner in the monolayer under strain can be greater than the energy of participating in clustering.
It is in the third step growth of the islands becomes dominant, as a feedbackloop encourages even more adatoms, both from the established monolayers and from the deposition vapours, to join the islands.
Finally, the islands grow to a size where it is no longer energetically favourable for them to consume more adatoms, as adatoms from the thin film monolayers now have to overcome a higher energy barrier to join the islands. At this point, the islands have become well-defined topologically as can readily be seen in the Monte Carlo simulations of SK growth in Figure 5d.

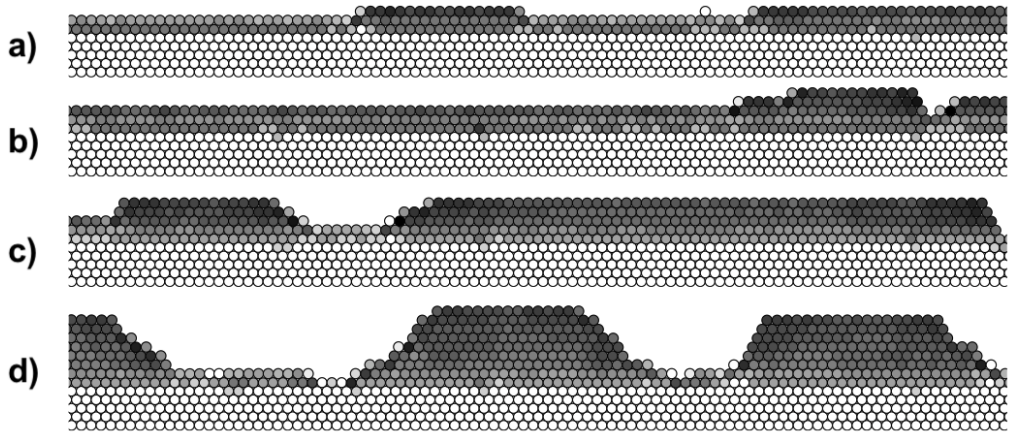

Figure 5: Monte Carlo simulation of Stranski-Krastanov growth, showing the different stages of the process: (a) Initial layer-by-layer growth, where the film remains strained to match the substrate lattice. (b) Clustering as the film reaches a critical thickness, leading to local topological variations. (c) Growth of islands as adatoms migrate from monolayers and deposition vapors, reinforcing the clustering process. (d) Fully developed islands, where further adatom incorporation becomes energetically unfavorable, stabilizing the morphology. Figure from [33].

2.2.3 Considerations of III-V Material Systems

We have now established the principles of self-assembled epitaxial growth and the different growth modes governed by lattice-mismatch induced strain, and we can therefore turn to more holistic properties of strain in heterostructures. Besides influencing growth dynamics, strain also has an impact on the electronic structure of the material, band alignments, carrier mobility, and optical properties, by physically deforming the crystal lattice.

For quantum dot fabrication and thin film heterostructures, the most common class of materials are the III-V semiconductor family, in which elements from groups III and V of the periodic table form alloys [29][34][35].

Unlike silicon, which is a group-IV semiconductor that forms stable covalent bonds with itself, III-V materials consist of elements from different groups of the periodic table. Despite this compositional difference, both types of semiconductors rely on strong covalent bonding within their crystal lattice to achieve structural stability. Bulk single crystals of semiconductors, whether group-IV or III-V, are typically grown using the Liquid Encapsulated Czochralski method [29], in which a seed crystal is submerged into a molten solution of the material and then slowly pulled out, allowing the material to crystallize with the same orientation as the seed.
This process yields highly ordered covalent mono-crystalline structures with high atomic coordination, resulting in strong interatomic bonding and relatively low defect densities.

Regardless of whether the material is a group-IV, III-V, or even II-VI semiconductor, the atoms

arrange into a periodic lattice structure, such as the diamond cubic structure in silicon and germanium, or the zinc blende structure in GaAs and InP. The periodic arrangement of atoms in the lattice creates a repeating potential that fundamentally shapes the material's properties: The charge carriers do not behave as independent free particles but are instead governed by the periodic potential of the crystal lattice:

$$V(\bar{r}) = V(\bar{r} + \bar{R}), \tag{43}$$

for any lattice translation vector $\bar{R}$. This periodic potential leads to the formation of energy bands, governing the material's electronic structure.
The periodic potential imposed by the crystal lattice changes the behavior of carriers, and their wavefunctions take the form of Bloch states [19]:

$$\psi_{n\bar{k}}(\bar{r}) = e^{i\bar{k}\cdot\bar{r}} u_{n\bar{k}}(\bar{r}), \tag{44}$$

where $u_{n\bar{k}}(\bar{r})$ is a periodic function, n denotes the band index, and $\bar{k}$ is the crystal momentum. Bloch's theorem states that in a periodic potential, electronic states must satisfy this form, leading to the emergence of distinct energy bands, described by the dispersion relation $E_n(\bar{k})$.

The morphology of the bands and bandgaps, the positions of the valence band maximum and conduction band minimum in k-space, depends on the symmetry of the electronic wavefunctions. Therefore, this symmetry directly dictates whether the material has a direct or indirect bandgap.

The character of the bandgap stems from the atomic orbital contributions to the electronic states at the band edges. In group-IV semiconductors like silicon, both the conduction and valence bands originate from the same atomic species, resulting in highly symmetric bonding interactions. The electronic states near the band edges primarily involve sp^3 hybridized orbitals, forming an extended covalent network with significant orbital overlap. However, this symmetry in bonding leads to a conduction band minimum that is not located at the center of the Brillouin zone ($k = 0$, also known as the Γ-point), as the valence band maximum, but instead at a different momentum point, such as the X, or L point in silicon [29].
This displacement of the conduction band minimum arises because at Γ, the conduction band primarily consists of s-like orbitals, which do not strongly hybridize with the valence band states, leading to a relatively high energy at this point. In contrast, at X and L, the conduction band states experience stronger orbital mixing, particularly with p-like and higher-order orbitals, which lowers the energy of these states [36][37]. As a result, silicon and germanium exhibit an indirect bandgap, where the lowest-energy optical transitions require a phonon to assist in momentum conservation.

In contrast, for III-V materials like GaAs and InP, the valence band maximum is predominantly derived from the p-orbitals of the group-V element, while the conduction band minimum originates from the s-orbitals of the group-III element. This difference in atomic species breaks the symmetry present in group-IV semiconductors, allowing for stronger s-p hybridization at Γ

and stabilizing the conduction band minimum at the Brillouin zone center [37][29]. This yields efficient optical transitions, as the lowest-energy transitions can occur without phonon assistance.

Beyond having a direct bandgap, some III-V semiconductors also exhibit significantly higher carrier mobility compared to silicon. This enhanced mobility arises from the lower effective mass of electrons in these materials, which affects how electrons and holes propagate through the crystal lattice[38].
Charge transport in semiconductors is based on the curvature of the electronic dispersion relation, defined in Equation 4, which expresses how energy varies as a function of crystal momentum. For many semiconductors, particularly near the conduction band minimum, this relation can be well approximated by a parabolic function, like the kinetic energy of a free electron.
In the expression, the effective mass is the influence of the periodic crystal potential on charge carrier dynamics. Unlike the free electron mass m_e, the effective mass incorporates the band structure effects, reflecting how easily charge carriers accelerate under an applied force. This property emerges naturally from the curvature of the dispersion relation; a band structure with a sharp curvature corresponds to a small effective mass, while a flatter band results in a larger effective mass. Mathematically, the effective mass is related to the second derivative of $E(k)$ [39]:

$$\frac{1}{m^*} = \frac{1}{\hbar^2}\frac{\partial^2 E}{\partial k^2}. \tag{45}$$

Physically, this means that charge carriers in materials with a lower effective mass respond more readily to an applied electric field, as Newton's second law in the crystal lattice takes the form:

$$\hbar\frac{dk}{dt} = -eE, \tag{46}$$

where E is the applied electric field. Since velocity is given by the group velocity relation,

$$v = \frac{1}{\hbar}\frac{\partial E}{\partial k}, \tag{47}$$

a smaller effective mass results in a steeper energy gradient, meaning that electrons accelerate more easily under an external field. Consequently, materials with a lower effective mass exhibit higher carrier velocities and greater overall mobility.
For instance, in GaAs, the electron effective mass is approximately $0.067m_e$, significantly lower than the $0.19m_e$ in silicon [40]. This lower effective mass reduces the inertia of charge carriers, allowing them to achieve higher velocities. Furthermore, a smaller effective mass also leads to a reduction in scattering, as charge carriers experience less resistance when propagating through the lattice.

2.2.4 Strain Effects and Bandgap Engineering in III-V Heterostructures

Besides these intrinsic electronic properties, III-V materials can be further tuned. Strain plays a fundamental role in shaping the electronic structure of III-V semiconductors, altering the curvature of the electronic bands and therefore, the effective mass and mobility of charge carriers. The biaxial strain arising from a mismatch in lattice dimensionality, as discussed earlier, modifies the material's electronic band structure, due to the deformation potential interactions.
Essentially, the equilibrium atomic positions shift, modifying the local electrostatic potential, and as a result, the conduction and valence band edges shift in energy, modifying the intrinsic bandgap of the material. The bandgap of a strained semiconductor is related to that of the unstrained material by the first order approximation [37]:

$$E_g^{\text{strained}} = E_g^{\text{unstrained}} + \Delta E_c + \Delta E_v, \tag{48}$$

where ΔE_c and ΔE_v correspond to strain-induced shifts in the conduction and valence band edges, respectively. Under uniform strain, these energy shifts can be expressed as:

$$\Delta E_c = a_c f, \quad \Delta E_v = b_v f, \tag{49}$$

where a_c and b_v are material-dependent deformation potential constants, and f is the relative lattice strain, as per Equation 40. The sign and magnitude of these shifts depend on whether the strain is tensile or compressive, with tensile strain typically reduces the bandgap by bringing the conduction and valence band edges closer together, while compressive strain increases the bandgap by pushing these bands apart [41][42].
Figure 6 shows the change in the energy bandgap, E_g, as a function of the lattice constant for a range of III-V semiconductor materials and semiconductor-alloys.
From the figure is is clear that an inverse correlation exists for some III-V's between the lattice constant, and the bandgap energy, with material combinations with smaller lattice constants generally having more pronounced bandgaps.

As the lattice expands, the overlap between atomic orbitals is reduced, narrowing the electronic bandgap, and thereby lowering the energy barrier for carrier transitions. Conversely, materials with a more compact lattice exhibit stronger wavefunction overlap, increasing the bandgap [41].

The selection of materials in the diagram are grouped based on their binary and ternary compositions, demonstrating that the bandgap can be tuned by varying the proportion of constituent elements. Ternary compounds such as $In_{0.53}Ga_{0.47}As$ are positioned between their binary endpoints, showing that we can engineer specific material properties through compositional variation.
For $In_xGa_{1-x}As$, Vegard's law provides an approximation of the lattice constant:

$$a(x) = x a_{\text{InAs}} + (1 - x) a_{\text{GaAs}}, \tag{50}$$

where a_{InAs} and a_{GaAs} are the lattice constants of the binary endpoints.

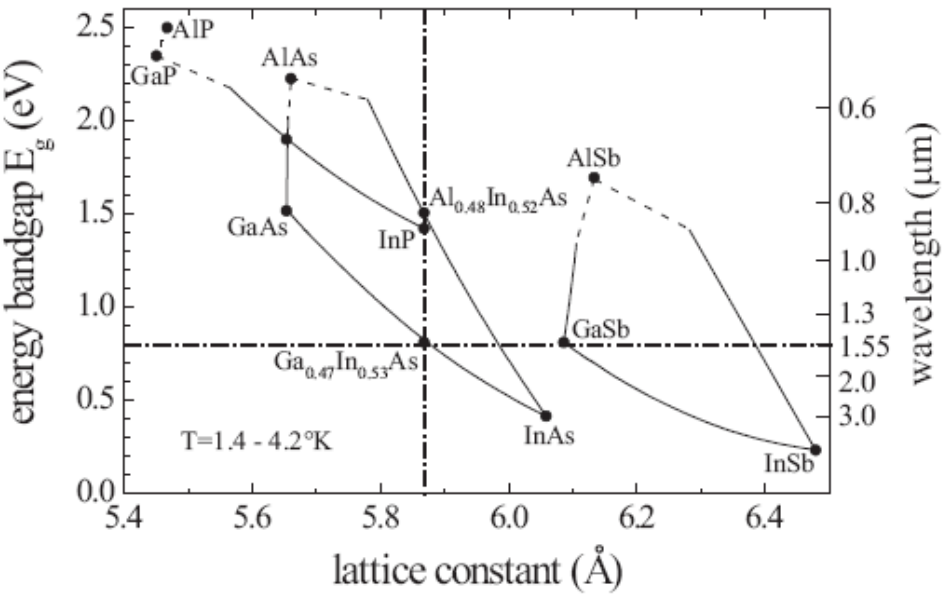

Figure 6: Bandgap energy E_g vs. lattice constant for III-V semiconductors. The inverse correlation reflects how increased lattice spacing reduces orbital overlap, lowering the bandgap. Ternary alloys demonstrate bandgap tunability via compositional engineering. The right axis shows corresponding photon wavelengths. Figure from [42].

A particularly important material system within the Telecom C-band is the InP/InGaAs system, which has been widely explored for its tunable electronic and optical properties. Indium phosphide (InP), with a lattice constant of approximately 5.87 Å and a bandgap of 1.344 eV [43], serves as a common substrate for $In_xGa_{1-x}As$ alloys, where the bandgap and lattice constant can be adjusted by varying the indium content. As the indium composition increases, the lattice constant expands, and the bandgap narrows, approaching the properties of InAs (lattice constant 6.06 Å, bandgap 0.36 eV [44]). This tunability is crucial for longer-wavelength photonic devices. $In_{0.53}Ga_{0.47}As$, which is lattice-matched to InP, exhibits a bandgap of approximately 0.74 eV, corresponding to an optical emission wavelength of 1.55 μm, where fiber optic transmission loss is minimal. This makes it an ideal material for telecommunication lasers and photodetectors. However, when InGaAs with lower indium content is grown on InP, compressive strain is introduced, increasing the bandgap. Conversely, higher indium content leads to tensile strain, reducing the bandgap, which is beneficial for long-wavelength infrared detection.

2.3 Deterministic Site-Control Growth of Quantum Dots

The quantum dot growth explored in the previous section is inherently stochastic, relying on strain-driven self-assembly to spontaneously nucleate nanostructures at energetically favorable sites, which, as mentioned, can be at defect sites, foreign particles, or simply from a random seeding adatom.
While this process is highly efficient and widely used, the random spatial distribution of self-assembled quantum dots presents challenges for applications requiring precise positioning and uniformity. The placement of quantum dots directly influences their optical and electrical interactions, impacting coupling efficiency and leading to variations in size, shape, and composition, which in turn contribute to inhomogeneous broadening of optical emission and inconsistencies in electronic properties.
To overcome these limitations, deterministic site-controlled growth offers an alternative approach, in which lithographically pre-patterned substrates are used to guide nucleation at predefined locations [45].

2.3.1 Strain and the Energy Landscape

In conventional Stranski-Krastanov growth, a thin wetting layer initially forms coherently on the substrate. However, as the lattice mismatch strain builds up, the system transitions from two-dimensional layer growth to three-dimensional island formation to minimize its elastic energy [46], a process we covered in detail in the previous section.

In the case of deterministic site-controlled growth, pre-patterning of the substrate modifies the local strain distribution, creating sites that promote nucleation. The introduction of pits, recesses, or mesas alters the strain energy landscape, by providing regions of local strain accumulation or relaxation [47] [15].
The redistribution of strain determines whether quantum dots nucleate at pit centers, edges, or beneath overgrown recesses, depending on the material system. Prior experiments have shown that, in III-V heteroepitaxial growth, strain accumulates either at the pit centers or peripheries, depending on the fabrication method and overgrowth thickness [48, 47]. This is illustrated in Figure 7, which depicts the transition from an initially coherent wetting layer to the formation of strain-driven 3D islands. As the lattice mismatch strain builds up, the elastic energy landscape changes dynamically, directing adatom diffusion and favoring nucleation at sites of localized strain accumulation.

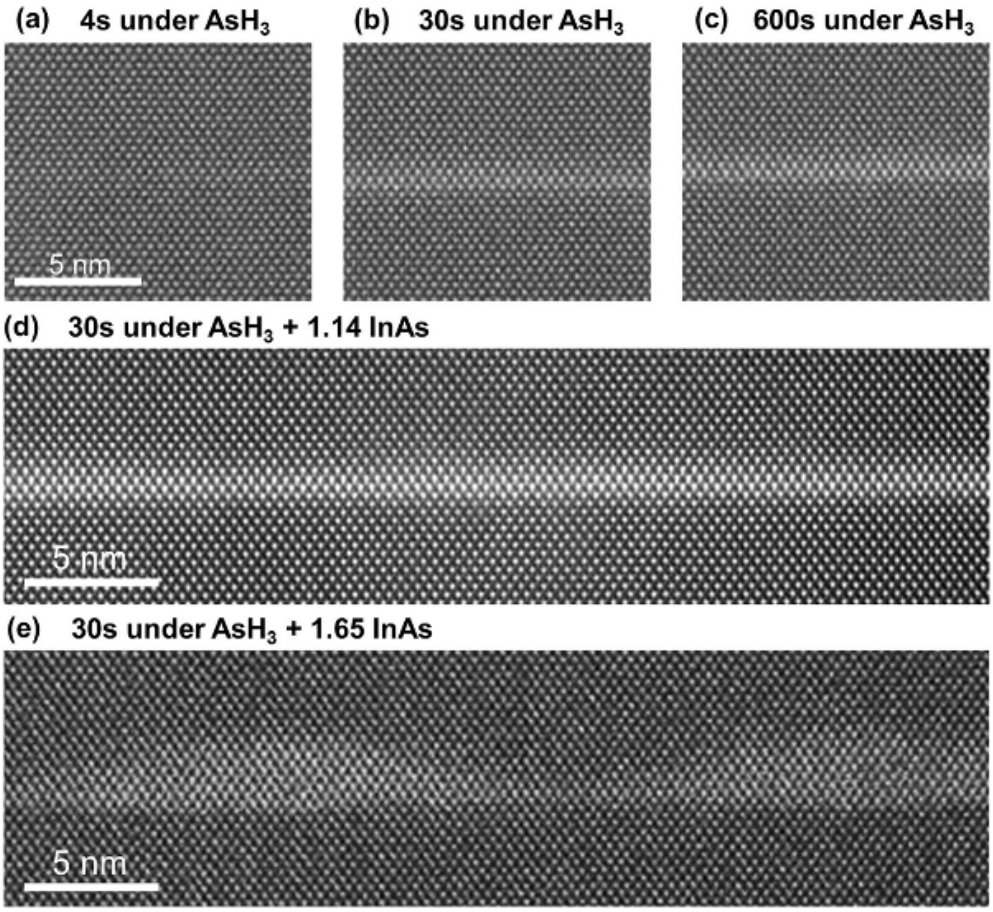

Figure 7: Cross-section HAADF STEM images illustrating the transition from two-dimensional wetting layer growth to three-dimensional quantum dot formation due to strain accumulation. The images show InAs layers formed after InP annealing in an AsH_3. The redistribution of strain dictates nucleation sites, influencing deterministic quantum dot positioning. Figure from [9].

The strain energy density for such a heteroepitaxial system is given by the expression [49]:

$$U_s = \frac{1}{2} C_{ijkl} \varepsilon_{ij} \varepsilon_{kl}, \tag{51}$$

where C_{ijkl} is the elastic stiffness tensor of the material, and ε is the elastic strain tensor, where the lattice mismatch, Equation 40, is the primary component. Both of these are inherent material properties that dictate how strain energy is stored and redistributed during epitaxial growth: When a top layer is grown over a patterned heteroepitaxial interface, the strain energy density is redistributed based on the local compliance of the materials involved, with regions where the overgrown material has a higher stiffness, the system retains more strain energy, potentially leading to enhanced strain-driven nucleation at these locations [50].

2.3.2 Spacing and Patterning Effects

The spatial arrangement and geometry of nucleation sites significantly influence QD formation by modifying both the local and global strain field, and diffusion dynamics. While local strain near or on top of a filled hole governs the individual nucleation events, the collective interaction of neighbouring strain fields dictates whether QDs form in strain-wise isolation or exhibit strain-mediated coupling effects [51].
The shape and dimensions of predefined nucleation sites influence adatom mobility, thereby affecting dot morphology and size distribution. Larger or deeper pits provide an extended surface for adatom accumulation, increasing the likelihood of multiple QD nucleation per site. This has been observed in structured GaAs substrates, where hole depth and diameter directly correlate with QD occupation numbers [52]. In contrast, asymmetric site geometries, such as elongated trenches or anisotropic etch profiles, induce directional strain relaxation, leading to the formation of elongated quantum dots [53]. This phenomenon arises because strain relaxation is anisotropic, occurring preferentially along certain crystallographic directions, thereby influencing both the shape and alignment of QDs [54, 15, 48].

The spacing between nucleation sites determines the degree of strain field overlap, directly affecting QD size uniformity and ordering. When sites are closely spaced, the overlapping elastic interactions modify the local strain energy density, leading to strain-assisted coalescence or ordering effects, where dots preferentially nucleate in clusters rather than as isolated structures [51, 55]. This effect has been experimentally observed in site-selective growth on GaAs substrates, where the local accumulation of adatoms within patterned pits is highly dependent on both spacing and hole shape [52].
At large separations, QDs nucleate with greater independence, as strain fields remain localized to individual pits. This reduces collective strain effects, leading to enhanced spatial uniformity and better-defined dot sizes. Conversely, when nucleation sites are too closely packed, merging strain fields redistribute material, disrupting the self-assembly process and promoting the formation of elongated or clustered structures instead of isolated dots [52].

3 Litterature Review

3.1 Self-Assembly and Quantum Dot Heterostructures

Strain-induced self-assembly has been an observed phenomenon in epitaxial growth since the mid-1980s. Initially, it was seen as an inconvenience in the fabrication of thin films due to its tendency to spontaneously disrupt uniform layer growth. However, as highlighted by Kuech, Bhattacharya, and Bansal [27], this effect was later harnessed as a method for creating defect-free self-assembled quantum dots. Their review provided a holistic discussion on the physics governing self-assembly in semiconductor epitaxy, particularly emphasizing the role of elastic strain relaxation in controlling QD size and uniformity. Through detailed experimental and theoretical analysis, they demonstrated that beyond a critical thickness defined by the Blakeslee model (42), the initially uniform two-dimensional film undergoes a spontaneous transition into three-dimensional islands. This transition, now classified as the Stranski-Krastanov growth mode, has since become a cornerstone of QD fabrication in strained heteroepitaxial systems.
The formation of self-assembled QDs has been extensively studied across various semiconductor material systems, with InAs/GaAs and InAs/InP emerging as some of the most well-characterized platforms. Further work in the spontaneous ordering of coherently strained QDs was investigated in the review by Ledentsov et al. [56]. In the review, they covered island nucleation and size distribution are dictated by a competition between strain-driven thermodynamic minimization and kinetic growth constraints.

The work by Kuech, Bhattacharya, and Bansal [27] further explored how growth parameters such as substrate temperature, deposition rate, and alloy composition influence the self-assembly process. By tuning these conditions, researchers have achieved significant control over QD morphology, directly leading to control of emission wavelengths across a broad spectral range ranging from 1033 nm (0.6 eV) to 2066 nm (1.2 eV).
The impact of substrate temperature on QD formation is particularly significant. For InAs QDs grown on GaAs substrates, it was been observed that the density of self-assembled islands decreases with increasing temperature, ranging from approximately 10^{12} cm^{-2} at 400°C to 0.5×10^10 cm^{-2} at 500°C, using MBE. This trend is attributed to the increased surface diffusion length of adatoms at higher temperatures, which reduces nucleation density and favors the formation of larger QDs. However, excessive temperatures can lead to desorption of adatoms, adversely affecting the QD size distribution.
Besides the temperature, it also showed taht the deposition rate plays a crucial role in determining the QD morphology. Higher deposition rates lead to an increased island density due to a higher adatom flux, which shortens the diffusion length and promotes nucleation at multiple sites.
A similar behavior was covered for InAs QDs grown using MOVPE on InP substrates, in the same review. The study demonstrated a strong correlation between QD morphology and photoluminescence spectra, showing that larger QDs correspond to lower transition energies. AFM

histograms revealed that at a QD height of just below 5 nm, which was produced by MOVPE growth at 6.5 monolayers per second, the QD density could reach values as high as 10^{10} cm^{-2}, with a narrow size dispersion.
As the study increased the growth rate to $9s^{-1}$, the density decreased significantly by an order of magnitude, which proposes a scaling relation, where larger islands form at the expense of smaller ones. This trend is consistent with the established strain-driven mechanism, wherein surface diffusion promotes the redistribution of material from smaller QDs into larger structures.
Also in the review, a direct correspondence was observed between the QD size distribution and the photoluminescence emission peaks, with smaller dots emitting at higher energies of 1.03 eV, while larger QDs exhibited redshifted transitions near 1.10 eV [27]. This aligns well with theoretical band-structure calculations for InAs/InP QDs, which predict a shift in ground-state transition energies due to size-dependent quantum confinement effects.

3.1.1 Alternative Growth Techniques for Quantum Dot Fabrication

While the SK growth mode remains the dominant approach in the fabrication of self-assembled QDs, alternative growth methods such as Droplet Epitaxy, DE, and Molecular Beam Epitaxy, MBE, have been explored to avoid some of the limitations inherent to strain-driven self-assembly. This was demonstrated in the work by Holewa et al. [57], which investigates the synthesis of InAs/InP QDs using DE, yielding highly symmetric quantum dots with a low fine-structure splitting of approximately $(50 \pm 5)\,\mu$eV.
This is fundementally different to the SK-grown QDs that has been outlined in this thesis, where the inherent strain-induced anisotropy typically results in a much larger FSS, leading to significant energy level splitting, which makes the energy levels non-degenerate, which could be a desirable property for single-photon sources [8]. Additionally, their reported QD densities are significantly lower than those observed in SK growth, with a surface density of 2.8×10^8 cm^{-2}. This is approximately two orders of magnitude lower than the QD densities observed in MOVPE-grown SK QDs, where densities can reach values on the order of 10^{10} cm^{-2} [27].

Another approach is MBE-based growth of InAs/InP QDs, as demonstrated by Miyazawa et al. [8], which also demonstrates yet another method of succesful fabrication for highly pure single-photon sources with exceptionally low multi-photon emission probabilities, with their study acheiving a low second-order correlation function, reporting a $g^{(2)}(0)$ value of $(4.4 \pm 0.2) \times 10^{-4}$. Additionally, the MBE-grown QDs emit single photons also at 1.5 μm (0.83 eV), making MBE another well-suited method for quantum communication over distances beyond 200 km.

From the litterature, it is evident that substrate temperature is a major factor in QD growth and morphology, irrespective of which of the two strain-driven epitaxy methods are used. For SK-grown QDs, the density of self-assembled islands has been observed to decrease with increasing temperature, ranging from approximately 10^{12} cm^{-2} at 400°C to 0.5×10^{10} cm^{-2} at 500°C [27]. These increased temperature essentially increases the diffusion length of adatoms, which reduces the nucleation density, and instead favouring the formation of larger QDs, making size-control possible by tuning the substrate temperature. However, excessive temperatures can lead to the

desorption of adatoms, thereby degrading the QD size uniformity.

A comparison of the photoluminescence properties across different growth techniques further highlights the trade-offs between methods. For SK-grown InAs/InP QDs, PL peaks range from 1.03 eV to 1.10 eV, depending on QD size distribution [27]. In contrast, the DE-grown QDs in [57] exhibit a PL peak centred at 0.85 eV (1500 nm), which is in accordance with general theory, as a common property of SK-grown QDs is the characteristic red-shifted emission spectra. However, it is possible to subvert this, as has been done in the MBE-grown QDs in [8], which demonstrate emission in the same spectral range but with a substantially lower fine-structure splitting of 100 μeV, albeit higher than DE-grown QDs. Additionally, the single-photon purity, as determined by $g^{(2)}(0)$ measurements, reveals a stark contrast between the techniques: DE-grown QDs achieve a single-photon purity of approximately 92.5%, whereas MBE-grown QDs demonstrate extremely high purity of 99.96% [8].

3.1.2 Strain effects in deterministic site-controlled quantum dot growth

The stochastic nature of self-assembled SK growth often leads to random spatial distributions of QDs, posing challenges for applications requiring precise positioning and uniformity. To address these limitations, variations of deterministic site-controlled growth techniques have been developed, enabling the fabrication of QDs at predefined locations with controlled properties.

Among these approaches, the buried stressor method and nanohole template technique have emerged as leading strategies due to their ability to influence strain fields and achieve spatially controlled QD formation [15]. The buried stressor method, for example, utilizes a buried AlAs layer that undergoes partial oxidation to form Al_2O_3, generating localized strain fields that direct QD nucleation [15].
The resulting strain modulation facilitates the deterministic alignment of QDs with oxide apertures, minimizing inhomogeneous broadening while maintaining optical purity.
Experimental demonstrations have achieved highly uniform QD positioning in 28 x 28 mesa arrays, with inhomogeneous broadening reduced to 15.8 meV, a notable improvement over the 18.4 meV broadening observed in non-positioned QDs [15], showing the importance of deterministic growth. Additionally, linewidth distribution statistics from a 10 x 10 subarray indicate that site-controlled QDs exhibit an average linewidth of 120 μeV, compared to 160 μeV for non-positioned QDs.

An alternative approach to deterministic site-controlled QD growth is the incorporation of quantum dots within position-controlled InP nanowires, grown via a bottom-up selective-area vapour-liquid-solid epitaxy [58]. This method has demonstrated a fabrication yield of nearly 100%, overcoming one of the persistent limitations in site-controlled QD growth, where unintended nucleation events often degrade the ratio of succesful growths on predefined sites. The InAsP QDs are embedded within tapered InP photonic nanowires, enabling efficient single-photon extraction with collection efficiencies reaching up to 83% and near-transform-limited linewidths of 880 MHz [58]. A key advantage of this approach is the absence of the two-dimensional wetting

layer commonly present in self-assembled QDs, which reduces spectral pollution from nearby QDs and eliminates hybridization effects that broaden emission linewidths [58].
Optical characterization of the 10 x 10 array of nanowires confirmed that every single QD exhibited bright emission, with an average exciton peak energy centered at 1264 meV and a standard deviation of 6 meV, demonstrating exceptional uniformity compared to conventional SK growth [58]. The single-photon purity measurements revealed multiphoton emission probabilities as low as 0.6%, highlighting the robustness of this approach for quantum photonic applications [58]. While this technique provides near-unity yield, a remaining challenge is mitigating phonon-mediated pure dephasing, which broadens linewidths beyond the transform limit due to carrier-phonon interactions under above-band excitation [58].

3.1.3 Tuning Electronic and Optical Properties of Quantum Dots

Strain also plays a defining role in the optical properties of QDs, influencing both excitonic transitions and emission characteristics. As described in [10], authored by Holewa and others, the SK growth mode enables the formation of QDs with discrete energy levels, akin to atomic-like transitions, as described in the first section of the thesis. This quantum confinement effect is pronounced in InAs QDs on InP wetting layers, which emit in the telecom bands at 1460-1625 nm. In the study, it was investigated if such QDs could serve as high-purity single-photon sources: The primary measure of quality for single-photon sources is the second-order correlation function $g^{(2)}(0)$, which quantifies the probability of detecting more than a single photon at a time. For an ideal single-photon source, the value of $g^{(2)}(0)$ should be zero, indicating that only single photon events occur.
Holewa et al. demonstrated that InAs QDs, when grown under well-controlled strain conditions, exhibit highly pure single-photon emission, characterized by a second-order correlation function $g^{(2)}(0) < 0.02$, confirming their suitability as indistinguishable photon sources. This result will be compared to alternative growth methods in the comming section.

4 Experimental Techniques

In the following chapter we will present the techniques and equipment used in the fabrication process of III-V InP/InGaAs/InP-InAs quantum dots. We will chronologically present the steps taken to fabricate the samples, as well as the principles behind the techniques used, and the equipment used to perform them.
Many of these techniques are standard in semiconductor fabrication and well-documented in textbooks [29]. Additional resources, including equipment listings and pre-developed process recipes, are available on the DTU NanoLab platform (DTU LabAdviser [59]). However, certain process steps, particularly those related to etching and MOVPE growth, were specifically developed by the project team. The complete process-flow can be found in Appendix 7.3.

4.1 An overview of Applied Techniques and Equipment

4.1.1 Epitaxial Thin Film Growth

All epitaxial growth processes were carried out using DTU NanoLab's metal-organic vapour phase epitaxy (MOVPE) reactor. This reactor is a EMCORE horizontal-flow MOVPE type, operated at reduced pressure. Trimethylindium (TMIn) and trimethylgallium (TMGa) were used as group-III precursors for InGaAs and InAs growth, while arsine (AsH_3) and phosphine (PH_3) provided the group-V elements for As- and P-containing layers, respectively

4.1.2 E-beam Lithography

Multiple wafers was produced for the project, varying in composition and material combinations, however, the equipment used to fabricate them was consistent across all samples.
The resist was applied using the "Gamma E-beam and UV" system, a Gamma 4M cluster from SÜSS MicroTec. This system has dedicated modules for spin-coating, HMDS vapour priming, and baking, providing a highly reproducible and controlled environment for resist application. The electron-beam resist used was CSAR (AR-P 6200[60]), a positive-type, high-resolution and high-contrast resist, which makes it excellent for creation of holes on the nanoscale.

The patterning process was carried out using a JEOL JBX-9500FS electron beam lithography system. The system operates at an acceleration voltage of 100 kV and is equipped with a thermal field emission gun, providing high beam stability and resolution. The system uses a spot beam with variable shaping and a high-speed deflection system. The beam current, step size, and exposure dose can all be modfied to achieve the required resolution while minimising proximity effects. Job files were prepared using JEOL's standard workflow, including dose modulation for process optimisation.

Following exposure, the resist was developed using DTU NanoLab's E-beam developer 02, which is a automatically operated, single-substrate puddle development process, with Zed N50 developer. The developer has a number of set recipes for different resists and time selections, ranging from 15 to 600 seconds. Each recipe follows a standardised sequence: developer dispense, static puddle development, periodic agitation, spin-off, IPA rinse, and nitrogen drying. The development was performed at room temperature, with agitation applied as a 1-second rotational movement at 30 rpm every 15 seconds.

Resist removal was performed using a combination of wet and dry methods. Two techniques were used for the wet resist removal. Following wet removal, residual resist and organic contaminants were eliminated using a PVA TePla Resist Ashing System GIGAbatch 380M. This plasma ashing step employed an oxygen plasma process to fully remove any remaining polymer residues, leaving a clean surface for subsequent processing.

4.1.3 Wet-Etching of Epitaxial Layers

Etching was performed exclusively using wet etching techniques, all carried out in a specialised fume hood. Two different fabrication techniques were explored in this project; one where an InGaAs layer was grown epitaxially on top of the InP substrate, and another where the growth also involved an InP toplayer on the InGaAs prior to etching. The indium phosphide was etched using a solution of hydrochloric acid (HCl) and phosphoric (H_3PO_4) acid, indium-gallium-arsenide layer etched in a solution of hydrogen peroxide (H_2O_2) and sulfuric acid (H_2SO_4).

4.1.4 Characterisation

The most utilised characterisation technique in this project was optical microscopy, which was performed using a Nikon Eclipse L200 microscope. This microscope has a 200 mm x 200 mm stage, and 2.5x to 100x objective lenses.
However, some of the features cannot not be optically resolved, and thus required the use of another technique: Scanning Electron Microscopy (SEM), which was performed using a Zeiss Supra 40 VP, which has an effective resolution-limit on the low-nm scale.
Lastly, surface roughness and step height measurements were obtained using the Dektak XTA stylus profiler from Bruker, and an Atomic Force Microscopy (AFM), Dimension Icon-PT, from Bruker to acquire high-resolution surface topography used to determine etch rates and quantum dot positioning.

In the following sections, we will present the steps taken to fabricate the samples, which require the presentation of models showcasing the nature of the samples at the given stage. The color scheme below will be used to represent the different materials in the models:



Figure 8: Color key for the process models.

4.2 Process Steps

4.2.1 Initial growth of Epitaxial Layers

Unlike MBE, which is governed by physical vapor deposition under ultra-high vacuum conditions, MOVPE is a type of chemical vapor deposition, where precursor gases decompose at the heated substrate, forming epitaxial layers through surface reactions, with a rate of deposition in the range of 0.1 to 1 monolayers per second (ML/s) [29].
One of the defining characteristics of MOVPE is its inherently non-equilibrium nature, which is a little different from the simpler equilibrium system that we discussed earlier in Section 2.2.
Fundemently, the same actions are taking place, and the same principles apply, however, in our thermal equilibrium model, we assumed that adatoms had sufficient time to diffuse across the substrate surface, settle into thermodynamically favorable sites, and reach a near-global free energy minimum before incorporation into the lattice. But in MOVPE, growth is limited by kinetic constraints such as mass transport, surface reaction rates, and precursor depletion, meaning that adatom diffusion is often interrupted before reaching an equilibrium state, which makes MOVPE deviate from the ideal layer-by-layer growth. Instead, metastable structures, step-bunching, and alloy segregation can emerge. This deviation from equilibrium is particularly interesting in the Stranski-Krastanov growth mode, where quantum dot self-assembly is driven by strain relaxation, but is simultaneously influenced by growth rate, supersaturation, and adatom mobility. Unlike equilibrium-based models where the critical thickness for island formation is solely dictated by elastic energy minimization, in MOVPE the nucleation and evolution of quantum dots are strongly dependent on the V/III precursor ratio, -amount, and growth temperature[27], making growth parameter adjustment and optimisation important, as it can be used to compensate for the limited kinetics.

One way to counteract these kinetic limitations is by increasing adatom mobility, which can be achieved through temperature control.
This is particularly critical in Frank-van der Merwe growth, the mode responsible for forming the underlying epitaxial layers. Since this process relies on layer-by-layer deposition, adatoms must diffuse across the surface to reach stable lattice sites rather than forming clusters. Higher temperatures can support this diffusion, which is why growth typically exceeds 600°C. Without sufficient thermal energy, adatoms risk becoming trapped in metastable configurations, leading to surface roughness and departures from ideal layer-by-layer growth.

In the fabrication first approach, an InGaAs layer grown on an InP substrate, followed by lithography and etching steps, after which a subsequent InP layer with InAs quantum dots was grown on top. In the second approach, the InP top-layer was grown on InGaAs from the onset, and lithography and etching were performed on both layers.
Despite these structural variations, the growth process itself remained nearly identical. The substrates used were 2-inch (001)-oriented InP wafers, pre-treated by the manufacturer to eliminate native oxides. The epitaxial deposition began with the growth of a 16 nm $In_{0.53}Ga_{0.47}As$ layer, initiated by ramping the temperature to 660°C over 30 seconds, followed by a stabilization phase

where the proportional-integral-derivative (PID) controller reduced the temperature to 610°C. Throughout this part, phosphine (PH_3) was introduced at a constant flow rate of 200 sccm to stabilize the surface and prevent desorption.

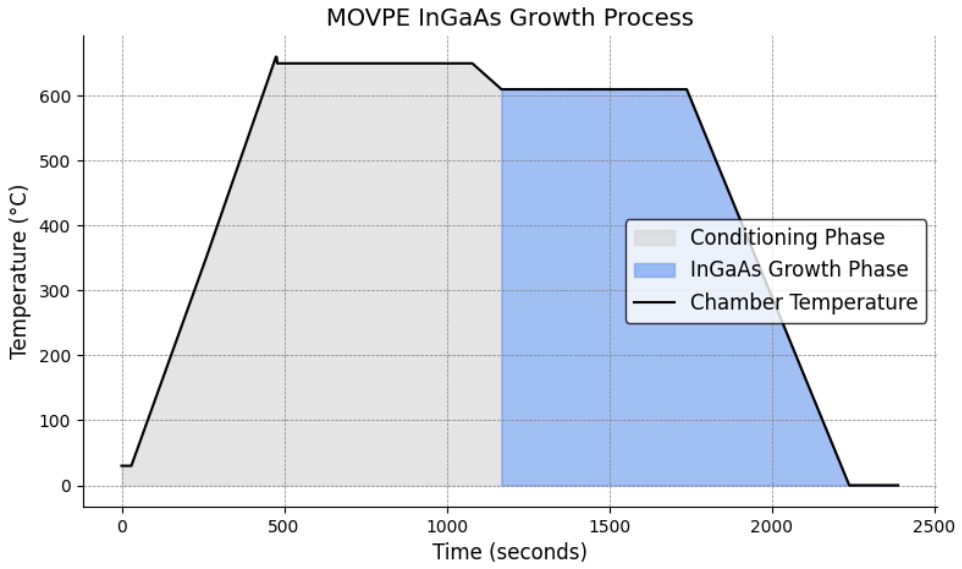

Figure 9: Diagram showing the temperature profile during InGaAs growth on InP.

Approximately 18 minutes into the process, indium was introduced into the reactor in the form of trimethylindium (TMIn) at a flow rate of 355 sccm. Following a 180-second delay, gallium and arsenic precursors were introduced at flow rates of 13.6 sccm and 175 sccm, respectively. These conditions were maintained for the remainder of the deposition, with the temperature stabilizing at 610°C upon the introduction of TMIn and arsenic dimers (As_2). The growth was concluded by a 650-second controlled temperature ramp-down to room temperature to prevent thermal stress-induced defects.
The growth rate for this process was determined to be 0.3 nm/s, corresponding to 0.5 ML/s of $In_{0.53}Ga_{0.47}As$. The total active growth duration was approximately 480 seconds, resulting in a final InGaAs layer thickness of 16 nm, selected to not exceed the critical thickness for strain relaxation. The complete deposition process lasted approximately 40 minutes, and yielded the desired 16 nm InGaAs layer on InP.

This critical thickness was calculated using the Matthews-Blakeslee model, as per Equation 42[31], using the lattice mismatch calculation from Equation 40. We used the value of 5.869×10^{-10} m for the lattice constant of InP [43], 6.058×10^{-10} m for InAs [44], and 5.869×10^{-10} m for GaAs [61].
The lattice constant of InGaAs is composition-dependent and follows Vegard's law 50, which was then calculated to be 5.869×10^{-10} m for the $In_{0.53}Ga_{0.47}As$ layer.
It should be noted that the Matthews-Blakeslee model is a simplified model, and has been ob-

served as being inaccurate, with up to 6% deviation for this specfic III-V system[62].

We then approximated the Burgers vector to be

$$b = \frac{a_{\text{InP}}}{\sqrt{2}} \approx 4.15 \times 10^{-10}\text{m} \tag{52}$$

and the Poisson ratio to be $\nu = 0.36$ [43].

The iterative solution was set to a convergence level of 10^{-3}, with an intial guess of 10 nm. The code can be found in the appendix 7.4.
A similar growth process was used for the InP layer, performed in a single run in the case of the sample with the structure InP/InGaAs/InP, with the only difference being an intermediate section in the run between the final ramp down and the growth of the InGaAs layer, where the temperature ran at 610°C, with continous flow of exclusively TMIn and PH_3.

Step	**Equipment**	**Procedure**
MOCVD growth	MOVPE	Place a 2" wafer in the correct stage slot, load the sample into the reactor and perform the growth. Recipe: "InGaAs Tstrain 16 nm", time: 39:48 (mm:ss). Target thickness: 16 nm resulting [Ga;In] Fraction: [0.47; 0.53] or Recipe: "InGaAs InP Tstrain 16 10 nm". Target thickness: 16 nm resulting [Ga;In] Fraction: [0.47; 0.53], and 10 nm 100% InP

Table 1: Processflow for epitaxial growth procedure.

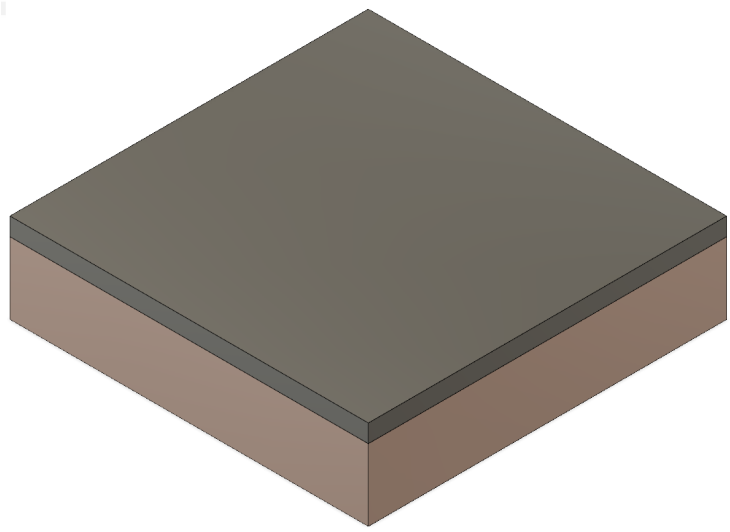

Figure 10: Model displaying the InGaAs epitaxial layer on the InP substrate.

4.2.2 Electron Beam Lithography

EBL is similar to traditional photolithography, but instead of using light, it employs a focused beam of electrons to expose a resist. Unlike photolithography, which relies on optical masks and is diffraction-limited, EBL uses direct writing at single-digit nanoscale resolution, achieving feature sizes well below the diffraction limit of light-based techniques. This makes EBL particularly suited for high-precision nanofabrication where flexibility and resolution are critical.
The process involves scanning a tightly focused electron beam across a resist-coated substrate, selectively exposing predefined regions. The exposure dose is defined by the user and determines the amount of energy delivered to the resist. The system calculates the beam dwell time required for each pixel to achieve the requested dose, adjusting it dynamically based on the defined area dose. Exposure is performed in a serial manner, where each feature is fractured into smaller writing fields, and within each field, the pattern is decomposed into discrete beam shots, placed according to an exposure grid.

To achieve uniform exposure, the shot pitch, the spacing between consecutive beam shots, must be optimised in with beam current and dose. A finer pitch results in a higher number of beam shots, increasing exposure time but improving resolution and feature uniformity. For example, at a 2 nA beam current with a dose of 250 μC/cm^2, a 4 nm shot pitch would yield a dwell time of 20 ns, while reducing the shot pitch to 2 nm would lead to a dwell time of 80 ns.
Another critical aspect of EBL is pattern alignment across multiple writing fields. The JEOL system employs an automated write-field alignment procedure that ensures sub-15 nm stitching accuracy. Misalignment between neighbouring fields can lead to stitching errors, causing discontinuities in features that span multiple fields. The JEOL system utilises an internal alignment sequence to correct for these effects, improving pattern fidelity and ensuring smooth feature transitions.

The lithographic procedure followed a standardised DTU NanoLab workflow.
Prior to exposure, the samples underwent a heat treatment step to eliminate any condensation and surface contamination that could interfere with resist adhesion. Even minor amounts of surface moisture can impact resist uniformity, leading to defects such as dewetting or inconsistent exposure outcomes, and heating the wafer drives off adsorbed water molecules and organic contaminants, ensuring a clean and dry surface before resist application.
Following heat treatment, the wafers were coated with Surpass 3000, which is a priming agent designed to enhance resist adhesion. Traditional adhesion promoters such as hexamethyldisilazane (HMDS) form a hydrophobic silane layer to improve adhesion, but Surpass 3000 instead uses a heteroatom resonance bonding process, where functional groups within the Surpass 3000 molecule selectively bind to electrostatic contaminants on the substrate, neutralizing their charge and allowing them to be rinsed away, while also forming a thin film of functional groups that promote adhesion [63]. This Surpass application is then followed by a 30 second Deionised water rinse to rinse away contaminants, and finalise the adhesion promotion process.

Surpass 3000 suffers from a short shelf life, and spin coating of the Electron Beam Resist, must therefore be performed shortly, on the order of minutes, after application. For this purpose the wafers were immediately transferred to the spin coater, where they were coated with CSAR resist, a common positive-tone EBL resist. The resist thickness was chosen to be 180 nm, as this is a standard recipe, and does not need further adjustments. Alternatively, 360 nm resist thickness could have been selected, but this would have required longer exposure times on the expensive EBL system.
The standard spin coating recipe includes the dispensing of the resist, and spinning at 5400 rpm for 60 seconds, followed by a bake at 180°C for 60 seconds on a Suss MicroTec HP8 Hot Plate.

Step	**Equipment**	**Procedure**
Pre-bake	Hotplate	Heat the wafer at 100°C for 5 minutes.
Adhesion promoter	III-V Fumehood	Surpass 3000 dip application for 30 seconds follow by 60 seconds dip in DIW.
Coating wafers	Spin Coater: Gamma E-beam & UV	Resist: CSAR (AR-P 6200, AllResist) Spin: 60 sec @ 5400 rpm (for appr. 180 nm) Softbake: 1 min @ 180°C Recipe: (2318) DCH 50mm CSAR 180 nm

Table 2: Spin coating procedure for CSAR AR-P 6200 on III-V substrate.

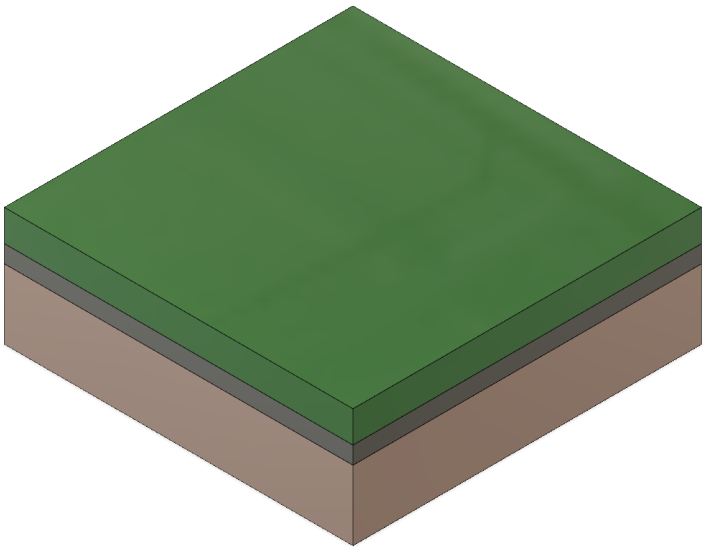

Figure 11: Resist Spin coated on top of InP/InGaAs structure.

After the resist coating, the samples were loaded into the EBL system, where the exposure was performed. The pattern was designed using `KLayout` and `GDSpy`.
The entire design was fitted into a 1 mm x 1 mm square, which is the maximum writing field size of the JEOL system. It features 24 lower-density fields; with each field being approximately 120 μm x 120 μm, and 3 smaller high-density fields of 30 μm x 30 μm. These high density fields were reduced in size to compress the GDSII file, such that the JEOL software could compile the file in reasonable time.
Three different field morphologies were selected; circular, square and diamond (45° rotated square), with each morphology used in 8 fields. These 8 fields were further divided, testing 2 different hole sizes; 40 nm, and 80 nm radii for the circles, sidelengths for the squares, and diagonals for the diamonds. Finally, for each of these sizes 4 different pitches were used: 400 nm, 1.2 μm, 2 μm, and 4 μm.
The patterns can be seen below in Figure 12.

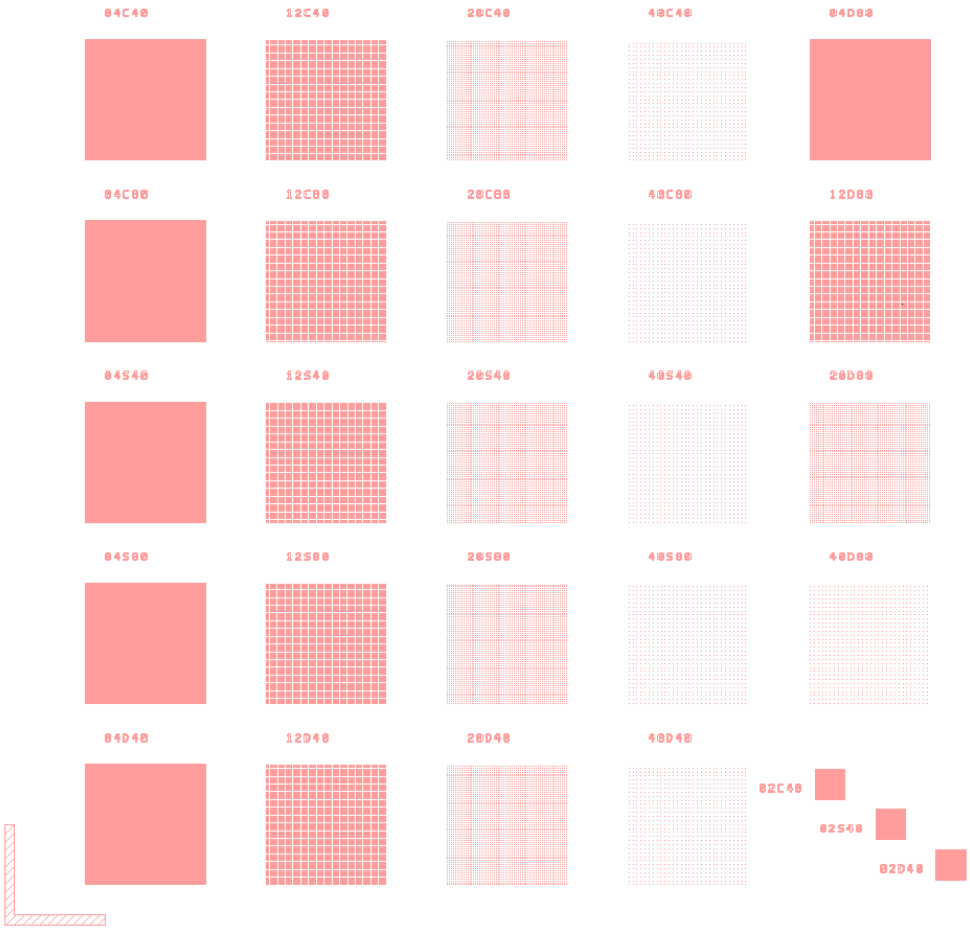

Figure 12: Overview of GDS pattern design. The first 4 fields in row 1-2 are designated for the circular holes. The first 4 fields in row 3-4 are squares. Diamonds were allocated in the right most column, and bottom row. The `GDSpy` code can be found in Appendix 7.2.

The three smaller fields use the same shapes as the larger fields, one of each morphology, but only includes the 40 nm dimensionality parameter, and a pitch of 200 nm.

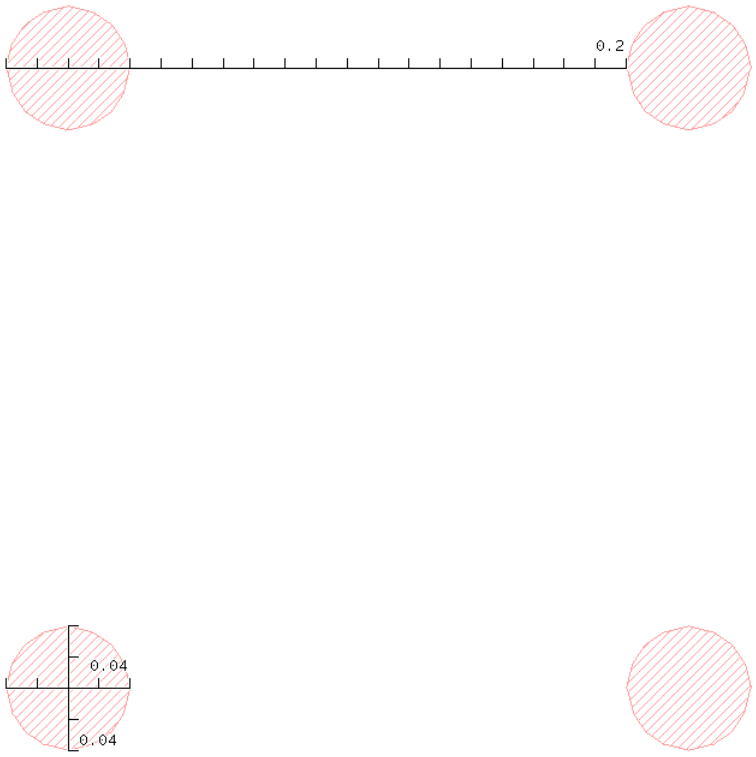

Figure 13: Close-up of the high-density pattern. Measuring scale is resolved in microns.

Additionally, a Scalebar and top-level numerical label was placed in each chip pattern, and each field within a chip was labelled with a unique identifier based on pitch, morphology, and size, in that order.

Across the 2 inch wafer, 24 chips were placed with a slight offset to the center lines of the wafer, as seen in Figure 41 in the appendix. However, during this project, alternative wafer layouts were considered, and an optimised wafer layout procedure was developed based on 2 common algorithms; simulated annealing and the greedy algorithm, which are both explained and discussed in Appendix 7.1.

The process steps can be seen in Table 3.

Step	Equipment	Procedure
E-beam exposure	E-beam writer: JEOL 9500	For AR-P 6200 (180 nm) at an acceleration voltage of 100 kV.
Development	E-beam developer 02	Automatically: Develops with ZED N50, 60 sec Rinses in IPA, 60 sec Blow dry with N_2

Table 3: E-beam exposure and development process.

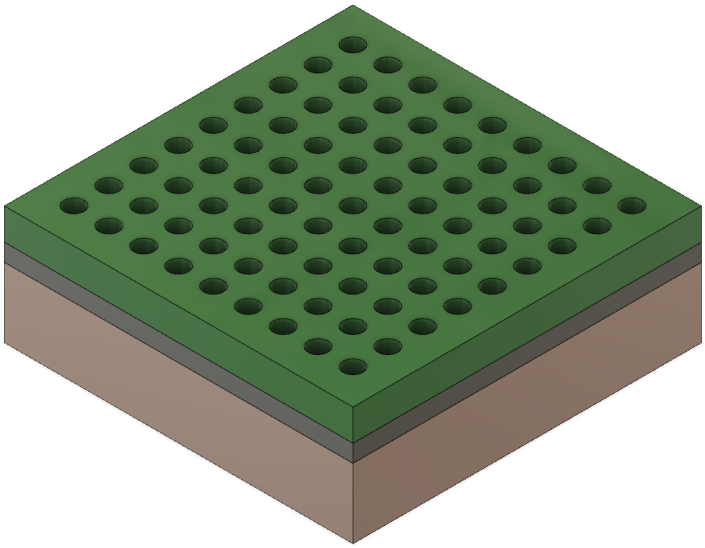

Figure 14: Model showing a subarea of a wafer, illustrating the patterning of holes.

4.2.3 Wet Etching of sample

The InGaAs layer was etched using solutions of hydrogen peroxide (H_2O_2) and sulfuric acid (H_2SO_4) in a 1:1 ratio, diluted in a 1:1:80 to 1:1:160 ratio with deionised water. This solution has been used previously by the project team to perform selective etching of InGaAs, and has been shown to be effective in removing the InGaAs layer without affecting the underlying InP layer. This can be seen in table 4, which was adapted from a table by the chemistry department of the University of Maryland [64].

Etchant	GaAs	InP	InGaAs
HCl : H_3PO_4	S	E	S
H_3PO_4 : H_2O_2 : H_2O	E	S	E
H_2SO_4 : H_2O_2 : H_2O	E	S	E
HCl : H_2O_2 : H_2O	E	E	
HCl : H_2O	S	E	S

Table 4: Material selectivity of different etchants. S denotes that the material is not etched by the acid combination, E denotes etching, and CD denotes chemical decomposition-dependent etch. The table is based on data from [64] [65].

From this table it is evident that this solution is specific to InGaAs, and will not etch the InP layer, making the InP an ideal etch-stop layer. The etch rate of the InGaAs layer is dependent on the concentration of the etchant, and prior etch-tests have shown that a 1:1:80 ratio of H_2O_2 : H_2SO_4 : H_2O will etch the InGaAs layer at a rate of approximately 1 nm/s.
To perform the etch, the sample was submerged in the etchant solution for approximately 16 seconds, and then dipped in DIW for 30 seconds to remove any residual etchant. The sample was then dried using nitrogen gas.

The InP layer was etched using a solution of hydrochloric acid (HCl) and phosphoric acid (H_3PO_4) in a 1:20 ratio, with an etch rate test, which can be seen in figure 15, showing that the etch rate of the InP layer is approximately 3 nm/s. The etch rate test were performed on 3 dedicated InP test samples for 8, 10 and 15 seconds, with slight margins of $\pm$ 1 seconds, as the solution is more viscous than other acids, and therefore does not flow as well on or off the sample. The height variations after the etch were measured using a DEKTAK profilometer.
This solution was chosen as it has been shown to be effective in etching InP, however, it was used in a 1:3 HCl:H_3PO_4 ratio in previous work [66]. The advantage of using this acid combination, is that it is has proven to be ineffective in etching InGaAs [67]. After performing the etch, the sample was submerged in DIW for 30 seconds, and then dried using nitrogen gas.
Based on the calculated etch rate for the 10 nm InP layer, the etch time was estimated to be approximately 3 seconds, however, due to the higher viscosity of this solution compared to other

acids, the etch time was increased to 5-7 seconds to ensure a complete removal of the InP layer.

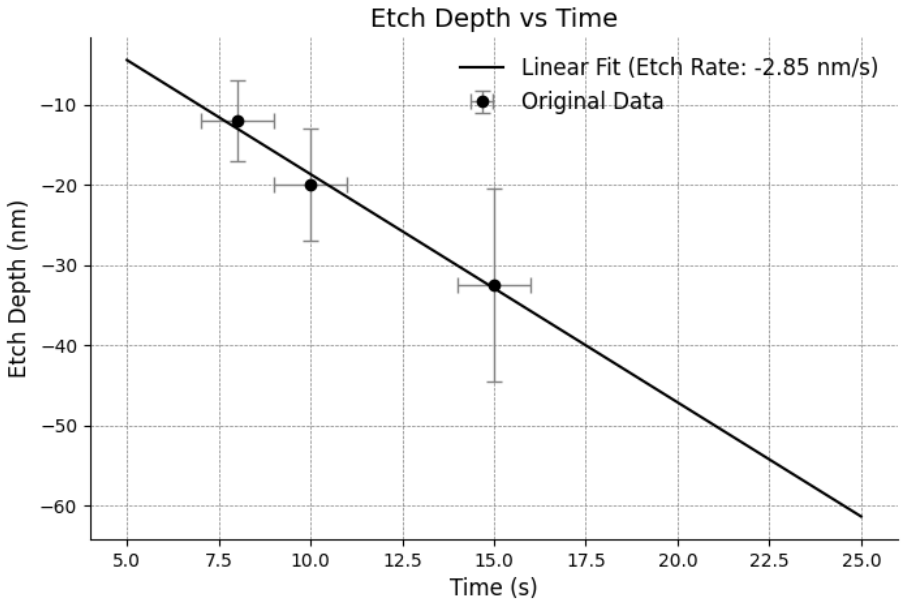

Figure 15: The etch rate of hydrochloric acid (HCl) and phosphoric acid (H_3PO_4), visualised, with a trendline showing the approximated etch rate of the solution.

Step	**Equipment**	**Procedure**
Selective InP Wet Etch	III-V acid/bases fumehood	1:20 HCl(37%):H_3PO_4(85%) dip for 3 seconds 30 second dip in DIW Blow dry with nitrogen.
Selective InGaAs Wet Etch	III-V acid/bases fumehood	1:1:80-1:1:160 H_2O_2(10%):H_2SO_4(30%):H_2O dip for 16 seconds 30 second dip in DIW Blow dry with nitrogen.

Table 5: Processflow for the III-V wet chemistry etching for pattern transfer. For the sample without the InP toplayer, the first step was naturally not performed. If the two etches were performed on the same sample in quick succession, blow drying with nitrogen after the first etch was not performed.

4.2.4 Resist Stripping

After etching the sample, the photoresist must be removed to expose the underlying material. For this project 2 different approaches were used: a simple dip in solvent for an extended period of time, and a more elaborate process heated solvent dips and an ultra-sonic bath [68]. After having performed wet resist removal, the samples were subject to a final dry clean using a plasma asher. The wet chemistry process involves submerging the sample in Remover 1165 [69], a solvent designed to dissolve photoresist without damaging the underlying material. Remover 1165 is an organic solvent that breaks down the polymer chains of the resist through solvation, allowing it to be removed off the substrate.

It should be noted that the original recipe for the advanced resist removal process included several steps, where the Remover 1165 was heated beyond its flash point of 88°C [69], which is prohibted in the NanoLab clean room due to safety regulations.
The process was therefore slightly modified, such that the temperature never exceeded 80°C.
Furthermore, the original process also calls for sonication in propan-2-ol at room temperature, however, the fumehood is only equipped with a single ultra-sonic cleaner, and as the water bath in the ultra-sonic cleaner, prior to the propan-2-ol bath, has been heated to 80°C, far exceeding the boiling point of propan-2-ol, the propan-2-ol ultra-sonic treatment was omitted, instead replaced by simply mechanically agitating the sample in room temperature propan-2-ol every 30 seconds for 10 minutes.

Following either of the wet resist removal processes, the sample is rinsed with isopropanol (IPA), as IPA disolves organic contaminants while being miscible with water. A final rinse with deionized water (DIW) ensures the complete removal of any remaining impurities.

The plasma asher process, a descumming process, is necessary to remove any residual resist that may remain after the solvent-based removal. This step is particularly important for ensuring clean surfaces for subsequent processing.
Plasma ashing relies on reactive oxygen species to break down and volatilize the remaining organic photoresist material. The oxygen plasma generates high-energy radicals that interact with the carbon of the resist, converting it into volatile byproducts such as CO_2 and H_2O, which are then evacuated from the chamber. This step is performed to make sure that the surface is completely clean and free of organic contamination.

The full process can be seen in Table 6.

Step	Equipment	Procedure
Simple strip	III-V Solvent Fumehood	Submerge etched sample into Remover 1165 for $>$ 1 hour. Rinse with 30-second IPA dip. Rinse with 30-second DIW dip.
Advanced strip	III-V Solvent Fumehood Hotplate VWR USC 1700D ultra-sonic	HP: 80°C 1165, 10 min. USC: 80°C, 1165, 10 min, 45 kHz. HP: 80°C 1165, 10 min. USC: 80°C, 1165, 10 min, 45 kHz. USC: 80°C, 1665, 3 min, max kHz. MA: 25°C, propan-2-ol, 10 min. Blow dry with Nitrogen gas. HP: 100°C, 1 min. Rinse, H_2O, 1 min. Blow dry with Nitrogen gas.
Descumming	Plasma Asher	300 sccm Oxygen, 400 Watt, 10 min.

Table 6: Table showing the two resist stripping process used in the project. The process ended with putting the samples directly on a hotplate at 100°C for 1 minute to drive off remaining solvent, before being rinsed in water, and blow-dried with nitrogen. HP: Hotplate, USC: Ultra-Sonic Cleaner, 1165: Remover 1165, MA: Mechanical Agitation.

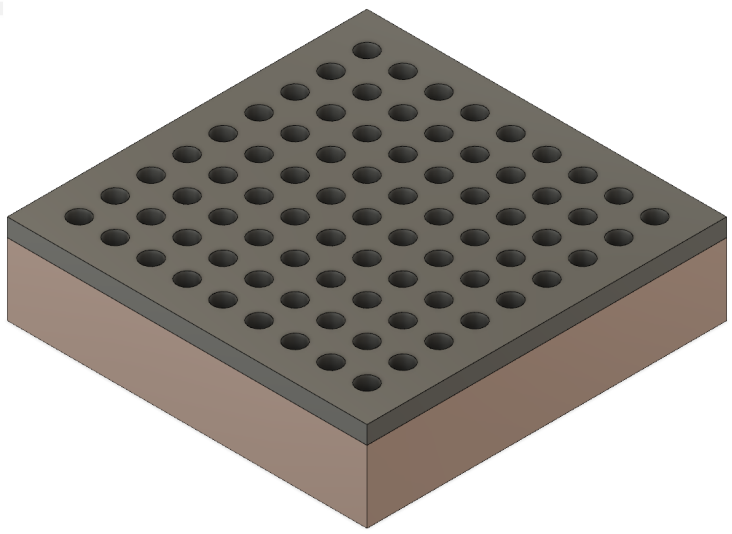

Figure 16: Model of the sample after the resist stripping process. The holes in the InGaAs layer are now completely exposed, and can readily be observed.

4.2.5 Quantum Dot Growth

After having completed the resist removal process, the samples were ready for the epitaxial growth of the quantum dots.
The process starts out by cleaning the samples in a (NH_4OH (25%): H_2O) ammonium hydroxide solution, in a 1:5 ratio for 60 seconds. This wet clean is weakly basic, and is commonly used to dissolve native oxides on III-V materials, since it easily froms hydroxides complexes with group III oxides [70][71]. The samples were then submerged in DIW, while in transport to the MOVPE reactor, to ensure that no re-oxidation occured by exposing them to ambient conditions.
Just before loading the samples into the reactor, they are moved from the DIW bath to a nitrogen bubble bath, to agitate the surface and remove any remaining particles. This process takes a couple of minutes and is done to ensure a clean surface before the epitaxial growth.

The epitaxial deposition process can be separated into 3 different steps: The conditioning of the chamber, the growth of the InP toplayer, and the growth of the InAs quantum dots.

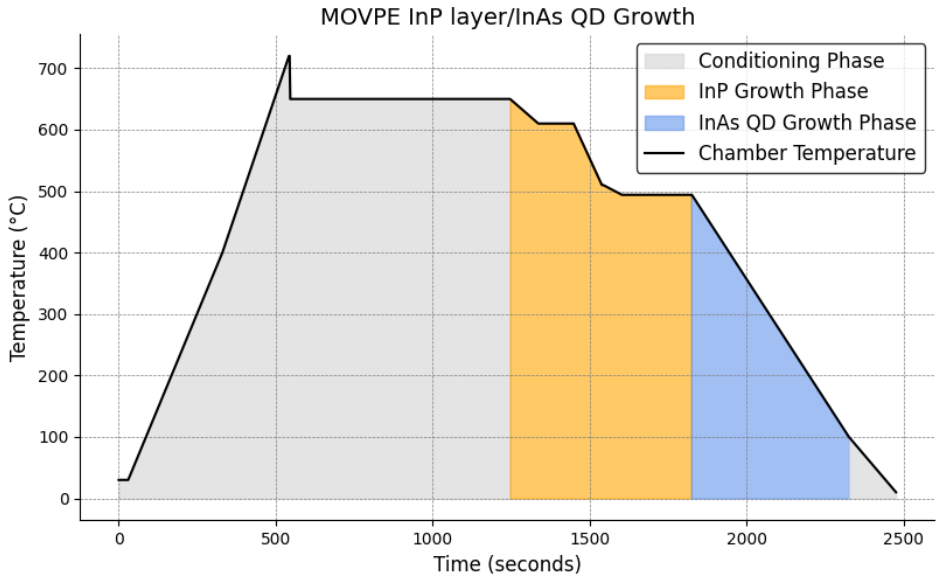

Figure 17: Visual representation of the temperature profile during InP toplayer / InAs QD growth on InGaAs. Different growth phases are distinguished by color.

As in the previous MOVPE growth, the reactor was first conditioned by overshooting the temperature, this time, to a target of 720°C, before the PID controller stabilized the temperature at 650°C, as seen in Figure 17. This process takes approximately 500 seconds to complete. During this phase phosphine is introduced at a flow rate of 200 sccm to provide a stable growth environment for the InP layer, as the surface is prone to desorption, unless a high chemical pressure of phosphorous is maintained. The flow of phosphine is maintained for the two first phases.
The temperature is then lowered to 510 degrees over 1.5 minutes (Figure 17), and indium is

introduced into the reactor in the form of trimethylindium (TMIn) at a flow rate of 200 sccm approximately 23 minutes into the process, and is maintained for 80 seconds. After the indium flow is terminated, the phosphine flow is maintained for another 7 minutes, to prevent InP decomposition.
After this phase, the growth of the InAs quantum dots is initiated by lowering the temperature further to 494°, see Figure 17, and introducing arsenic into the reactor, at a flow rate of 1.51 sccm, maintained for 500 seconds, with a short 2 second window of Indium at the beginning of the phase, at a flow rate of 30 sccm.
The growth of the InAs quantum dots is concluded by a controlled temperature ramp-down to room temperature over 650 seconds.

The final QD MOVPE growth was never attempted for the InP/InGaAs/InP samples, due to fabrication complications in the steps leading up the growth.

Step	**Equipment**	**Procedure**
Pretreatment	III-V acid/bases fumehood. Nitrogen bubble bath.	NH_2OH:H_2O (1:5) dip for N seconds. Rinse in DIW. Submerge in Nitrogen bubble bath until sample load.
MOCVD growth	MOVPE	Recipe: “InP 20nm QDs 2s VIII 20 In 30sccm” time: 41:14 (mm:ss). Target thickness: 20 nm InP

Table 7: Processflow for the final epitaxial growth procedure.

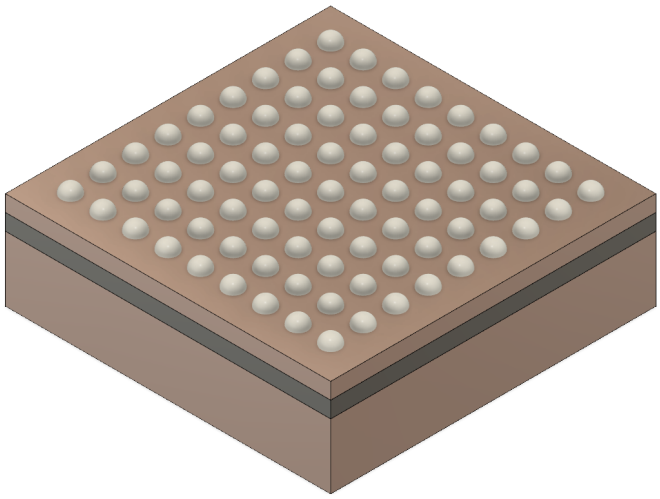

Figure 18: Visual representation of the final MOVPE growth, with InAs quantum dots above the InP filled holes. The model is not to scale.

5 Fabrication and Characterisation

In this section of the thesis, the practical work of the project is presented.
The chapter is divided into three parts, one for each of three distinct sample-types fabricated:

1. The first section details the fabrication of InP samples featuring an initial epitaxial growth of InGaAs.

2. The second section examines InP samples incorporating an initial epitaxial growth of both InGaAs and InP.

3. The third section outlines legacy InP samples, which also featured an initial epitaxial growth of InGaAs.

The fabrication of the third sample type was necessitated by the failure of the two previous samples, a failure that occured at the same stage in the process.
A comprehensive discussion, and justification for the use, of the sample is provided in Section 5.3; however, it is worth emphasizing that, at this stage, it had only undergone the epitaxial growth of InGaAs, with the same recipe as outlined in Figure 9, followed by resist application, development, and exposure.

5.1 Fabrication for InGaAs Epitaxy on InP Substrate

5.1.1 Epitaxial Growth of InGaAs

The first sample type was fabricated by growing a layer of InGaAs on an InP substrate, as outlined in Section 4.2.1. The InP(011) wafer was first subjected to the standard cleaning procedure before being loaded into the MOVPE reactor.
After the growth process, the samples were inspected using optical microscopy, to observe if the growth was successful. In particular, the aim of the microscopy was to simply verify that no visible surface topology gradients or surface defects were present.

5.1.2 Pre-treatment and Spin Coating

After having verified the growth, the samples were pre-treated with Surpass-3000 adhesion promoter, visually inspected, and then transferred to automatic E-beam spin-coater, as outlined in 2. The entire process lasted approximately 20 minutes from start to finish. During this time, the samples were exposed to ambient conditions for no more than 10 minutes without any active processing, which is within the expected shelf life of applied Surpass-3000.

Inspection of the resist covered samples was performed using optical microscopy, to verify that the resist was evenly distributed, and showed no signs of defects, like streaks, non-uniform liquid expansion, or sub-areas with different thicknesses, or lack of coating. No such defects were observed, besides acceptable levels of particle contaminants, as seen below in Figure 19.

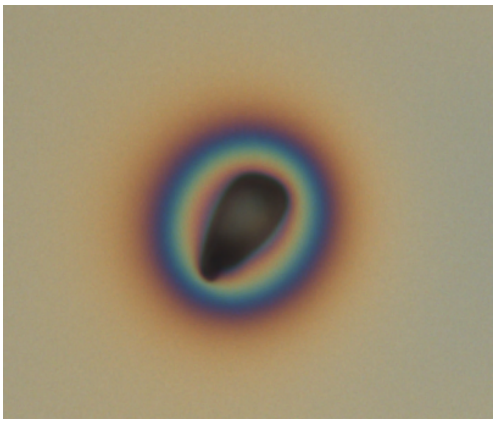

Figure 19: Optical microscopy image of a surface particle, approximately 5 μm in length, distorting the nearby resist topology.

5.1.3 Exposure and Development

The next process step was exposure of the resist on the JEOL-9500 EBL system.
No issues were encountered during the exposure process, nor the development process, yielding a successful pattern transfer. The samples were then inspected, first by means of optical microscopy, which can be seen in Figure 20. In this figure, one of the four center chips can be observed, with the labels and scalebar clearly visible, which suggests that pattern transfer was achieved, at least for larger structures. Furthermore, at a magnification of 10x, traces of the fields ”04C80” and ”04S80” can be faintly distinguished due to a slight contrast difference.



Figure 20: Optical microscopy image of the patterned sample. Labels are clearly visible and well-defined, and traces of structures are visible, with scalebar 100 μm in length.

To further verify the exposure, the samples were inspected using SEM, iterating through each field to ensure that the pattern was properly transferred to the resist and consistently replicated. For this process, 3 patterns were investigated, one on each side of the wafer, and one from the center. This was done to ensure that the settings related to height correction, beam alignment, and focus-calibration were correctly set.
Within each pattern, a subset of fields was inspected to assess pitch and diameter uniformity and to ensure that the holes were well-defined and accurately resolved, as seen in Figure 21.
In the SEM image, which was taken using an acceleration voltage of of 0.7 kV to avoid charging of the resist, the holes had a high level of fidelity, with well-defined edges and a uniform diameter. This result was consistently seen across the remaining fields, signifying that the exposure was uniformly achieved.

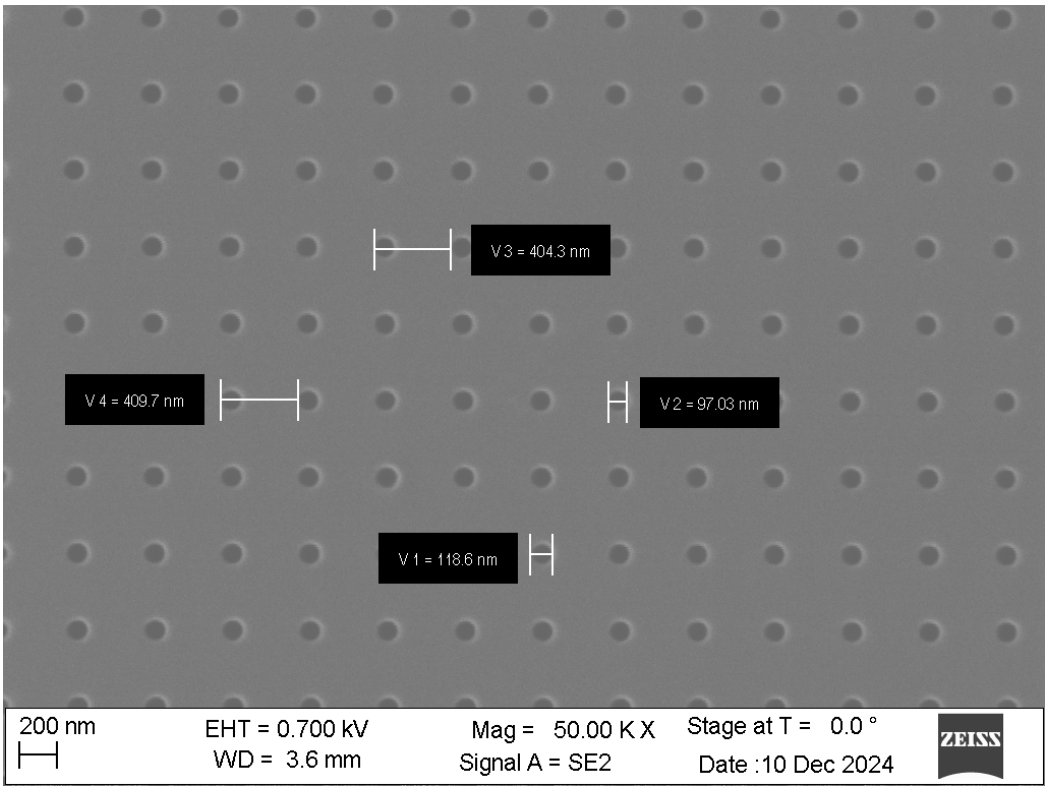

Figure 21: Scanning electron microscopy image of the resist pattern. The holes exhibit well-defined edges and uniform diameters, confirming successful exposure.

5.1.4 Etching of InGaAs Epitaxial Layer

After having verified the integrity of the resist, and the quality of the developed exposure pattern, the wafer was cleaved into chips, with the vast majority being defect-free, with no particle contaminants within the borders of the pattern.
The etching process was initially performed using the described 1:1:80 H_2SO_4:H_2O_2:H_2O solution for 16 seconds as per 5, followed by a DIW rinse and nitrogen blow-dry.
It was immidiately evident that the etch was had experienced complications after extracting the sample from the water, as no visible resist remained on the sample. Visually, the sample had a faint light-green tint to it prior to etching, indicative of a resist-layer, however, after having performed the etch-process, the sample instead had a pronounced metallic sheen to it.
The suspicions were confirmed when the sample was inspected using optical microscopy, shown in Figure 22. The image clearly reveals that the resist failed to adhere properly to the InGaAs layer during the etching process, resulting in significant flaking and peeling across the entire sample.
Large regions of delaminated resist are visible, exposing the underlying material and indicating poor adhesion. This widespread failure suggests that either surface preparation was insufficient or, perhaps that the etching concentration could have been too high.
The second hypothesis is based on the observation that parts of the pattern were etched into the

sample, as evidenced by the remnants of the ”04D80” label in the top right corner of Figure 22. This suggests that the etchant penetrated through the holes in the resist, isotropically etching the InGaAs layer beneath it. As the etching progressed, the resist may have been undercut and attacked from below, which could lead to delamination.
While possible, this hypothesis was not strongly supported, as other parts of the pattern were not etched into the sample at all. For instance, the label inbetween the partially etched ”04D80” (top-right) and the resist-covered ”20C40” (top-center), could not be discerned at any magnification.



Figure 22: Flaking and Peeling of the resist post-etching (1:1:80). 10x magnification.

While the hypothesis of isotropic etching was not strongly supported, it was still considered a possibility, and was therefore further investigated. We repeated the etching process across multiple chips using concentration ratios of 1:1:100, 120, 140, and 160 to investigate whether the resist was delaminating due to etching from underneath. If the resist was delaminating due to isotropic etching, the resist would be expected to remain intact at lower concentrations, as the etch rate would decrease, causing less undercutting.

The first attempt was performed using a 1:1:100 solution, with the same etch time as before, 16 seconds, followed by a DIW rinse and nitrogen blow-dry.
The sample was inspected using optical microscopy, and the result can be seen in Figure 23. Once again, the resist had partially delaminated from the InGaAs layer, with large regions of the sample showing no resist coverage. While flaking had occured, it was less severe than in the previous etch, with parts of the sample being intact.



Figure 23: Optical microscopy image of the resist post-etching. It appears that lower concentrations (1:1:100) improve resist integrity. 10x magnification.

The sample was then examined in detail using SEM to assess the extent of delamination and its impact on the pattern. As shown in Figure 24 on the top, the delamination is clearly evident.

Closer inspection revealed that even the resist regions that remained intact had deteriorated during the etching process, compromising the overall pattern integrity. The holes appeared blurred, with less-defined edges, and their diameters had increased significantly.

The effects were even more pronounced in the delaminated regions, where holes had been weakly etched into the InGaAs, had completely lost their definition, resulting in distorted features, as shown in Figure 24, bottom. In these areas, the holes had become increasingly shallow and superficial, which was evident from the contrast in the SEM image. Additionally, the spacing between them had decreased to the point where it was smaller than the hole diameters themselves.

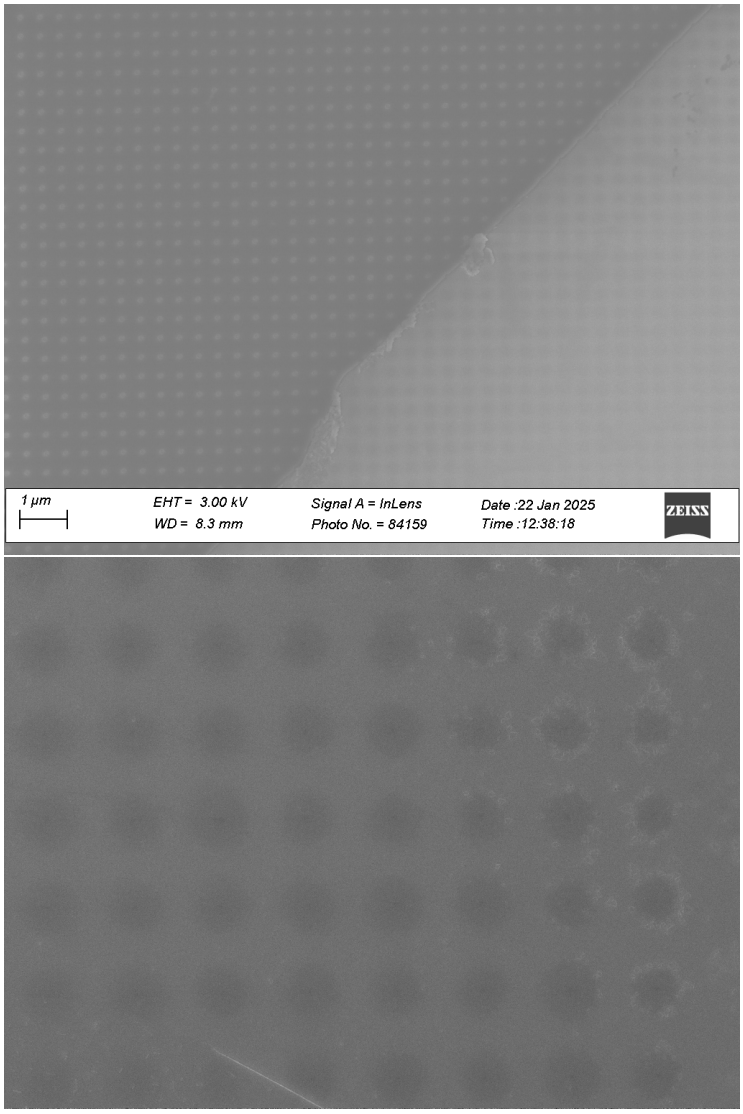

Figure 24: SEM images showing resist delamination and degradation post-etching. Top: Close-up of delaminated resist regions. Bottom: Distorted and shallow hole features in weakly etched areas of InGaAs.

However, since the resist had not completely delaminated, more attempts were conducted using the aforementioned concentrations, but no concrete or reproducible improvements were observed.
Finally, for completeness sake, the etching process was emulated, performing the same steps as before, but without the presence of any etchants. The sample was submerged in DIW for 16 seconds, rinsed in DIW for 30 seconds, and then blow-dried using nitrogen. Once again, delamination was observed across the sample, as seen in Figure 25

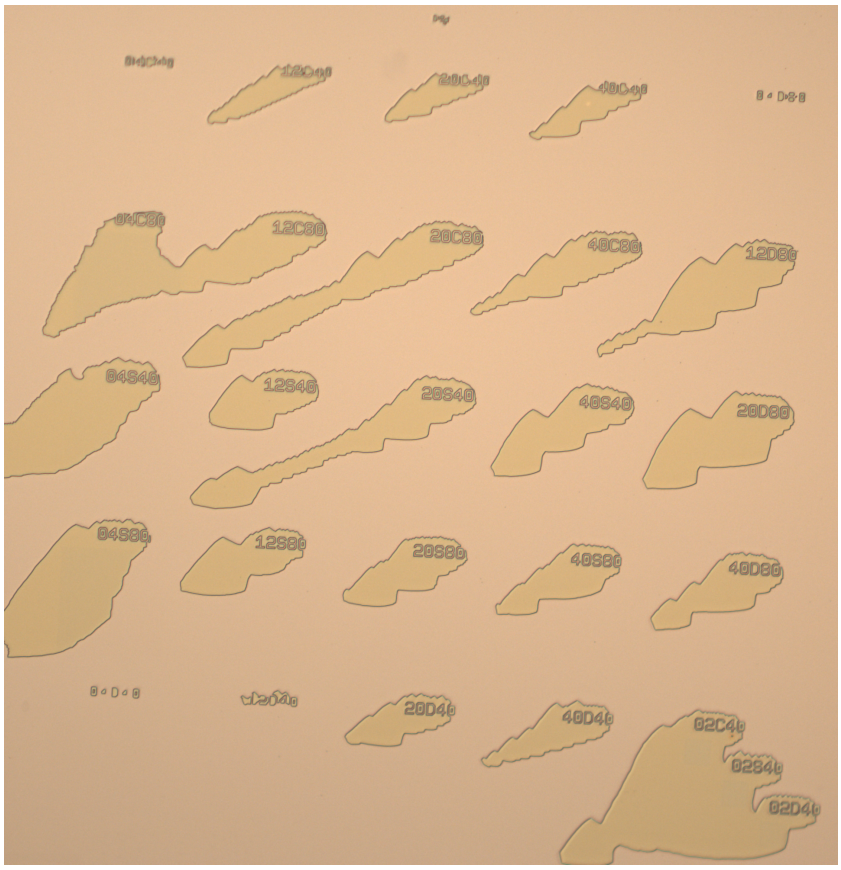

Figure 25: Optical microscopy image showing extensive resist delamination across the sample after etching process emulation without any chemical etchants. 10x magnification.

Despite multiple adjustments to the etching process, including variations in etchant concentration, duration and dip-technique, the resist continued to experience significant delamination and severe pattern degradation. While the initial exposure and development were successful, the failure of the resist to adhere throughout the etching process made it impossible to produce well-defined features with reproducible results.

Further attempts to mitigate this issue—including reducing the etchant concentration and even eliminating the etchant altogether—demonstrated that delamination occurred regardless of chemical etching, suggesting that some aspect of the resist adhesion process was at fault.

The literature clearly indicates that EBL resist peeling on III-V materials, particularly InGaAs, during wet etching is a well-documented issue. The most common solution to the adhesion-problem is the use of adhesion promoters [72] [73], such as HMDS or Surpass-3000, the latter of which was implemented in this project.
Other techniques, such as those outlined in [72], like multiple high-temperature ($> 120°$C) bakes prior to adhesion promoter application, and post-development, can help reduce resist dissolution during exposure to liquids and etching.

5.2 Fabrication of Optimised InP/InGaAs/InP Sample

Given the persistent adhesion issues encountered with the previous sample, further modifications to the process were unlikely to yield a reliable solution. To achieve a controlled and reproducible fabrication process, a new approach was required.
As a result, we opted to restart fabrication on a different wafer, reassessing each step of the process, including the epitaxial growth, substrate preparation, resist adhesion, and etching conditions.

5.2.1 Epitaxial Growth of InGaAs and InP

The new sample iteration also used an InP (011) substrate, similar to the previous sample, but with a key distinction in the epitaxial growth process. Previously, the InP layer was intended to be grown alongside InAs quantum dots, as outlined in Section 4.2.1 and Table 1, on top of the InGaAs layer. In this iteration, however, the 10 nm InP layer was grown immediately after the 16 nm InGaAs layer during the same growth sequence.

Compared to an InGaAs-terminated surface, an InP top-layer provides a more stable growth environment by mediating strain relaxation and suppressing supersaturation-driven fluctuations.. Without an InP cap, uncontrolled precursor supersaturation leads to non-uniform nucleation, where different regions of the wetting layer reach the critical thickness (1.5 ML) at varying rates, resulting in inconsistent QD densities and size distributions. By maintaining a chemically stable and structurally coherent surface, the InP cap moderates local strain energy, ensuring a more uniform transition from 2D to 3D growth [9].

One of the driving mechanisms behind the regulation is that the InP cap suppresses As/P intermixing, which a major source of wetting layer instability in InAs QD growth. During MOVPE, exposure to AsH3 induces self-limited As/P exchange, leading to composition variations in the wetting layer, ranging from $InAs_{0.18}P_{0.82}$ (2 ML thick) to $InAs_{0.75}P_{0.25}$ (4 ML thick). This variability affects the critical thickness for QD nucleation, making growth conditions unpredictable. With an InP cap in place, the surface remains phosphorus-terminated, minimising As/P intermixing and maintaining a well-defined wetting layer [9].

Furthermore, the phosphorus-rich environment of the InP cap prevents premature strain relaxation, which would otherwise lead to dislocations and degrade QD quality. When InP is present before InAs deposition, strain remains coherently distributed, allowing for controlled nucleation and uniform QD formation. Without the cap, strain relaxes unevenly, resulting in high clustering and broad size dispersion [9].

After the growth, the surface was inspected using OM, and no visible defects were observed.

5.2.2 Resist Application, Exposure and Development

The resist application process was carried out similarly to the previous sample, with a few key modifications. Prior to applying the adhesion promoter, the sample underwent a 180-second high-temperature bake, as suggested in [72]. This step was implemented to remove moisture and other surface contaminants that could interfere with adhesion.

Immediately after the bake, to prevent condensation, Surpass-3000 adhesion promoter was applied following the same method as in the previous iteration. The sample was then promptly transferred to the spin-coater, where the resist was applied using the same spin-coating recipe as before.

Inspection of the resist covered samples was performed using optical microscopy, and again no visible defects indicating an issue with resist adhesion or the spin-coating were observed.

The exposure process was carried out using the same parameters as in the previous sample, with the same mask design, and developed using the same equipment and recipe as before. An example of the resulting pattern can be seen in Figure 26. It can be observed that once again, the fidelity of the pattern is high, with no visible defects or indication of issues with the exposure process.



Figure 26: Optical microscopy image of the patterned resist after exposure, showing high fidelity in pattern transfer with no visible defects. 10x magnification.

5.2.3 Etching of the InGaAs/InP epitaxial Layers

While the addition of the InP capping layer improves the overall quality of the epitaxial structure, it also introduces additional complexity to the etching process. In the previous iteration, etching was straightforward, as it only required the selective removal of the InGaAs, however, with the presence of the 10 nm InP cap, a sequential etching process was required: First, etching the InP top-layer, followed by the InGaAs layer.
This additional step requires precise etching control to selectively remove each layer while preserving pattern fidelity and resist integrity. While this modification enhances QD growth uniformity in later stages, it increases the overall fabrication complexity.

The etching process is outlined in Table 5 in Section 4.2.3. Similar to the previous wet etch, the InGaAs was etched using a sulfuric acid-hydrogen peroxide solution, while the InP was first etched using a hydrochloric-phosphoric acid solution. Multiple samples were etched with slight variations in InP etching time to assess consistency. As shown in Figure 15, the etch rate for the InP layer was approximated at 2.85 nm/s with an uncertainty of ± 0.33 nm/s.
However, the validity of this estimate is questionable due to significant variability in the data points. Specifically, while an etch rate of 2.85 nm/s would predict a 10 nm removal in just 3-4 seconds, the actual etching test revealed a depth of 12 nm in 8 seconds, significantly lower than expected. This discrepancy suggests that the etch rate may be overestimated, potentially due to the high viscosity of the etchant, which could slow down the effective material removal. Given this uncertainty, etching times were systematically varied between 3 and 10 seconds in 1-second increments to better characterise the actual rate and ensure process reproducibility.

The effects of the varied etch times on the InP layer showed tremendous variability, as can be readily seen in Figure 27.

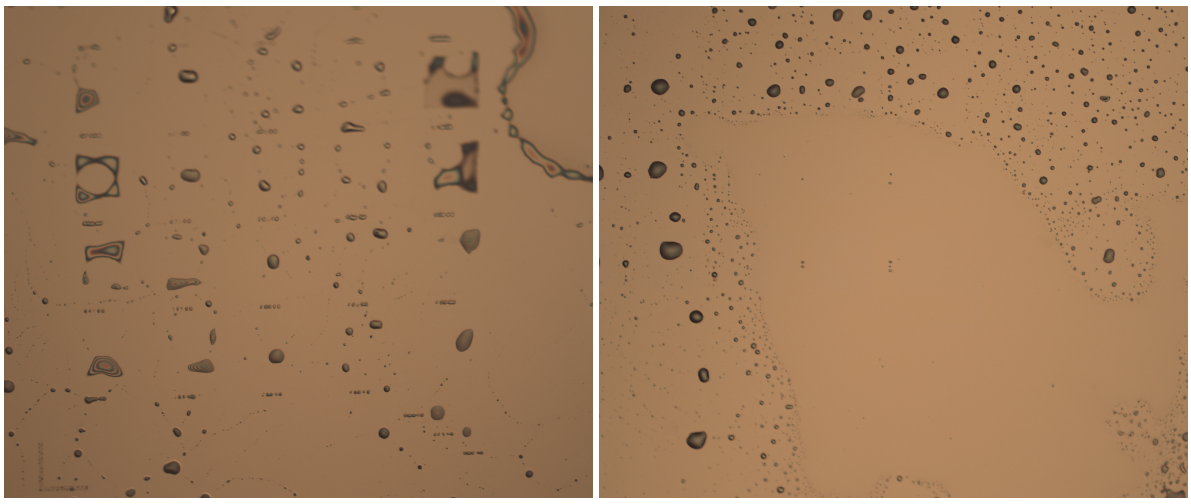

Figure 27: Left: Sample A1, InP-layer etch duration of 5 seconds. Right: Sample A3, InP-layer etch duration of 7 seconds. Both samples were subsequently etched with the solution for InGaAs for 16 seconds. 10x magnification.

The etching results showed significant resist degradation across all samples, although distinct variations in morphology and pattern retention were observed. The right sample in Figure 27, which underwent a longer H_3PO_4:HCl etch (7 s versus 5 s for the left sample) prior to the subsequent H_2O_2:H_2SO_4:H_2O etch, exhibited nearly complete pattern degradation, whereas the left sample retained faint but discernible labels.
Resist island formation was observed in both cases, but in the right sample these islands were strangely absent near the patterned regions. This suggests an interplay between etchant viscosity, surface conditioning effects, and resist interactions with the etchants, which has also been observed and discussed in other studies [74][75].

Due to the unusual thickness of the etchant, we immediately considered the role of etching kinetics, as investigated in [76], which asserts that when the reaction rate is limited by mass transport, a concentration gradient of the active etching species can develop at the solid/solution interface. In a viscous solution like our etchant, where the mass transport of reactants and by-products is inherently slow, the efficacy of the etching process may become unpredictable. A highly viscous etchant, such as H_3PO_4, may not diffuse away from the surface in a proper manner, for instance during the rinse step. As a result, remnants of the etchant could persist locally, leading to unintended effects even after the sample has been immersed in a new solution. This raises the hypothesis that etchant retention is an indirect consequence of the high viscosity, as slower diffusion rates hinder the transport of reactive species away from the surface.

The unintended effects of etchant retention could potentially be twofold:

First, the formation of resist islands near the patterned regions in both of the samples in Figure 27 suggests that residual H_3PO_4 may have acted as a buffer layer between the resist and the second etchant. This buffering effect could have altered the interaction between the resist and the subsequent H_2O_2:H_2SO_4:H_2O etch, preventing immediate peeling and instead leading to a more gradual degradation process. Rather than complete delamination, it is possible that retained phosphoric acid partially dissolved or weakened the resist, leading to a redistribution of smaller resist fragments instead of large-scale peeling. This is somewhat consistent with previous observations, Poulin et al. [74] observed that residual etchants can catalyse the dissolution of photoresists when phosphoric acid interacts with organics.

However, this buffering effect does not explain why the resist islands form away from the patterned regions in the sample shown to the right in Figure 27, with the pattern itself being almost entirely removed. Since the phosphoric-hydrochloric acid etch-duration was longer in this case, it would stand to reason that the buffer layer would be at least equivalent or perhaps greater than in the left sample.
Instead, it is possible that the patterned region facilitated a more extensive dissolution of the resist. Since the pattern contained openings in the resist, the etchant may have diffused more effectively into and underneath the resist during the extended etching period, leading to increased degradation. Following this heightened weakening, compared to the other sample, exposure to the second etchant could have completely removed the resist in these areas, as the resist was

already compromised.

This hypothesis, however, is not as compelling as the buffering effect explanation, as it seems unlikely that an increase of just two seconds in etch time alone could induce such a dramatic difference in local resist degradation. Although the viscosity of the etchant is high, the additional etching duration should not have significantly altered the penetration depth of the etchant to such a pronounced extent.

It is likely that the observed degradation during etching is a combination of several factors, including the viscosity of the etchant, the resist composition and integrity, etch duration, rinse efficiency, resist-etchant interactions, and possibly inherently stochastic effects. Furthermore, H_3PO_4-based etching is a common wet-chemical method for InP, typically employing higher H_3PO_4 to HCl ratios, such as 3:1 [65] [67]. In this context, etch rates around 1000 nm/min have been reported for InP using a 3:1 H_3PO_4:HCl solution.

Given that 10 nm is a relatively thin layer for a wet-chemical etching process that is typically used for much thicker layers, the standard etchant compositions may not be optimal for this specific application. Therefore, further studies into the etching dynamics and concentration adjustments for this specific process should be conducted to fully understand the mechanisms and to achieve a successful etch on thin InP epitaxial layers.

Since resist degradation was observed across all samples, independent of etchant composition, dilution, or material system, the most plausible explanation is that the resist itself was compromised. In particular, the finding that the resist began to peel when exposed solely to a DIW dip (Figure 25), despite treatment with an adhesion promoter, was a strong indicator.
The automatic spin-coater used in the resist application process has previously experienced solvent evaporation issues, resulting in unintended variations in resist thickness. Instead of adhering to the target value of 180 nm, the resist layer often exceeds this thickness, approaching approximately 200 nm.

Given the prior malfunctions of the equipment, we opted to attempt the etching again, using a sample that had been coated prior to the project. This allowed us to assess whether the pre-existing coating exhibited greater resistance to the etching process, thereby providing a definitive evaluation of the current resist's performance, and potentially allowing us to move forward with the fabrication process.

5.3 Fabrication Using Pre-coated InGaAs/InP Sample

The pre-coated legacy sample was fabricated on the same premise as ours, with similar, but not identical fields, as shown in Table 8. The sample underwent a similar process as ours, having had the same MOVPE growth procedure, as the sample in Section 5.1: It was a 2-inch InP (011) substrate, with a 16 nm InGaAs layer grown on top. It was then dipped in adhesion promoter, rinsed in DIW, and coated, using the same resist as in our sample, CSAR.
It was however visually evident that it differed from ours, as the faint tint of the resist was more pronounced, as it had been coated during the era where solvent had partially evaporated from the spin-coaters liquid containers, and the resist was therefore thicker, resulting in a coating with a thickness closer to 200 nm.
After the resist-coating process, the sample was exposed in the same E-beam writer as our sample, using the same standard configurations, and the same acceleration voltage. The sample was then developed in the same developer, and rinsed in DIW.

At this stage of the fabrication process, we adopted the sample shown in Figure 28.



Figure 28: Optical microscopy image of the pre-coated legacy sample after resist development. The observed coloration difference compared to previous samples is mainly related to the in light intensity settings during imaging. 10x magnification.

5.3.1 Etching of InGaAs Epitaxial Layer and Resist Removal

The etching process was performed using the slightly diluted 1:1:100 H_2SO_4:H_2O_2:H_2O solution, as opposed to the originally proposed 1:1:80. Following the etch, the sample underwent a deionised water (DIW) rinse and was subsequently dried with a nitrogen blow.

In contrast to previous etching attempts, no significant visual changes were observed upon initial inspection. The resist remained fully intact, with no signs of degradation under optical microscopy.

The sample was then transferred to the solvent fumehood, where chemical resist removal was undertaken. For this particular sample, the advanced resist removal process outlined in Table 6 was used, however later testing showed no discernible differences in resist-removal efficacy between the simple and advanced stripping processes, as can be seen in Figure 29.



Figure 29: OM images of resist removal test, without the descumming step. Both samples were InGaAs on InP. Left: Advanced resist removal process. Right: Simple resist removal process.

The sample was then transferred to the SEM for imaging.
The SEM analysis confirmed that both the etching and resist stripping process was considerably more successful, with the resist having been removed fully, and the fidelity of the pattern being high. This strongly implies that the previously observed resist deterioration was not an inherent material issue but rather a problem associated with the specific spin-coater and its CSAR resist.

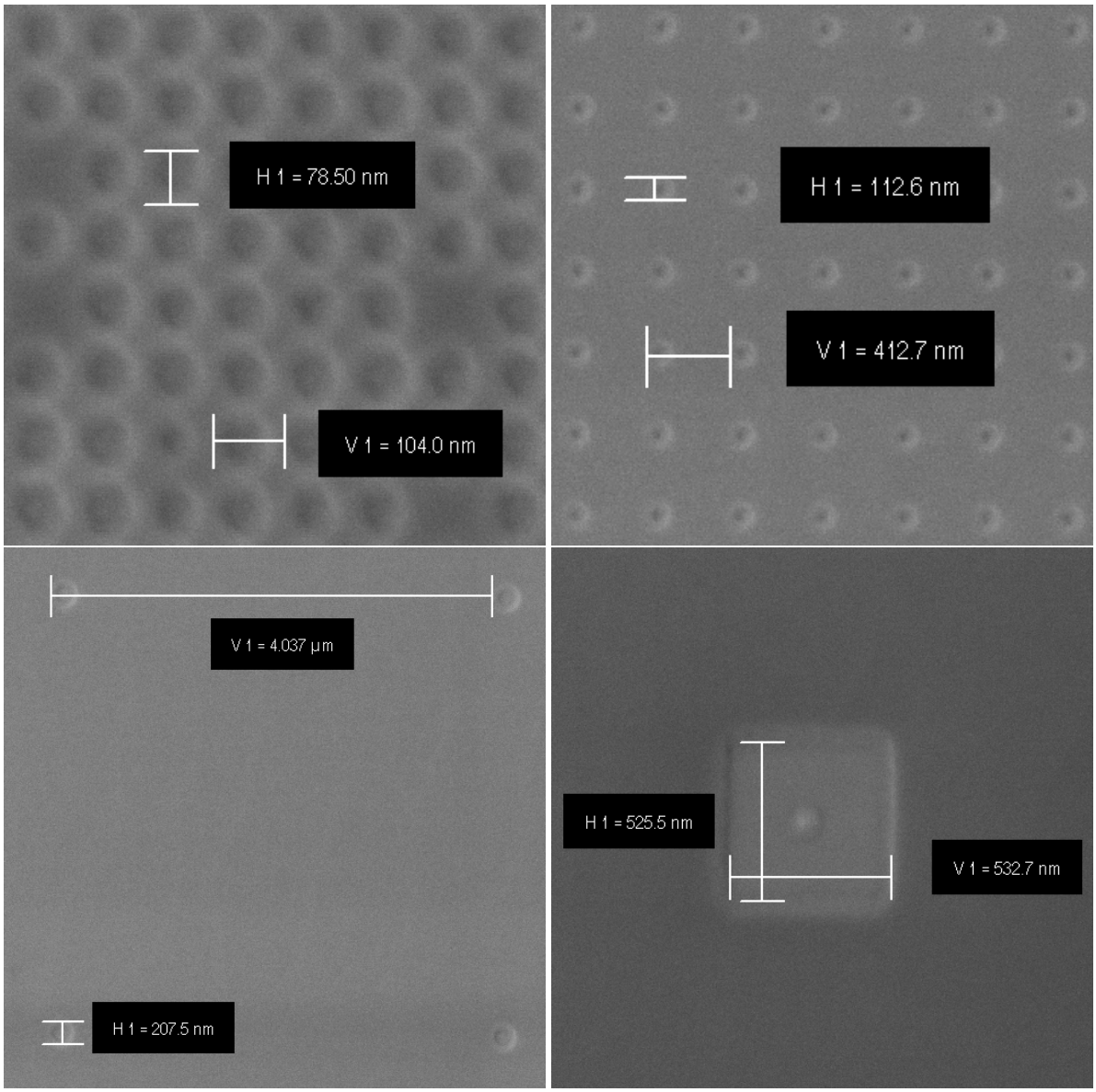

Figure 30: Top left: A3, top right: C4, bottom left: H14, bottom right: P10. The samples were imaged using InLens mode, with an acceleration voltage of 3kV.

In the SEM images shown in the figure and Table 8, we observe that, particularly for smaller hole diameters, the etch was slightly more aggressive than anticipated, resulting in an increase in diameter by a factor of 2 in some cases.
It should be noted, however, that these measurements are subject to considerable uncertainty and may not be fully representative of the entire fields. Several factors contribute to this imprecision, including the limited sample size of measurements and the discrete resolution of the measurement annotations: The annotation system operates with quantised measurement steps, meaning that diameters are recorded in fixed increments, which inherently introduces a systematic error.

For the top-left image, depicting field A3, in Figure 30, the holes exhibit high variability in both size and shape, lacking well-defined edges. The etching process appears to have been inconsistent, leading to a mixture of over-etched and under-etched regions, with some holes extending beyond their intended dimensions due to over-etching, others exhibited incomplete etching, resulting in marginal topology change.

This phenomenon was not present across the entire field but was specifically selected for imaging to highlight its occurrence.
It is possible that the variability in this particular field is simply a by-product of small feature size, and thus any deviations appear larger in magnitude.

Another contributing factor to the observation of larger hole diameters, could be related to the plasma ashing process used for descumming prior to etching. In this project, we used an O_2 flow rate of 300 sccm at 400 W.
However, laboratory guidelines recommend a lower process power of $\sim$200 W for descumming [59], which then presents a fundamental trade-off: using a lower descumming power minimises the risk of pattern erosion, but increases the risk of resist residues, which may affect subsequent fabrication steps.

Finally, the etch itself, H_2SO_4:H_2O_2:H_2O on InGaAs in the (011) crystallographic orientation, produces positively tapered sidewalls, where the openings at the top are wider than at the bottom [75]. While this tapering may contribute to the observed hole widening, its impact is likely marginal compared to the erosion from Plasma ashing, and possible over-etching during the dip itself.

The top-right and bottom left images show fields C4 and H14, respectively. Both of these fields show a regular pattern, with no holes observed that experienced under-etching. Slight variations from the expected hole-diameter, Table 8, can be seen, but the holes themselves are generally uniform.

The final image, located in the bottom-right of Figure 30, shows a hole from field P10, where the geometry was non-circular. The sidewall definition is sharp, and the corners appear well-defined and nearly straight, indicating that the etch achieved a high-fidelity pattern transfer to the InGaAs.

Label	λ_{Design} (nm)	$\varnothing_{Design}$ (nm)	$\lambda_{Measured}$ (nm)	$\varnothing_{Measured}$ (nm)	**Geometry**
A3	100	30	100	50-70	Circular
B4	200	40	200	100	Circular
C4	400	40	400	100	Circular
D4	600	40	600	100	Circular
E4	1000	60	1000	90	Circular
E6	1000	60	1000	100	Circular
F4	2000	40	2000	80-100	Circular
F6	2000	60	2000	140	Circular
F10	2000	100	2000	150	Circular
H4	4000	40	4000	100	Circular
H8	4000	80	4000	150	Circular
H14	4000	140	4000	200	Circular
6u4	6000	40	6000	100	Circular
6u10	6000	100	6000	150	Circular
8u4	8000	40	8000	100	Circular
8u10	8000	100	8000	150	Circular
P8	4000	500 (80)	4000	500 (N/A)	Square
P10	4000	500 (100)	4000	500 (N/A)	Square
P12	4000	500 (120)	4000	500 (120)	Square
P15	4000	500 (150)	4000	500 (N/A)	Square

Table 8: Geometric and dimensional parameters of the fields in the pre-exposed sample. The additional columns represent the intended pattern dimensions from the GDS file. The "()" in the P denote the size of a pillar structure inside the holes.
λ = pitch, $\varnothing$ = diameter.

Based on these results, the etch was deemed successful, and we proceeded to the final growth with the sample.

5.3.2 Epitaxial Growth of InP Top-layer and InAs Quantum Dots

The growth, outlined in Section 4.2.5, Table 7, and Figure and 17, was then performed.
From visual inspection alone, it appeared that the sample had obvious irregularities. These can be seen in Figure 31, an OM image showing the entire pattern post-growth. The fields appeared to have grown, extending beyond the labels, and small islands was observed in the center of each field.



Figure 31: OM of the sample post-growth. The fields have laterally expanded, and small islands formations are visible at the center of each field. An observable change in hue, both optically and visually can be seen. 10x magnification.

While the macroscopic and OM inspection of the sample initially suggested a growth failure, SEM imaging was performed to investigate if any quantum dots had nucleated successfully.

We found that while the sample generally had experienced deterioration, some quantum dots could be observed.
These quantum dots, however, were highly irregular in distribution, size and morphology. This is particularly evident in Figure 32, an image using the InLens detector, with 0° tilt, which highlights an elongated quantum dot, being 50 nm nanometers longer in one direction. The highlighted quantum dot itself is also rather large, especially when considering other nearby QDs in the image.
Beyond the variations in size, the quantum dots displayed highly variable morphologies, with many deviating from the expected rounded shape: Several dots appeared elongated or irregularly faceted, with low uniformity. This is also evident in Figure 33, which further shows the inconsistent nucleation and growth dynamics observed across the sample. These images were taken from field E6, which was designed with a 1000 nm pitch; however, closer examination of the few quantum dots that seemed to form a small, localised array (see Figure 33, right) had a pitch of about 500 nm instead, with some variation. This likely indicates that these localised arrays were merely stochastic QD's that aligned themselves in a semi-ordered way, without the patterned holes having much of an effect.

A final observation from these images is the poor planarisation of the InP epitaxial layer. The SEM images reveal that instead of forming a well-integrated and continuous film, the InP layer had localised height variations. These height variations were explored further using AFM characterisation.

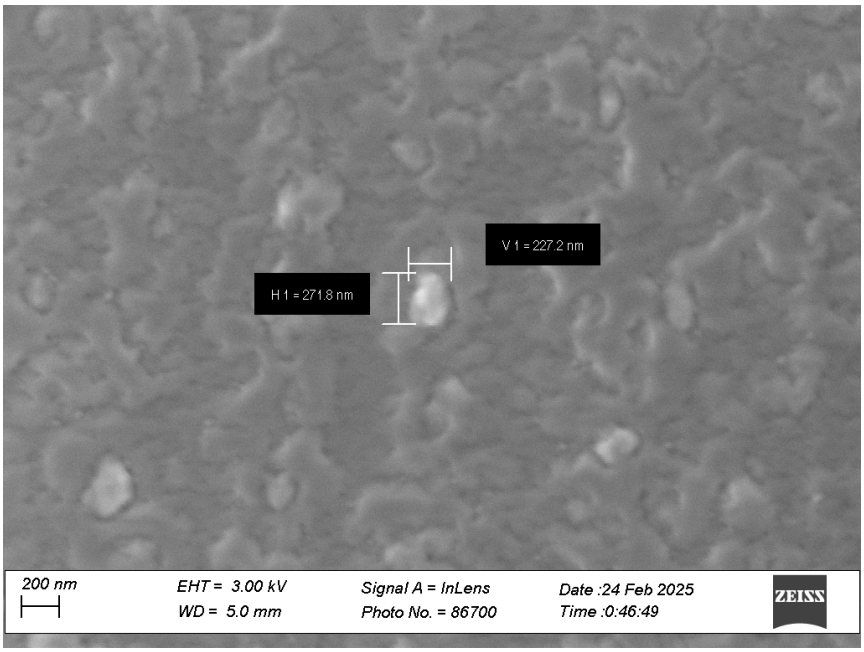

Figure 32: SEM image of randomly organised quantum dots on the InP epitaxial layer. The highlighted quantum dot appears elongated. Significant variation in nearby quantum dots' size and morphology is observed.

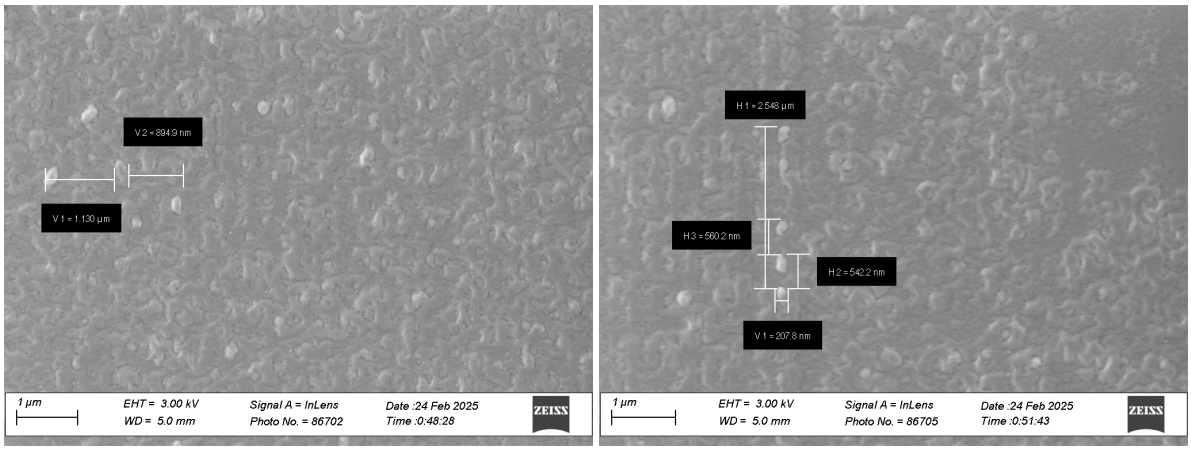

Figure 33: SEM images showing variations in quantum dot distribution. The quantum dots are also clearly irregular in shape, likely due to to the poor surface planarisation observed.

Using standard AFM tapping mode, the images in Figure 34 were produced. The left image reveals a highly granulated surface, with significant height variations across a relatively large scan area, highlighting that the InP capping layer is not remotely planarised, as the peak-to-valley height variations reach up to 127 nm.

The right image, provides a high-resolution examination of what appears to be a quantum dot. The suspected quantum dot stands approximately 25 nm in height when measured relative to the surrounding surface peaks, and 64 nm when referenced from the lower valleys in the local topography.

These AFM measurements are in line with the SEM observations, reinforcing that the InP capping layer suffers from poor planarisation, with localised regions of excess material deposition, causing the irregularity in quantum dot growth.

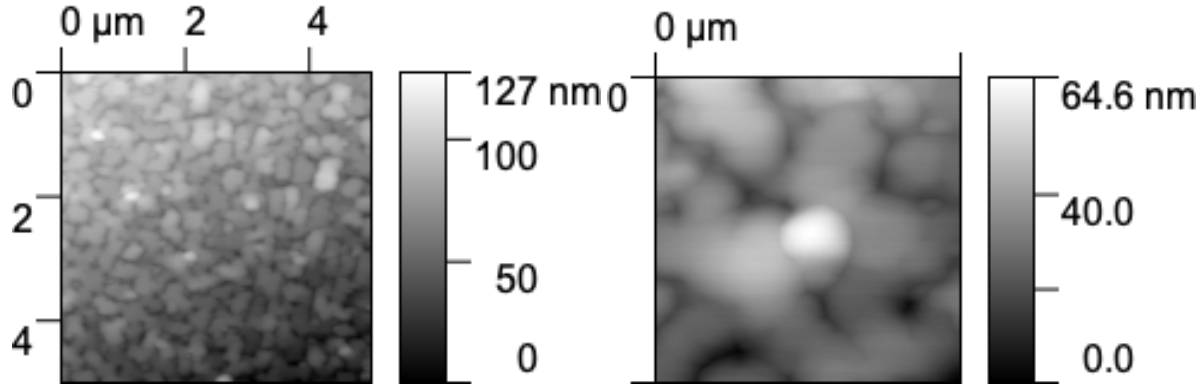

Figure 34: AFM images of the InP epitaxial layer. Left: A 5x5 μm^2 scan to show significant height variations, with peak-to-valley differences reaching $\sim$100 nm. Right: A 1x1 μm^2 scan showing a suspected quantum dot, measuring $\sim$ 25 nm in height relative to surface peaks.

5.3.3 AsH_3-Enhanced Epitaxial Growth for Improved Planarisation

To address the issue of poor planarisation, we modified our growth sequence by introducing arsine earlier in the process. This should enhance surface stabilisation, reduce indium desorption, and promote uniform nucleation sites for InAs QDs, leading to improved layer planarisation and more consistent QD morphology, than observed in the previous sample.

The change is based on previous observations [77], which demonstrated that an optimised As/P exchange process significantly improves QD height distribution and overall surface morphology. By introducing AsH_3 before the growth of InAs QDs, a stabilised arsenic-rich surface is established, effectively limiting the diffusion of indium adatoms and suppressing their desorption. This should result in a more uniform and well-integrated InP capping layer, reducing the height variations and roughness observed in previous growth attempts.

After the growth, the sample had a concerning light-blue tint to it, however, upon examining the sample in the SEM a noticeable improvement in surface morphology was observed in certain regions. Despite this enhancement, irregular topographical features remained persistent, so while the early introduction of AsH_3 contributed to local surface stabilisation, it did not entirely eliminate non-uniformities across the sample.

The surface topology of the sample was characterised using SEM and AFM to evaluate the effectiveness of the growth modifications. The SEM image in Figure 35 reveal that despite the introduction of early AsH_3, significant topographical irregularities persist. The figure illustrates widespread island-like formations, which were consistently observed throughout the sample. These hilly features reflect a continued imbalance in precursor diffusion and nucleation dynamics, leading to randomized surface roughening rather than a well-integrated planar film, despite increasing the arsine flow in the chamber during growth.

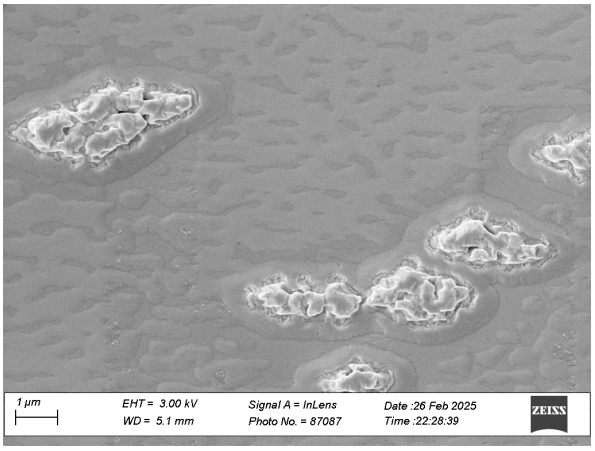

Figure 35: SEM image of the sample surface and widespread irregular island-like structures. The islands varied in size, but were generally on the order of 1-3 μm in length.

The persisted presence of poor planarisation was verified by AFM measurements, as seen in Figure 36. The scan, performed over a 4×4 μm^2 area, confirms the persistence of substantial height variations, with peak-to-valley differences reaching 100 nm. This surface instability further confirmed that strain relaxation effects and non-uniform precursor incorporation continued to impact the growth dynamics, leading to inhomogeneous deposition across the sample.
Despite this, it is likely that quantum dots still nucleated at the light-gray peaks, as small, highly localised white specks can be observed on the surface. Based on the color scale provided in the legend, these specks correspond to height variations of approximately 30 nm. The placement of these dots seem highly stochastic, likely a product of the randomly distributed peaks and valleys in the scanned area.

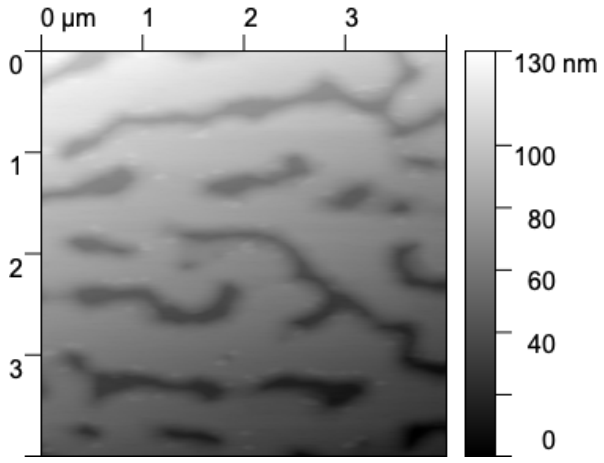

Figure 36: AFM image of the sample surface showing pronounced height variations, with peak-to-valley differences reaching up to ∼100 nm, confirming persistent surface roughness. Suspected quantum dots can be seen, extending from the peaks, with heights of ∼30 nm.

Despite the sample generally having poor planarisation, certain regions exhibited improved surface topology, particularly in areas where a patterned template was present prior to growth. However, these improvements were highly localised, appearing only in isolated regions. One of these regions, found in field A3, can be observed below in Figures 37 and 38. As shown in Table 8, the expected pitch of these localised structures is approximately 100 nm, and our measurements confirm this with high accuracy within these small local growths, as seen in the left SEM image. These hyper-localised arrays within the semi-planar sub-regions number between 5 and 20 quantum dots each.
Despite the pitch-measurements being in alignment with our expectations, it was evident that the QDs themselves did not exhibit the same uniformness in size. According to Table 8, the expected QD diameter ranges between 50 and 70 nm, yet the right-hand image in Figure 37 reveals that only a subset of QDs conform to these dimensions. Notably, QDs positioned near the center of these hyper-localised arrays appear to fall within the anticipated size range, whereas those located further from the center show a gradual reduction in size, suggesting a spatial dependency in growth dynamics.

A possible explanation for this spatial dependency is that the center QDs become preferential aggregation sites due to their proximity to surrounding material. If the supply of available adatoms is limited, a competitive growth dynamic could arise, where the proximity effect increases adatom consumption in the center, promoting faster growth. The smaller size of QDs at the edges of the localised arrays supports this hypothesis, as they have fewer adjacent sites to draw material from, leading to reduced growth rates and size discrepancies across the array.

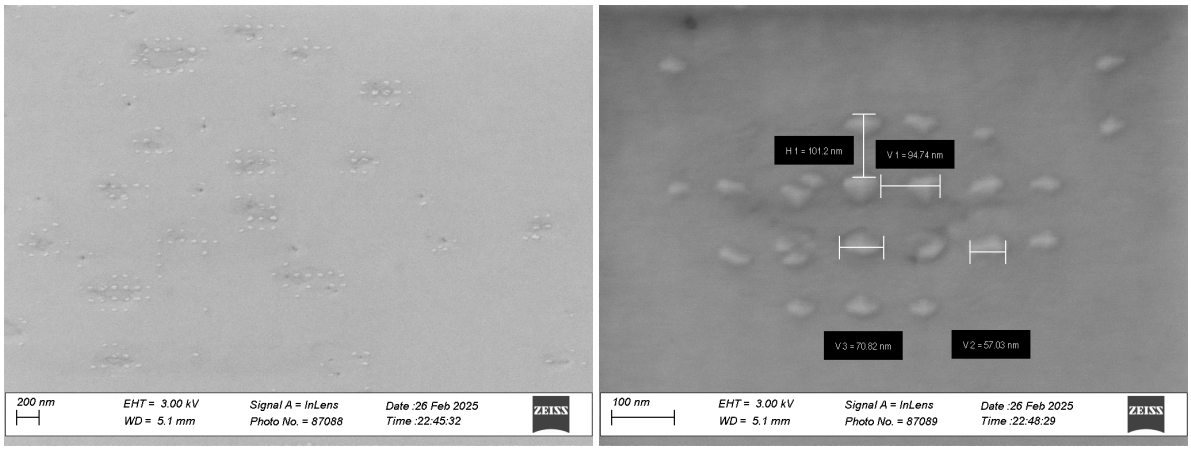

Figure 37: SEM images of localised regions exhibiting improved planarisation. The periodicity suggests that growth conditions in these areas allowed for more stable material incorporation, reducing large-scale roughness.

Other patterned regions, with poorer planarisation were also investigated for completeness sake. In Figure 38, the field F4 is shown, with sparsely populated quantum dot formation. However, despite the low count of nucleations, the measured QDs align with the expected pitch, indicating that the designed growth sites still acted as preferential points of aggregation. This supports the idea that localized strain fields at these sites promoted nucleation, even under conditions of limited surface diffusion. This observation reinforces a direct relationship between surface morphology and the extent of stochastic growth. While this region exhibited topographical variations, they were less severe than others, for instance in Figure 36, where extreme height fluctuations occurred. The reduced surface roughness likely improved adatom diffusion, minimizing random QD formation.

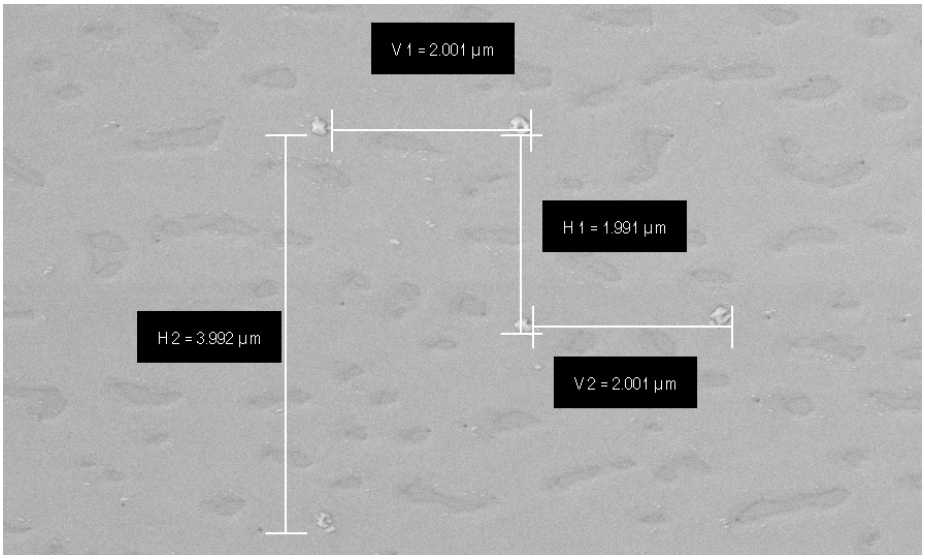

Figure 38: SEM image of a patterned region (F4) where more abrubt topology changes persist.

A final observation is related to the morphologies of the quantum dots themselves. Below in Figure 39, the height map (left), and adhesion (right) measurements of a 1.5 x 1.5 μm^2 scan be seen for one of the P-fields, but the same phenomenon can be observed in all observed fields, see Figure 37: Some of the InAs did not nucleate into single, well-defined dots, but instead materialised as clusters of multiple smaller dots right next to eachother, sharing a single pre-defined nucleation site.

One possible explanation is that local variations in strain and surface energy created multiple energetically favorable nucleation sites within the same pre-defined site, leading to a breakdown of the formation process. This explanation seems reasonable for the observations in the P-fields, where the patterned sites are relatively large (500 nm x 500 nm). Within such areas, QDs could reach a natural size threshold, beyond which further growth becomes energetically unfavorable. However, this does not explain the site-sharing QDs observed in Figure 37, as these QDs do not appear significantly larger than those that formed adjacently. This suggests that an alternative mechanism, beyond simple size limitation, may be responsible for the unusual nucleation behavior in these regions.

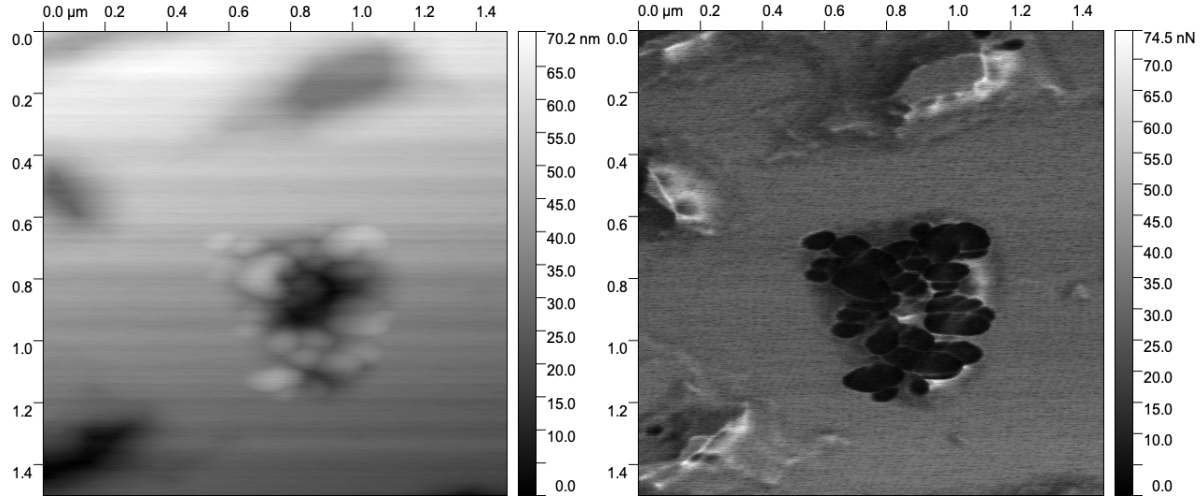

Figure 39: AFM scan using the (Left): height metric. The peak-valley difference is 70 nm. (Right:) adhesion metric. The adhesion scan was included to provide a more clear image of the surface and its properties.

6 Conclusion

The goal of this project was to fabricate strain-induced, site-controlled quantum dot structures through pre-patterning with high-resolution electron beam lithography, followed by the controlled self-assembly of quantum dots within the Stranski-Krastanov growth regime using Metalorganic Vapour-Phase Epitaxy. By applying these fabrication techniques, we aimed to achieve deterministic quantum dot placement with optimised uniformity and reproducibility.
This work explores the physics of quantum confinement effects, the self-assembly process, and the various epitaxial growth regimes, applying these principles to develop uniform fields of indium arsenide quantum dots at predefined locations on a III-V material system.
Experimentally, multiple growth and processing iterations were conducted to address challenges, particularly resist peeling during etching and poor planarisation during QD growth. The initial approach, using an InGaAs-on-InP epitaxial layer, failed before the final InP/InAs growth due to etching issues. A second attempt, in which the InP top layer was grown in the same sequence to improve planarisation also failed at the etching stage, leading to the conclusion that the issue was related to the resist. To resolve this, a third pre-coated sample of InGaAs on InP, was used, which saw successful etching and subsequent InP and InAs quantum dot growth. Two growths were performed, as the first growth suffered from poor planarisation and stochastic dot formation, while the second attempt, with earlier arsine introduction, improved growth dynamics and yielded hyperlocalised quantum dot arrays, though planarisation issues persisted. The samples were characterised using optical-, atomic force- and scanning electron microscopy.
The results demonstrated that growth conditions, particularly precursor introduction during growth, significantly influence quantum dot formation. However, despite successfully producing quantum dots, the site-control aspect showed varying degrees of success. As discussed in the results, this likely had to do with poor planarisation, causing disruptions to adatom surface diffusion, and consequently, to the uniformity of quantum dot formation.
Future work should focus on improving planarisation by refining the growth sequence. Growing an additional InP layer directly on InGaAs during the initial stage before the final InP/InAs growth could help reduce lattice mismatch effects and enhance surface uniformity, leading to more controlled quantum dot formation. Additionally, optimisation of the etching process for InP is necessary: The excessive viscosity of the current phosphoric-hydrochloric acid etch likely impeded mass transport and process control. Exploring alternative dilution strategies, such as using water instead of just increasing the concentration of phosphoric acid, would reduce viscosity, possibly making the process more sustainable and reproducible. Alternatively, an InP etching solution without phosphoric acid, like H_2O:HCl could be employed, which also exhibits selectivity toward InGaAs, although to a lesser extent [67, 65].
In conclusion, this research has demonstrated a structured approach to quantum dot fabrication, highlighting key challenges in site-control and planarisation in MOVPE epitaxial growths. The findings highlight the critical role of growth sequence optimisation and precursor introduction in achieving deterministic quantum dot placement.

7 Appendix

7.1 Exposure Mask Topology Optimisation

In wafer design, a commonly encountered problem is optimising the layout of ones design, in this case the number of chips, that can be fitted onto a circular wafer. Maximising the chip-per-wafer (also known as die-per-wafer (DPW)) can have a substantial impact on the overall yield, costs, and resource usage.
Some standard tools and resources to calculate the DPW number is freely available on the internet [1][2], however these are often limited to the most common wafer dimensions such as 4, 6 and 8 inch wafers, or are restricted in some dimension, most commonly inter-chip spacing.
To combat this problem, we created a custom topological optimaisation procedure, employing the widespread probabilistic optimisation technique simulated annealing, to maximise the yield of each wafer produced.

7.1.1 Problem Definition

The main objective is to determine the optimal arrangement of square chips (or dies) on a circular wafer with a diameter $d = 50.8$ mm. Each chip has a fixed side length $s = 1$ mm, and there is a specified spacing $g = 8$ mm between adjacent chips. Due to the circular shape of the wafer, some chips near the periphery may fall outside the usable area and therefore need to be excluded from the count.

Furthermore, an "edge exclusion zone" must also be considered: this region is deliberately left unpatterned or unused due to various process limitations, such as resist adhesion issues, edge bead formation, and the challenges in maintaining uniformity near the wafer's edge during lithographic processes. We estimate the edge exclusion zone to be 2 mm in width, extending inwards from the perimeter, which reduces the effective diameter to 46.8 mm.

Thus, calculation of the maximum Die Per Wafer (DPW) is constrained by:

- The wafer diameter, d.
- The effective diameter, d_e.
- The chip sidelength, s.
- A fixed spacing, g, between chips.

[1] https://anysilicon.com/die-per-wafer-formula-free-calculators/
[2] https://www.silicon-edge.co.uk/j/index.php/resources/die-per-wafer

To explore the implemented optimisation, we start with the simplest configuration strategy, which is placing a chip precisely at the centre of the wafer. Given that this is the origin of our coordinate system, we assign it coordinates

$$(0, 0)$$

. Following this, additional chips are arranged in a grid-like pattern with a spacing of g in the x- and y-directions. This pattern expands radially, with each successive layer of chips positioned at distances of $g, 2g, 3g, \ldots$ from the centre.

To ensure that each chip lies within the circular wafer boundary, we impose a constraint on the Euclidean distance from the wafer's centre. For a chip positioned at

$$(x, y)$$

, we require:

$$\sqrt{x^2 + y^2} + \frac{s}{2} \leq R,$$

where R is the effective radius of the wafer (after accounting for the edge exclusion zone). This condition guarantees that no part of the chip extends beyond the wafer's boundary. If this criterion is met, the chip is considered valid and counted towards the DPW.

Using the given chip and wafer dimensions, this approach systematically places chips in a circular pattern, with each successive layer filling available radial space until the boundary of the wafer is reached.

7.1.2 The Symmetric Solution

A common approach is to off-set the grid by a shift of $\frac{g}{2}$ in both the x- and y-directions. This adjustment ensures symmetry in the placement, aligning chips to optimise their fit within the circular boundary of the wafer.
By offsetting the grid, this method can reduce the amount of wasted space near the edges of the wafer and can improve the overall packing density. This symmetry-based placement is particularly effective when the wafer's dimensions and the chip's dimensions create alignment challenges at the boundaries.
The symmetry ensures a more balanced distribution of chips, and can make it easier to process later in the fabrication stages, as cleaving is a non-issue, unlike row based iterations, where overlap on dicing lines may occur.
The physical implementation of this solution is rather elegant and straightforward: By defining a grid that slightly extends beyond the boundaries of the wafer and incorporating the dimensional parameters, the necessary shifts are introduced. Chips that do not satisfy the constraints imposed by the wafer dimensions are simply excluded from consideration. This approach yields a symmetric solution that is not only easy to implement, but also rather useful in the fabrication stages.
The final DPW using the symmetric solution is 24, and can be seen in figure 40a.

7.1.3 Optimisation Using Greedy and Simulated Annealing Algorithms

However, there is an optimisation strategy, which produces a more unstable configuration, ie. is not guaranteed to be better than the two previous methods, but which can maximise the DPW significantly under certain circumstances. The optimisation process begins with a greedy algorithm, which generates an initial solution. The greedy approach systematically places chips on the wafer by iterating over potential grid positions and selecting valid placements that maximise the DPW. This is achieved by ensuring that each chip fits within the usable radius of the wafer and satisfies minimum spacing constraints. The greedy algorithm is deterministic, and produces a stable, replicable starting configuration, which is particularly advantageous as it provides a well-structured base for further refinement.

Once the initial greedy solution is obtained, the optimisation transitions to the simulated annealing phase. Simulated annealing is inspired by the physical process of annealing in materials, where materials are heated and then gradually cooled to reach a stable, low-energy state. In the context of die placement, simulated annealing enables a probabilistic exploration of configurations by introducing controlled randomness, allowing the algorithm to escape local maxima and explore a broader solution space. This phase refines the initial greedy configuration, aiming to identify an arrangement that yields a higher DPW.

The annealing process involves gradually lowering the temperature parameter, which controls the level of randomness in chip placement. Higher temperatures allow for greater variability and exploration, while lower temperatures focus on refining the solution by reducing randomness. At each iteration, a new configuration is generated, and if the new configuration improves the DPW, it is retained. Suboptimal configurations are also accepted probabilistically to avoid being trapped in local optima, following the probability:

$$P = \exp\left(-\frac{\Delta E}{T}\right) \tag{53}$$

where,

- P is the probability of accepting a worse solution,
- ΔE is the change in the objective function, calculated as $\Delta E = E_{\text{new}} - E_{\text{current}}$, where E_{new} and E_{current} represent the DPW values of the new and current solutions, respectively,
- T is the current "temperature," a parameter that decreases over time according to a cooling schedule.

Over time, the temperature decreases, reducing randomness and thus "freezing" the configuration towards an optimal layout. With this approach, we discovered a new configuration that accommodates an additional chip at both the top and bottom, along with an offset in the centre row, making the DPW to 25, as can be seen in figure 40b.

Despite the apparent symmetry, and increased DPW, we elected to go with the symmetric solution instead of the Greedy+SA solution, due to familiarity. However, we have demonstrated the more optimal DPW configurations can exist compared to the standard solutions of radial geometry and symmetrical placements.

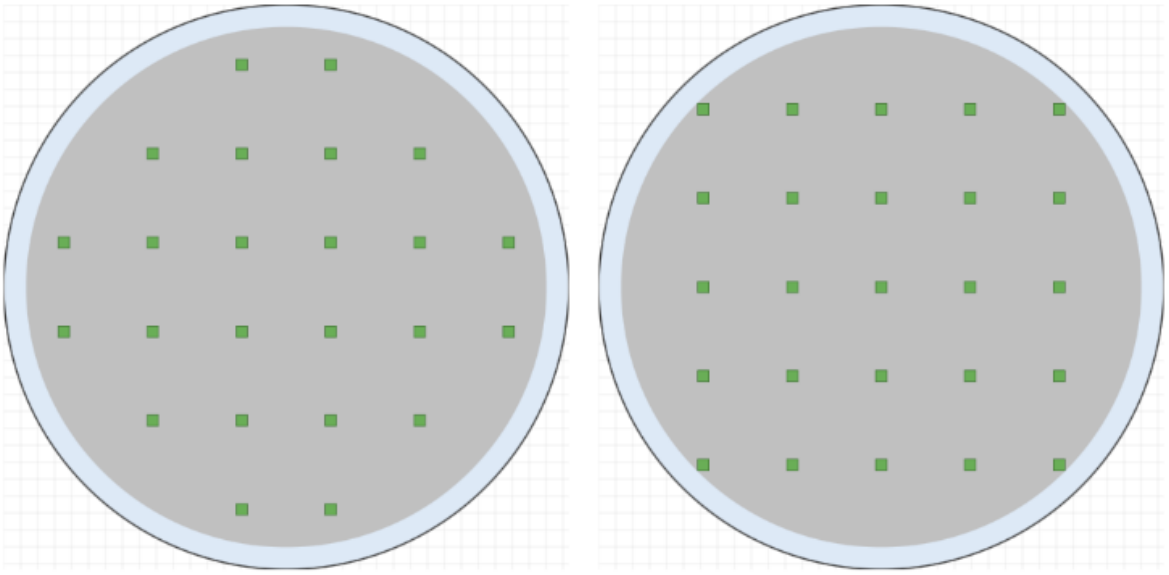

Figure 40: Comparison of chip placement strategies on a circular wafer. (a) The symmetric solution, which uses an offset grid to optimise chip alignment within the wafer boundaries, resulting in a total DPW of 24. (b) The greedy algorithm combined with simulated annealing, which further refines chip placement to maximise DPW, achieving an improved total of 25 chips by accommodating additional placements at the wafer's top and bottom.

7.2 Exposure Mask Generation

The code is hosted in it's entirety on `github.com/BjornFS`

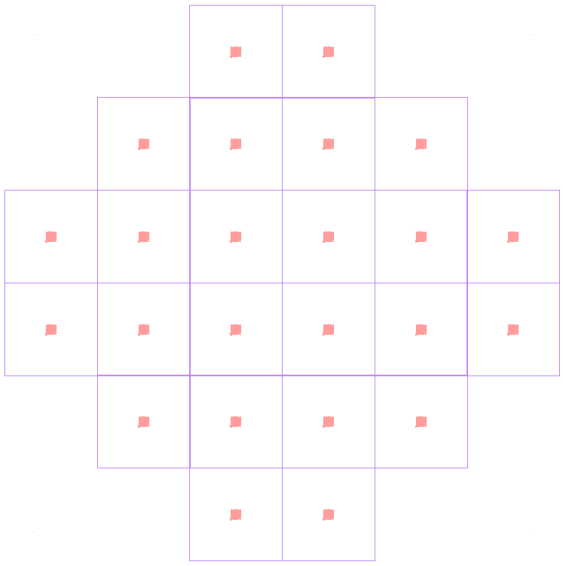

Figure 41: Layout of the 24 chips on the 2 inch wafer.

7.2.1 Compiler

```
def load_chip_positions(file_path):
    """
    Reads chip positions from a text file (csv).
    """
    chip_positions = []
    with open(file_path, 'r') as file:
        for line in file:
            x, y = map(float, line.strip().split(','))
            chip_positions.append((x, y))
    return chip_positions


def create_chip():
    """
    Generates a single chip layout without alignment marks.
    """
    chip_cell = gdspy.Cell("CHIP")

    with open("geometries.json", "r") as f:         # Load chip geometries
   from json file
        field_geometries = json.load(f)
```

```
    for field in field_geometries:                    # Add fields from the
   JSON data
        shape = field["shape"]
        diameter = field["diameter"]
        pitch = field["pitch"]
        domain_size = field["domain_size"]
        position = tuple(field["position"])          # Convert list to tuple
        field_generator = Fields(chip_cell, shape, diameter, pitch,
   domain_size, position)
        field_generator.create_field()

    label_generator = Labels(chip_cell, text_height=10) # Add field labels

    for field in field_geometries:
        shape = field["shape"]
        diameter = field["diameter"]
        pitch = field["pitch"]
        domain_size = field["domain_size"]
        position = tuple(field["position"])
        label_generator.generate_field_label(shape, diameter, pitch,
   domain_size, position)

    # Add scalebar
    scalebar = Scalebar(chip_cell, position=(-480, -480), length=100, width
   =10)
    scalebar.add_scalebar()

    spacer_generator = Spacers(chip_cell, grid_size=8000, layer=2) # Add
   spacers
    spacer_positions = [(0, 0)]  # Spacer centered around the chip
    for position in spacer_positions:
        spacer_generator.add_spacer(position)

    chip_label_position = (0, 0)                     # Add chip label
    label_generator.generate_chip_label("CHIP_1", chip_label_position)

    return chip_cell


def create_chip_array(chip_cell, positions_file):
    """
    Generates array of chips from positions from txt file and adds alignment
     marks once.
    """
    chip_positions_mm = load_chip_positions(positions_file) #Load chip
   positions from file

    chip_positions_um = [(x * 1000, y * 1000) for x, y in chip_positions_mm]
     #mm to um

    # Create a top-level cell for the array
```

```
    array_cell = gdspy.Cell("CHIP_ARRAY")

    # Add alignment marks
    alignment_marks = AlignmentMarks(array_cell, square_size=0.1)
    alignment_positions = [(21500, 21500), (21500, -21500), (-21500, 21500),
     (-21500, -21500)]
    alignment_marks.create_alignment_marks(alignment_positions)

    # Add each chip to the array at the specified positions
    for position in chip_positions_um:
        array_cell.add(gdspy.CellReference(chip_cell, origin=position))

    return array_cell


# Main Script
if __name__ == "__main__":

    chip = create_chip()                                    # Create the chip
   template
    chip_array = create_chip_array(chip, "positions.txt") # Create chip
   array w alignmentMarks
    gdspy.write_gds("Exposure_InAs_QDs.gds", unit=1.0e-6, precision=1.0e-9)
   #Save GDS file
```

7.2.2 Alignment Markers

```
class AlignmentMarks:
    def __init__(self, cell, square_size=0.1):
        """
        Initializes the AlignmentMarks generator.
        """
        self.cell = cell
        self.square_size = square_size

    def create_alignment_marks(self, positions):
        """
        Creates alignment marks at the specified positions.
        """
        half_size = self.square_size / 2
        for x, y in positions:
            # Define the bottom-left and top-right corners of the square
            bottom_left = (x - half_size, y - half_size)
            top_right = (x + half_size, y + half_size)

            # Create a square and add it to the cell
            self.cell.add(gdspy.Rectangle(bottom_left, top_right))
```

7.2.3 Field Generation

```
class Fields:
    def __init__(self, cell, shape, diameter, pitch, field_size, position):
        """
        Initializes the ShapefieldGenerator for creating a field with
    specified shapes.
        """
        self.cell = cell
        self.shape = shape
        self.diameter = diameter
        self.pitch = pitch
        self.field_size = field_size
        self.position = position

    def create_shape(self, x, y):
        """
        Generates the specified shape at given (x, y) based on shape type.
        """
        radius = self.diameter / 2
        if self.shape == 'circle':
            return gdspy.Round((x, y), radius, number_of_points=16)
        elif self.shape == 'square':
            return gdspy.Rectangle((x - radius, y - radius), (x + radius, y
    + radius))
        elif self.shape == 'diamond':
            return gdspy.Polygon([
                (x, y - radius), (x + radius, y), (x, y + radius), (x -
    radius, y)
            ])

    def create_field(self):
        """
        Generates a layout for a single field filled with the specified
    shape type.
        """
        # Determine max shapes per field
        shapes_per_side = int((self.field_size - self.diameter) // self.
    pitch) + 1

        # Calculate the offset to centre the field on the given position
        offset_x = -self.field_size / 2 + self.diameter / 2
        offset_y = -self.field_size / 2 + self.diameter / 2

        # Add additional global shifts
        global_shift_x = 100  # Shift the field 100 um to the right
        global_shift_y = 50  # Shift the field 50 um up

        # Create a unique cell for the field
        field_cell_name = f"{self.shape[0].upper()}_x{self.position[0]}_y{
    self.position[1]}"
```

```
        field_cell = gdspy.Cell(field_cell_name)

        # Generate shapes row by row
        for row in range(shapes_per_side):
            for col in range(shapes_per_side):
                x = col * self.pitch + offset_x
                y = row * self.pitch + offset_y
                shape = self.create_shape(x, y)
                field_cell.add(shape)

        self.cell.add(gdspy.CellReference(field_cell, origin=(
            self.position[0] + global_shift_x,
            self.position[1] + global_shift_y
        )))
```

7.2.4 Label Generation

```
class Labels:
    def __init__(self, cell, text_height=5):
        """
        Initializes the LabelGenerator for creating and positioning labels.
        """
        self.cell = cell
        self.text_height = text_height

    def generate_field_label(self, shape, diameter, pitch, domain_size,
   position):
        """
        Generates a text label for a domain field based on its shape,
   diameter, and pitch.
        """
        # Mapping dictionaries for pitch, shape, and diameter
        pitch_map = {0.2: "02", 0.4: "04", 1.2: "12", 2.0: "20", 4.0: "40"}
        shape_map = {'circle': "C", 'square': "S", 'diamond': "D"}
        diameter_map = {0.04: "40", 0.08: "80"}

        # Generate the label code
        pitch_code = pitch_map.get(pitch, "XX")
        shape_code = shape_map.get(shape, "X")
        dimension_code = diameter_map.get(diameter, "XX")
        text_label = f"{pitch_code}{shape_code}{dimension_code}"

        # Calculate label position above the domain
        x_pos = position[0] + domain_size / 3
        y_pos = position[1] + domain_size + 10

        self.add_text(text_label, (x_pos, y_pos))

    def generate_chip_label(self, chip_id, position):
        """
```

```
        Generates a label for the chip at the specified position.
        """
        x_pos = position[0]
        y_pos = position[1] + 500  # Place 500 um above the chip
        self.add_text(chip_id, (x_pos, y_pos))

    def add_text(self, text, position):
        """
        Adds a text label at the specified position.
        """
        x, y = position
        text_label = gdspy.Text(text, self.text_height, (x, y))
        self.cell.add(text_label)
```

7.2.5 Scalebar Generation

```
class Scalebar:
    def __init__(self, cell, position=(0, 0), length=100, width=10):
        """
        Initializes the Scalebar to create a scale bar with specified
   dimensions at a position.
        """
        self.cell = cell
        self.position = position
        self.length = length
        self.width = width

    def add_scalebar(self):
        """
        Generates a single L-shaped scale bar with the specified dimensions.
        """
        x, y = self.position

        # Generate the L-shaped scale bar
        points = [
            (x, y),
            (x + self.length, y),
            (x + self.length, y + self.width),
            (x + self.width, y + self.width),
            (x + self.width, y + self.length),
            (x, y + self.length)
        ]
        self.cell.add(gdspy.Polygon(points))
```

7.2.6 Spacing Visualisation

```
class Spacers:
    def __init__(self, cell, grid_size=8000, layer=2, line_width=10):
        """
        Initializes the SpacerGenerator to create spacers around chips.
        """
        self.cell = cell
        self.grid_size = grid_size
        self.layer = layer
        self.line_width = line_width

    def add_spacer(self, position):
        """
        Adds a square spacer around the specified position.
        """
        half_size = self.grid_size / 2
        x, y = position

        # Define the four corners
        bottom_left = (x - half_size, y - half_size)
        bottom_right = (x + half_size, y - half_size)
        top_left = (x - half_size, y + half_size)
        top_right = (x + half_size, y + half_size)

        edges = [                       # Define the edges of the square as
    lines
            [bottom_left, bottom_right], # Bottom edge
            [bottom_right, top_right],   # Right edge
            [top_right, top_left],       # Top edge
            [top_left, bottom_left]      # Left edge
        ]

        for edge in edges:
            self.cell.add(gdspy.PolyPath(edge, self.line_width, layer=self.
   layer))
```

7.3 Process Flow

Process flow title				Revision
Site-controlled Quantum Dots				**1.1**
DTU Nanolab	Contact email S183754@dtu.dk		Contact person Bjørn Nielsen	Contact phone 42200766
	Labmanager group Fabrication support	Batch name Initial QDs	Date of creation 16-Oct-24	Date of revision 1-Mar-25

Objective
Batch name: Initial QDs
Site-controlled quantum dots by means of strain. This process flow contains all the steps from purchased InP wafer to fabrication of the strained surface, and subsequent quantum dots, finishing with rigorous characterization of the dispersion of InGaAs Qdots on top-layer InP surface. 1. InP substrate 2. Epitaxial Growth of InGaAs 3. Spin Coating of E-beam Resist 4. E-beam Exposure 5. Development and Rinse 6. III-V Pattern Transfer (Wet-chemistry etching) 7. Resist stripping 8. Pre-growth Inspection 9. MOVPE growth of Q-dots 10. Post-growth characterization

Substrates									
Substrate	**Orient.**	**Size**	**Doping/type**	**Polish**	**thickness**	**Box**	**Purpose**	**#**	**Sample ID**
InP*	<011>	2”	P (Zn)	SSP	300±25µm	N/A	Device wafers	1	S1-S3

*Purchased from *WaferWorld*

Step	Heading	Equipment	Procedure	Comments
1	Preparation			**All wafers**
1.1	Wafer procurement		Purchase InP wafers	
1.2	Wafer approval		Obtain approval from the NanoLab staff to bring in purchased InP wafers	
2	Epitaxial Growth of InGaAs			**All wafers**
2.1	MOVPE growth	MOVPE	Place a 2" wafer, wafer segment (quarter), or chip in the correct stage slot, load the sample into the reactor and perform the growth. Recipe: "InGaAs Tstrain 16 nm", time: 39:48 (mm:ss) Target thickness: 16 nm Resulting [Ga;In] Fraction: [0.53; 0.47]	Critical thickness has been calculated to be ~27 nm
2.2	SEM Inspection	SEM Supra 3	Inspect initial surface homogeneity.	
3	Spin coating of CSARAR62 on III-V			**All wafers**
3.1	Surface treatment	Fumehood 08: III-V (dedicated	A pre-dehydration bake. Demands immediate application of resist, as shelf-life deteriorates quickly >> 5 min @ 120 °C Surpass-3000 dip for 30 seconds, followed by DIW dip for 60 seconds.	
3.2	Coat wafers	Spin Coater: Gamma e-beam & UV	**Resist:** CSAR (AR-P 6200, AllResist) **Spin:** 60 sec @ 5400 rpm (for appr. 180 nm) **Softbake:** 1 min @ 180 °C **Sequence**: (2318) DCH 50mm CSAR 180 nm	Soft bake is not a crucial step according to AllResist. CSAR is a positive e-beam resist.
3.3	SEM and OM Inspection	OM Nikon SEM Supra 3	Ensure that standard sequence spin coating produces expected thickness.	
4	E-beam Exposure			**All wafers**
4.1	E-beam exposure	E-beam writer: JEOL 9500	For AR-P 6200 (180 nm) at an acceleration voltage of 100 kV.	Dose depends strongly on a combination of parameters, test runs are needed.
5	Development and Rinse			**All wafers**
5.1	Development	Automatic TMAH developer	Develop with ZED N-50, 60s Rinse in IPA, 60 sec blow dry with N2	
6	III-V Pattern Transfer			**All wafers**
6.1	Selective InGaAs Wet Etch	Fumehood 07: III-V (dedicated)	(1:1:80) H_2SO_4(10%):H_2O_2(30%):H_2O	the rates should be tested before use, as they have not yet been calibrated at DTU Nanolab
6.2	Rinse	Fumehood 07: III-V (dedicated)	Rinse in DI water, 30 sec blow dry with N2	
6.3	SEM Inspection	SEM Supra 3	Evaluate Resist integrity	
7	Resist stripping and Lift-off			**All wafers**
7.1	Strip	Petribowl, Fumehood 08: III-V (dedicated)	Remover 1165 for 60 min + Rinse with IPA for 30 sec Rinse in water for 30-60 sec	An alternative stripping process involving Ultrasonic bath could be implemented.

7.2	Descumming	Plasma Asher 5	300 sccm, 400 Watt, 10 min	
7.3	SEM Inspection	SEM Supra 3	Inspect surface for traces of resist remains, and surface homogeneity.	
8	MOVPE growth of InP and InAs QD's			**All wafers**
8.1	Ammonium hydroxide clean	Fumehood 08: III-V	$NH_2OH(25\%):H_2O$, 5:1	Remove native oxides
8.2	MOVPE growth	MOVPE	Place a 2" wafer, wafer segment (quarter), or chip in the correct stage slot, load the sample into the reactor and perform the growth. InP growth of 20 nm, InAs qd growth.	******
9	Post Process Characterization			**All wafers**
9.1	SEM Inspection	SEM Supra 3	Perform SEM inspection using SEM Supra 3 to evaluate the dispersion of quantum dots on the wafer surface. Inspect the uniformity of quantum dot distribution, size variation, and any clustering or defects	..
9.2	AFM site control and Qdot Topology characterisation	AFM Icon Acceptance	Measure size, height, and shape of Qdots. Verify site-control	

7.4 Critical Thickness Script

This Python script implements calculations related to lattice properties in semiconductor materials, specifically using Vegard's Law and critical thickness estimation. The code consists of three main functions:

- **`vegards_law(X)`**: Applies Vegard's Law to estimate the lattice constant of an alloy as a function of the composition fraction X.
- **`lattice_mismatch(X)`**: Calculates the lattice mismatch between the estimated Vegard's Law lattice constant and a reference material.
- **`critical_thickness(h_c_guess, b, denominator, tol, max_iter)`**: Iterative function that computes the critical thickness of a strained layer using a convergence approach.

The script executes the critical thickness calculation by calling `critical_thickness()` with predefined parameters, yielding the final computed thickness value `h_c_final`. This implementation is crucial in material science and epitaxial layer design, helping to determine strain limitations and growth conditions for semiconductor heterostructures.

```
# Define a function to calculate Vegard's Law
def vegards_law(X):
    # Apply Vegard's law
    a = X * a_InAs + (1 - X) * a_GaAs
    return a

def lattice_mismatch(X):
    return (vegards_law(X) - a_InP)/a_InP

# tol: Tolerance level for convergence (default is 1e-3,
def critical_thickness(h_c_guess, b, denominator, tol=1e-3, max_iter
=100):
    for _ in range(max_iter):
        # Right-hand side (rhs) of the equation: This is the updated
value of h_c based on the current guess
        rhs = (b / denominator) * (np.log(h_c_guess / b) + 1)

        # Check if the difference between the current guess and the rhs
is smaller than the tolerance (convergence)
        if abs(h_c_guess - rhs) < tol:
            break

        # Update h_c
        h_c_guess = rhs
    return h_c_guess

# Perform the calculation
h_c_final = critical_thickness(h_c_guess, b, denominator)
```

8 Bibliography

References

[1] P Michler et al. “A quantum dot single-photon turnstile device”. In: *Science* 290.5500 (2000), pp. 2282–2285.

[2] P Senellart, GS Solomon, and AG White. “High-performance semiconductor quantum-dot single-photon sources”. In: *Nature nanotechnology* 12.11 (2017), pp. 1026–1039.

[3] R. Paschotta. “Optical Fiber Communications”. In: (Mar. 2024). DOI: 10.61835/9ec.

[4] U.N. Environment Programme World Conservation Monitoring Centre. *Submarine Cables and the Oceans: Connecting the World*. UNEP-WCMC Biodiversity Series 31. At page 3. UNEP-WCMC, 2009.

[5] International Telecommunication Union. *Spectral grids for WDM applications: DWDM frequency grid*. Accessed: 2024-12-03. 2020.

[6] Rajiv Ramaswami, Kumar N. Sivarajan, and Galen H. Sasaki. *Optical Networks: A Practical Perspective*. Third. San Francisco, CA: Morgan Kaufmann, 2010, pp. 70–76. ISBN: 978-0-12-374092-2.

[7] Bikash Kumar Das. “A Brief Review on Choice of Non-Linear Crystals for Spontaneous Parametric down Conversion”. In: *SSRN* (2021). DOI: 10.2139/ssrn.4118391.

[8] T. Miyazawa et al. “Single-photon emission at 1.5 um from an InAs/InP quantum dot with highly suppressed multi-photon emission probabilities”. In: *Applied Physics Letters* 109.13 (2016), p. 132106. DOI: https://doi.org/10.1063/1.4961888.

[9] Yury Berdnikov et al. “Near-critical Stranski-Krastanov growth of InAs/InP quantum dots”. In: *Scientific Reports* 14.1 (2024), p. 23697. DOI: 10.1038/s41598-024-70451-1.

[10] Pawel Holewa et al. “Bright Quantum Dot Single-Photon Emitters at Telecom Bands Heterogeneously Integrated on Si”. In: *ACS Photonics* 9 (2022), pp. 2273–2279.

[11] Dieter Bimberg. *Quantum Dot Heterostructures*. Wiley, 1999.

[12] I. Stranski and L. Krastanow. “Zur Theorie der orientierten Ausscheidung von Ionenkristallen aufeinander”. German. In: *Monatshefte fur Chemie* (). DOI: 10.1007/BF01571381.

[13] P Bhattacharya. “Strain-engineered quantum dots”. In: *Journal of Applied Physics* 117.11 (2015), p. 112807.

[14] P. Holewa, D. A. Vajner, E. Zieba-Ostoj, et al. “High-throughput quantum photonic devices emitting indistinguishable photons in the telecom C-band”. In: *Nature Communications* 15 (2024), p. 3358. DOI: 10.1038/s41467-024-47551-7.

[15] Jan Grosse et al. “Development of site-controlled quantum dot arrays acting as scalable sources of indistinguishable photons”. In: *APL Photonics* 5 (2020), p. 096107. DOI: 10.1063/5.0013718.

[16] Sudha Mokkapati, Hark Hoe Tan, and Chennupati Jagadish. “Selective-area epitaxy generates quantum-dot devices and integrates optoelectronics”. In: *SPIE Newsroom* (July 2006).

[17] Fugao Wang and D. P. Landau. “Determining the density of states for classical statistical models: A random walk algorithm to produce a flat histogram”. In: *Physical Review E* 64.5 (Oct. 2001). DOI: 10.1103/physreve.64.056101.

[18] Jr. William D. Callister and David G. Rethwisch. *Fundamentals of Materials Science and Engineering: An Integrated Approach*. 5th. John Wiley & Sons, 2018. ISBN: 978-1-119-17548-3.

[19] Felix Bloch. “Über die Quantenmechanik der Elektronen in Kristallgittern”. In: *Zeitschrift für Physik* 52.7 (1929), pp. 555–600. DOI: 10.1007/BF01339455.

[20] Mark Fox. *Optical Properties of Solids*. 2nd. Oxford, UK: Oxford University Press, Mar. 2010, p. 416. ISBN: 978-0-19-957337-0.

[21] Wolfgang Pauli. “Über den Zusammenhang des Abschlusses der Elektronengruppen im Atom mit der Komplexstruktur der Spektren”. German. In: *Zeitschrift für Physik* 31 (1925), pp. 765–783. DOI: 10.1007/BF02980631.

[22] Werner Heisenberg. “Über den anschaulichen Inhalt der quantentheoretischen Kinematik und Mechanik”. German. In: *Zeitschrift für Physik* 43 (1927), pp. 172–198. DOI: 10.1007/BF01397280.

[23] Louis de Broglie. “Recherches sur la théorie des quanta”. French. PhD thesis. University of Paris, 1924.

[24] E. Schrödinger. “Quantisierung als Eigenwertproblem”. German. In: *Annalen der Physik* 384.4 (1926), pp. 361–376. DOI: 10.1002/andp.19263840404.

[25] Prabhava Barimar. “A Study of Electronic Structure and Thermal Stability of Engineered SOI Material”. PhD thesis. Trinity College, 2018.

[26] N. N. Winogradoff. “Field Control of the Quantum Efficiency of Radiative Recombination in Semiconductors”. In: *Physical Review* 138.5A (1965), A1562–A1567. DOI: 10.1103/PhysRev.138.A1562.

[27] A. Bhattacharya E. T. Kuech and B. Bansal. “Self-Assembly in Semiconductor Epitaxy: From Growth Mechanisms to Device Applications”. In: *Handbook of Crystal Growth, Vol. 3, 2nd Edition*. Elsevier, 2015, pp. 1057–1099.

[28] Alexander Toifl. “Numerical Methods for Three-Dimensional Selective Epitaxy and Anisotropic Wet Etching Simulations”. Ph.D. Dissertation. Wien: Technische Universität Wien, July 2021.

[29] S. M. Sze and Kwok K. Ng. *Physics of Semiconductor Devices*. John Wiley & Sons, 2006. ISBN: 9780471143239. DOI: 10.1002/0470068329.

[30] Celso Israel Fornari et al. “Monte Carlo Simulation of Epitaxial Growth”. In: *Epitaxy*. 2018. Chap. 5. DOI: 10.5772/intechopen.70220.

[31] J.W. Matthews and A.E. Blakeslee. “Defects in epitaxial multilayers: I. Misfit dislocations”. In: *Journal of Crystal Growth* 27 (1974), pp. 118–125. DOI: 10.1016/S0022-0248(74)80055-2.

[32] Sergey Smirnov. “Physical Modeling of Electron Transport in Strained Silicon and Silicon-Germanium”. PhD Dissertation. Vienna, Austria: Technische Universität Wien, Dec. 2003.

[33] Michael Biehl, Florian Much, and Christian Vey. *Off-lattice Kinetic Monte Carlo simulations of strained heteroepitaxial growth*. 2005.

[34] Johnson Chuang, Daniel Weiskopf, and Torsten Möller. “Energy Aware Color Sets”. In: *Computer Graphics Forum* 28.2 (Apr. 2009). DOI: 10.1111/j.1467-8659.2009.01359.x.

[35] Joachim Piprek. “What Limits the Efficiency of High-Power InGaN/GaN Lasers?” In: *IEEE Journal of Quantum Electronics* PP.99 (Dec. 2016). DOI: https://doi.org/10.1109/JQE.2016.2644861.

[36] Charles Kittel. *Introduction to Solid State Physics*. 8th. Wiley, 2004.

[37] Peter Y. Yu and Manuel Cardona. *Fundamentals of Semiconductors: Physics and Materials Properties*. 4th. Springer, 2010.

[38] Otfried Madelung. *Semiconductors: Data Handbook*. 3rd revised ed. Springer, 2004. ISBN: 978-3-642-18826-7. DOI: 10.1007/978-3-642-18826-7.

[39] Neil W. Ashcroft and N. David Mermin. *Solid State Physics*. New York: Holt, Rinehart and Winston, 1976. Chap. 12.

[40] Bart J. Van Zeghbroeck. *Effective mass in semiconductors*. [Online; accessed 22-February-2025]. 1997. URL: apachepersonal.miun.se/~gorthu/halvledare/Effective%20mass%20in%20semiconductors.htm.

[41] Shun Lien Chuang. *Physics of Photonic Devices*. 2nd. Hoboken, NJ: John Wiley & Sons, Inc., 2009. Chap. 4.5.

[42] Veer Dhaka. “Ultrafast Capture and Relaxation of Carriers in InGaAs Semiconductor Quantum Well Nanostructures”. PhD thesis. Nov. 2006.

[43] Ioffe Institute. *Basic Parameters of InP - NSM Archive*. Accessed: 9 February 2025. 2025. URL: https://www.ioffe.ru/SVA/NSM/Semicond/InP/basic.html.

[44] Ioffe Institute. *Basic Parameters of InAs - NSM Archive*. Accessed: 9 February 2025. 2025. URL: https://www.ioffe.ru/SVA/NSM/Semicond/InAs/basic.html.

[45] Y. Arakawa and M. J. Holmes. “Progress in Quantum-Dot Lasers”. In: *IEEE Journal of Selected Topics in Quantum Electronics* 10.5 (2002), pp. 941–954.

[46] Cédric Priester. *Semiconductor Nanostructures: Growth and Energetics*. CRC Press, 2015. ISBN: 978-1-4822-3035-3. DOI: 10.1201/b18842.

[47] M. Schmidbauer et al. “Site-controlled growth of self-assembled InAs quantum dots on pre-patterned GaAs substrates”. In: *Journal of Applied Physics* 103 (2008). DOI: 10.1063/1.2919791.

[48] X. Ma et al. “Site-controlled growth of single and pairs of InAs quantum dots on patterned GaAs substrates”. In: *Applied Physics Letters* 119 (2021). DOI: 10.1063/5.0062221.

[49] Martin T. Dove. *Structure and Dynamics: An Atomic View of Materials*. Oxford Master Series in Condensed Matter Physics. Oxford University Press, 2002. Chap. 7.5.2. ISBN: 978-0-19-850678-9.

[50] David Zubia and Stephen D. Hersee. “Nanoheteroepitaxy: The Application of Nanostructuring and Substrate Compliance to the Heteroepitaxy of Mismatched Semiconductor Materials”. In: *Journal of Applied Physics* 85.9 (1999). DOI: 10.1063/1.370153.

[51] G. Springholz et al. “Strain-induced self-organization of quantum dots and rings”. In: *Science* 282.5395 (2008), pp. 734–737. DOI: 10.1126/science.282.5395.734. URL: https://doi.org/10.1126/science.282.5395.734.

[52] Christian J. Mayer, Mathieu F. Helfrich, and Daniel M. Schaadt. “Influence of hole shape/-size on the growth of site-selective quantum dots”. In: *Nanoscale Research Letters* 8.504 (2013). DOI: 10.1186/1556-276X-8-504.

[53] Mathieu Helfrich et al. “Growth and characterization of site-selective quantum dots”. In: *physica status solidi* 210.1 (2012), pp. 87–92. DOI: 10.1002/pssa.201228423.

[54] A. Mohan et al. “Polarization-entangled photon generation from a quantum dot embedded in a nanowire”. In: *Nature Photonics* 4 (2010), pp. 302–306. DOI: 10.1038/nphoton.2010.54. URL: https://doi.org/10.1038/nphoton.2010.54.

[55] J. Tersoff, C. Teichert, and M. G. Lagally. “Self-organization in growth of quantum dot superlattices”. In: *Physical Review Letters* 76.10 (1996), pp. 1675–1678. DOI: 10.1103/PhysRevLett.76.1675. URL: https://doi.org/10.1103/PhysRevLett.76.1675.

[56] N. N. Ledentsov et al. “Quantum dot heterostructures: fabrication, properties, lasers”. In: *Semiconductors* 32.4 (Apr. 1998). Review article. DOI: 10.1134/1.1187325.

[57] P. Holewa et al. “Droplet epitaxy symmetric InAs/InP quantum dots for quantum emission in the third telecom window: morphology, optical and electronic properties”. In: 2 (2021). DOI: https://doi.org/10.48550.

[58] P. Laferriere et al. “Unity-yield deterministic growth of telecom band quantum dots in photonic nanowires”. In: (2022).

[59] DTU Nanolab. *LabAdviser - DTU Nanolab Wiki*. Accessed: 28 February 2025. 2025. URL: https://labadviser.nanolab.dtu.dk.

[60] Allresist GmbH. *AR-P 6200 CSAR 62 E-Beam Resists - Product Information*. Technical product information for AR-P 6200 (CSAR 62) positive e-beam resists. Allresist GmbH. Feb. 2020.

[61] Ioffe Institute. *Basic Parameters of GaAs - NSM Archive*. Accessed: 9 February 2025. 2025. URL: https://www.ioffe.ru/SVA/NSM/Semicond/GaAs/basic.html.

[62] C. Ferrari et al. “Deviation from Vegard law in lattice matched InGaAs/InP epitaxial structures”. In: *Conference Proceedings. 2001 International Conference on Indium Phosphide and Related Materials. 13th IPRM (Cat. No.01CH37198)*. 2001, pp. 322–325. DOI: 10.1109/ICIPRM.2001.929123.

[63] Inc. DisChem. *SurPass 3000 Cationic Priming Agent Datasheet*. DisChem, Inc. Ridgway, PA, USA, 2025. URL: http://www.dischemінc.com.

[64] Toby Olver. *Wet Chemical Etching: Standard Operating Procedures*. Accessed: 16 Feb. 2025. 2025. URL: https://terpconnect.umd.edu/~browns/wetetch.html.

[65] UCSB Nanofab Wiki. *Wet Etching Recipes*. 2023. URL: https://wiki.nanofab.ucsb.edu/wiki/Wet_Etching_Recipes.

[66] Chun-Chieh Chang. “Step-Tapered Active-Region Mid-Infrared Quantum Cascade Lasers and Novel Fabrication Processes for Buried Heterostructures”. PhD thesis. June 2015.

[67] Marco Lamponi. “Hybrid III-V on silicon lasers for telecommunication applications”. French. NNT: 2012PA112039, tel-00769402. PhD thesis. Université Paris Sud - Paris XI, 2012.

[68] Charlotte Ovenden. “Development and Characterisation of Site-Controlled Quantum Dot Arrays”. PhD thesis. The University of Sheffield, Mar. 2021.

[69] Dow Electronic Materials. *MICROPOSIT™ Remover 1165 - Technical Data Sheet*. Technical data sheet for MICROPOSIT™ Remover 1165, detailing processing conditions and material compatibility. Dow Chemical Company. Feb. 2014.

[70] Yi Xuan, Hung-Chun Lin, and Peide D. Ye. “Simplified surface preparation for GaAs passivation using atomic layer-deposited high-kappa dielectrics”. In: *IEEE Transactions on Electron Devices* 54.8 (2007). DOI: 10.1109/TED.2007.900678.

[71] Harumitsu Hattori et al. “Compositions for cleaning III-V semiconductor materials”. WO2014089196A1. June 2014.

[72] Jiang Wang, Sam Mony, and Nercy Ebrahimi. “New Methods Eliminate Etch Defects in GaAs IC Production”. In: *Compound Semiconductor* 7.8 (Oct. 2001).

[73] Wilfried Erfurth, Andrew Thompson, and Nezih Unal. “Electron Dose Reduction through Improved Adhesion by Cationic Organic Material with HSQ Resist on an InGaAs Multilayer System on GaAs Substrate”. In: *Proceedings of SPIE*. Vol. 8682. SPIE. 2013, 86821Z. DOI: 10.1117/12.2018121.

[74] Suzie Poulin, John F. Currie, et al. “Etching of InP by H3PO4, H2O2 Solutions”. In: *Japanese Journal of Applied Physics* 29.10 (1990). DOI: 10.1143/JJAP.29.1912.

[75] Alan R. Clawson. “Guide to references on III-V semiconductor chemical etching”. In: *Materials Science and Engineering: R: Reports* 31.1 (2001). DOI: 10.1016/S0927-796X(00)00015-5.

[76] P. H. L. Notten. “Electrochemical study of the etching of III-V semiconductors”. PhD Thesis. Technische Universiteit Eindhoven, 1989. DOI: 10.6100/IR307988.

[77] S. Luo et al. “Impact of double-cap procedure on the characteristics of InAs/InGaAsP/InP quantum dots grown by MOCVD”. In: *Journal of Crystal Growth* 375 (2013), pp. 100–103. DOI: 10.1016/j.jcrysgro.2013.04.024.